UNIVERSITY OF CALIFORNIA
RIVERSIDE

Asymmetrical Flow Field Flow Fractionation Coupled to Nanoparticle Tracking Analysis for Rapid Enrichment and Online Characterization of Nanoparticles

A Dissertation submitted in partial satisfaction
of the requirements for the degree of

Doctor of Philosophy

in

Chemistry

by

Gary Brent Adkins

September 2021

Dissertation Committee:
Dr. Wenwan Zhong, Chairperson
Dr. Yinsheng Wang
Dr. Jason Cheng

The Dissertation of Gary Brent Adkins is approved:

_____

_____

_____

Committee Chairperson

University of California, Riverside

ACKNOWLEDGEMENT

I would first like to thank Dr. Wenwan Zhong for her patience and guidance. Her hard work and passion for chemistry kept me motivated throughout my years at UCR, but her patience and understanding were the most important part because she gave me the time and space I needed to recover when I became very ill in my second year. A major setback and a very difficult recovery placed continued challenges on my productivity, but Dr. Zhong was able to give me the time when I needed it, but also kept me focused on my goals.

I would also like to thank the staff and faculty at UCR, especially my committee members of Dr. Yinsheng Wang and Dr. Jason Cheng, who provided guidance and mentorship throughout my time at UCR. I also would like to thank Dr. Joseph Genereux for guidance and training and allowing the Zhong lab to share precious equipment. I would also like to thank the environmental toxicology department at UCR for the T32 funding opportunity I was able to apply for and receive involving the nanoparticle analysis and exosome secretion characterization work for toxicology assays.

I would also like to thank all the Zhong lab members, old and new, who have helped discuss, analyze, train, or repair the various protocols and equipment I have used over the 5 years. I especially would like to thank Ju-Yong Lee, Wen Shen, Kenneth Flack, Luis Jimenez, Jiwon Lee, Michael Trinh, and Kaizhu Guo for not only discussing science in lab, but also providing support and friendship as well as being there for the lab when the time

was needed. I would especially like to thank my undergraduate student Erica Sun, whose dedication to the project and hard work was unwavering during her time on the project.

I also would like to thank my family back east. Without them I would not be where I am today. Their love and encouragement kept me motivated while I sought a degree no one else in my family has reached. I am successful because they want me to be successful. I especially would like to mention my mom, who is by far the nicest person on the planet but also never wavered in her support and love.

And finally, I would like to thank my partner and love of my life, Christina Dioquino. I did not know her before I came to California, but I cannot imagine my future without her. She has brought stability and support into my chaotic life. I also cannot thank her enough for bringing our dog Chewie into my life. I brought my 1-year-old kitten, Princess Buttercup, to California 6 years ago, and while her passive looks of encouragement helped, it was my full family that made my time here survivable. Much of the writing of this dissertation was done with a warm dog at my side, a purring cat on my lap, and the love of my family at my back.

To everyone I mentioned above and the ones I forgot. Thank you!

The material in Chapter 2 and some of Chapter 3 were previously published, reprinted with permission from *Anal. Chem.* **2020**, *92*, 10, 7071–7078. The coauthor, Dr. Wenwan Zhong, directed and supervised the research that formatted the basis of this chapter.

ABSTRACT OF THE DISSERTATION

Asymmetrical Flow Field Flow Fractionation Coupled to Nanoparticle Tracking Analysis for Rapid Enrichment and Online Characterization of Nanoparticles
by

Gary Brent Adkins

Doctor of Philosophy, Graduate Program in Chemistry
University of California, Riverside, September 2021
Dr. Wenwan Zhong, Chairperson

AF4 is a size separation technique that is routinely used for nanoparticle analysis due to the open channel design, the gentle forces used, and separation being done in native and stable buffers. NTA is an excellent detector for AF4 due to the flow cell fluidics and the individual counting and sizing NTA performs, making it an excellent candidate to use as an online detector to allow simultaneous fractionation and characterization of samples. NTA is label free, making general detection of all NPs above a certain size possible, making this a very versatile detector that can be used for many types of nanoparticles and materials that may be separated by AF4.

Chapter 2 focuses on the coupling connection and validation of the AF4-NTA system. The initial design required a split flow design. COMSOL simulations were done to determine the best strategy for splitting the eluent into multiple lines of equivalent sample. A splitter manifold was used to control pressure and flow while a syringe pump was used to control the flow rate going through the NTA. The AF4-NTA system showed great particle counting ability and consistent sizing of the different size populations of

standards tested. Some drawbacks were identified with the split flow design, which was mainly band broadening from the larger dead volume of the NTA channel. The main counting ability showed very strong linearity when evaluating sequential increases in injection amounts and produces simple and attractive three-dimensional fractograms.

Chapter 3 uses AF4-NTA for the analysis of non-spherical particles and soft-shelled and flexible materials like exosomes. AF4-NTA was used to separate and analyze two different aspect ratios of gold nanorods. The NTA hydrodynamic size and TEM data were used to determine the conversion factor between the NTA hydrodynamic size and the rod length. Additionally, it was shown that offline NTA had difficulty identifying the two populations but were easily identified when utilizing AF4 separations before NTA analysis. AF4-NTA was also used to analyze 2D nanomaterials and the protein corona formation around it once it was incubated in cell culture medium. AF4-NTA showed very rapid analysis of nanomaterials, allowing quick determination of aggregation and protein corona thickness. Finally, the system was tested against softer and more flexible materials, which AF4 has advantages over SEC. Good recovery, quantification, and sizing indicate the AF4-NTA is quite versatile and applicable to a wide array of sample types, matrices, sizes, shapes, and composition.

Chapter 4 focuses on the development of AF4-NTA for exosome analysis. AF4-NTA showed applicability in measuring extracellular vesicles, but additional downstream analysis is needed to make use of the BioNP information. AF4 was used as a preparatory step for the downstream analysis while the offline NTA data characterizes the BioNPs collected. The AF4 recovery was compared to other common isolation techniques as well

as the purity and native size investigated and showed comparable purification abilities. In-channel labeling was performed as an efficient way to wash exosomes of unbound probes, allowing simple plating and quantification of the probes. This technique removes every step of blocking, incubating, and washing because AF4 can complete this on the analyte directly during the size separation. While AF4-NTA was never ran with the final probe designs due to the COVID-19 shutdowns, it was shown that in-channel labeling and protein label quantification within the ranges of NTA is possible.

AF4-NTA is versatile with broad applicability. The online NTA data saves time, sample, and allows direct relation of particle counts to downstream results. The throughput is very quick compared to individual steps of purification, characterization, and protein quantification. Some drawbacks still exist, such as band broadening from slow flow rates in NTA, AF4 dilution factor, and limited working ranges by NTA. Some of these can be further improved while some are inherent drawbacks of the individual instruments used, but AF4-NTA was shown to be an ideal candidate for general nanoparticle analysis, especially when dealing with complex matrices or mixtures of multiple size populations.

TABLE OF CONTENTS

LIST OF FIGURES

LIST OF TABLES

Chapter 1: Introduction and Background

1.1 - Introduction

This chapter will discuss the relevant background necessary to understand the motivation, challenges, and novelty of the work involving asymmetrical flow field flow fractionation and nanoparticle tracking analysis for general nanoparticle analysis. Nanoparticle's wide adoption in commercial products and the pharmaceutical industry has increased demands for robust, simple, and efficient nanoparticle analysis. The growth is expected to continue as more nanomedicines, smaller electronics, and nanoparticle-based assays continue to hit the market. The buildup of engineered nanoparticles and the breakdown of plastics into micro- and nanoplastics are of growing concern that requires extensive studies evaluating the impact nanoparticles may induce on the environment. Often, the enrichment, purification, or analysis preparation steps cause aggregation, fusion, destruction, or physical changes in the material. The work outlined in this dissertation intends to develop a single system that can accurately and rapidly enrich, size, count, and fractionate native nanoparticles separated by asymmetrical flow field flow fractionation.

1.2 - Nanoparticle Overview

Nanoparticle is often a buzzword science fiction movies and CSI marathons use to add scientific jargon to create technical mystery. NPs may even be the destructive technology that ends all of mankind, but NPs are much less sinister. NPs are a type of material classified as particles with a single dimension less than 100 nm in size; however nanoparticles are often considered to be particles with dimensions less than 1 μm.[1] As the size of a particle gets smaller, the relative surface area to volume ratio increases. Increasing

surface area increases the efficiency of the desired surface reactions by increasing the number of exposed reaction sites.[2–6] Figure 1.1 shows how relative surface area increases as the size of the material decreases. Increased interaction with the solvent increases the overall efficiency of any nanoparticle-based reaction than reactions performed with the same mass of micron-sized material. This increased efficiency has led to widespread use of nanoparticles in bioanalytical assays and purification as well as numerous applications in electronics, sensors, and pharmaceuticals where various sizes, shapes, compositions, and surface modifications create a unique material designed for specialized applications.

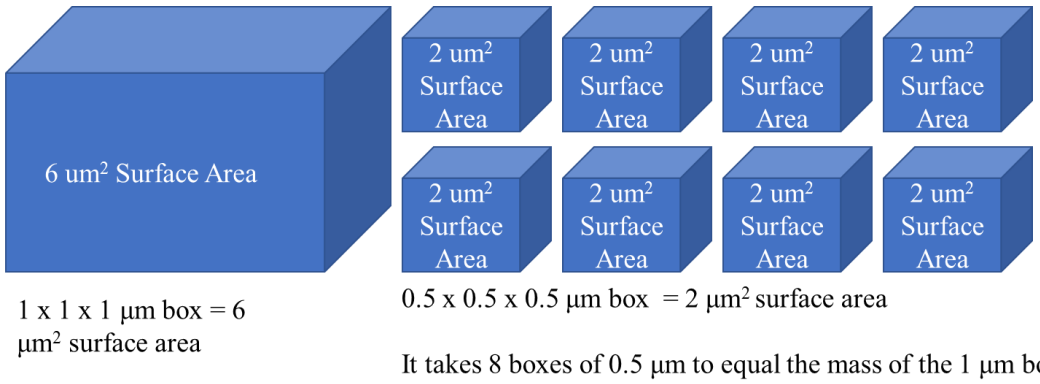

Figure 1.1 Relative surface area to volume ratio increases as NP size decreases. With equal masses, the number of reactive sites is ~2.6 times higher with the smaller 0.5 µm box than the 1 µm box.

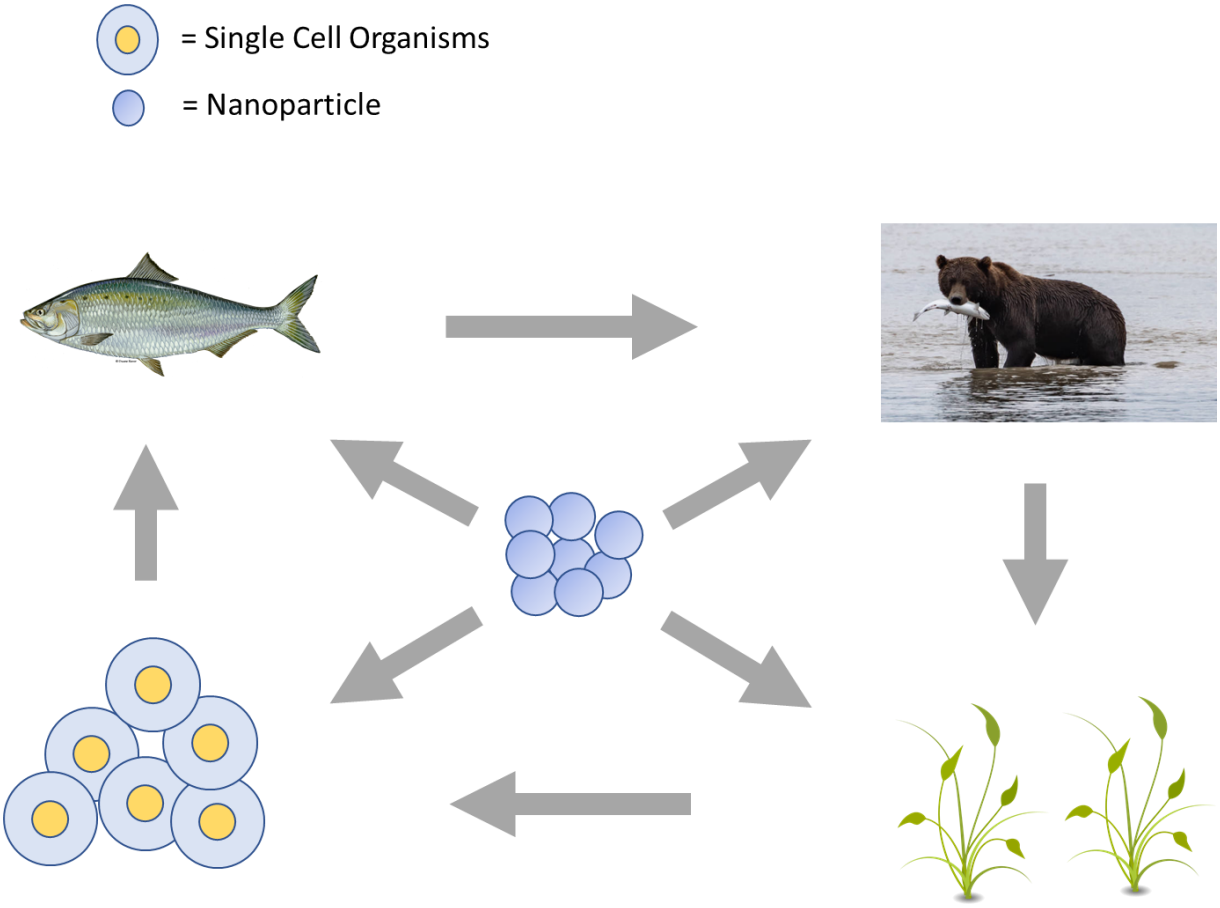

Figure 1.2 - Nanoparticle persistence in the environment as it is exchanged from host to host until total degradation.

The smaller sizes also create unique problems compared to larger and heavier particles, especially dealing with invasiveness in the environment.[7,8] Larger, micron-scaled particles are affected by gravity and tend to settle in aqueous environments, but smaller NPs can be affected by the random motion of the water in an aqueous environment. In an aqueous ecosystem, these smaller particles have better solubility and a higher mobility leading to increased environmental persistence.[9] The higher solubility increases particle concentration in water, which can then be taken in by smaller organisms through various uptake mechanisms such as ingestion, and endocytosis. Figure 1.2 shows a

schematic showing the lifecycle of a NP. Cellular uptake is dependent on size as well as shape and surface functional groups.[10–16] NPs can persist in the body due to the biocorona, which is a biological shell that may provide protection from degradation pathways and may appear as an analogous biological NP to the host organism.[17–19] The shell is created from proteins, fatty acids, oligonucleotides, and metabolites adsorbing to the surface of the NP and forming a biological shell.[20–23] This shell is dynamic, with the early stage of the corona being formed with highly mobile and abundant molecules with low affinity. As molecules of higher affinity interact with the ENP, the low affinity molecules become displaced, eventually leaving only high affinity proteins bound once the final corona is formed. The shell adds stability, neutralizes charges, and shields reactive groups from interfacing with the solvent. Increased stability allows longer retention in the host, which could be consumed by a larger organism. This cycling of NPs persist until the NP has been degraded completely or removed from the environment through waste and water treatment.[8] Degradation in a biological host is not always a safe route for the cell because lysosomal degradation can produce toxic byproducts.[24,25] After cellular uptake by endocytosis, the NP faces two pathways: internal release into the cytosol, or degradation by lysosomes.[26–29] Upon lysosomal degradation, the NP can induce a change or cause cytotoxic effects as the corona protecting the NP is destroyed and the core NP is exposed. This can lead to high amounts of ROS generation, alteration of the pH, or lysosome-mediated cell death.[30–35] This toxicity is not just a concern for engineered particles, but also for bulk plastics that have high resistance towards environmental degradation. The breakdown is much slower, but still releases small fragments of micro- and nanoplastics that begin to interact with the

environment in the same manner.[36–42] Nanoparticles, regardless if initially designed as nano-sized or created through the degradation of bulk materials, requires analysis of the core material, the corona information, and how those may affect uptake and fate, and the nanotoxicity during transport and degradation pathways.

1.3 - Engineered Nanoparticles

Engineered NPs (ENPs) are materials specifically designed and manufactured to be nanosized with specific interactions or properties that are needed for a specific application.[43–49] A common example is graphene sheets for electronic applications and sensors.[50–54] The single sheet has great conductive properties and it can be used as conductive patterning on chips. Commercial products are designed for long-term storage and product functionality, but also may make it resistant to common degradation pathways like oxidation. Not only is the design and specific toxic effects a concern, so is the production waste and byproducts that may be hazardous or contain a wide distribution of morphologies and toxicities.

There are different synthetic routes to functional nanomaterials. Figure 1.3 shows a few common techniques used to make platinum nanoparticles.[55] Different routes produce different yields and size distributions. Synthesis of these specialized materials commonly require a nucleation or crystallization buffer to initiate NP agglomeration, which are then grown into the desired size as the NPs crystallize. These polymerization reactions can create NPs with different sizes and shapes as the reactions continue and the NPs grow. Wide size distributions are common and need size fractionation to isolate particles of a narrower distribution for use.[56–58] Furthermore, solution stability is increased with

stabilizing additives that are added to the NP buffer or chemically modified surface passivation increase longevity and dispersion properties.[59–63] Some additives may need to be included in a stabilization buffer or may be chemically linked to the surface to provide constant stability to the NP, even after removal of the storage buffer. Zeta potential also plays an important role in stability and reactivity. DLVO theory describes the colloidal state as the overall product of the dispersion and electrostatic forces.[64,65] It is common to

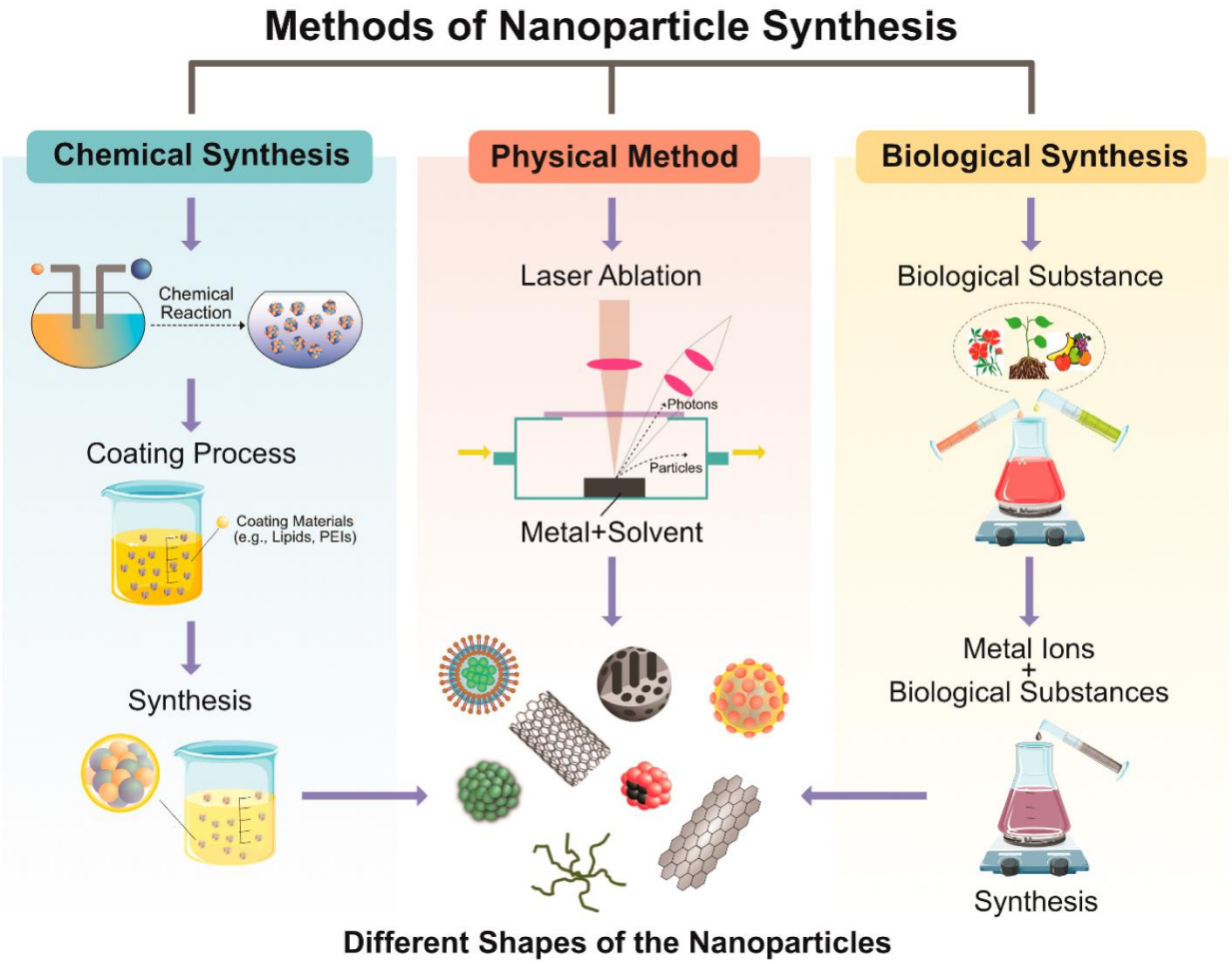

Figure 1.3 - A diagram showing common synthesis routes of metal nanoparticles. Reprinted from Reference 55

manipulate the surface to increase the repulsive force between NPs to add stability. However, once the material is removed from the colloidal state, they are prone to aggregation and are highly reactive to molecules of opposite charge. Many of the techniques used to functionalize or stabilize NPs may also have negative environmental impacts or increased cytotoxicity.

1.4 - Biological Nanoparticles

NPs are not always synthetic and may be biologically produced, with unique functions and considerations. Biological NPs (BioNPs) range in types, functions, and composition with many different therapeutic or analytical interests.[66–68] Most of these can be classified into a few classes: protein aggregates/complexes, lipoproteins, exosomes, microvesicles, and apoptotic bodies.[69] Figure 1.4 shows a diagram showing the different classes and generalized size range of BioNPs.[70] These different classes are generated through differing mechanisms, but also have different analytical significance due to their biogenesis mechanism. Below is a quick description of the different classes of BioNPs commonly found in biofluids and the considerations of isolating and analyzing the BioNP.

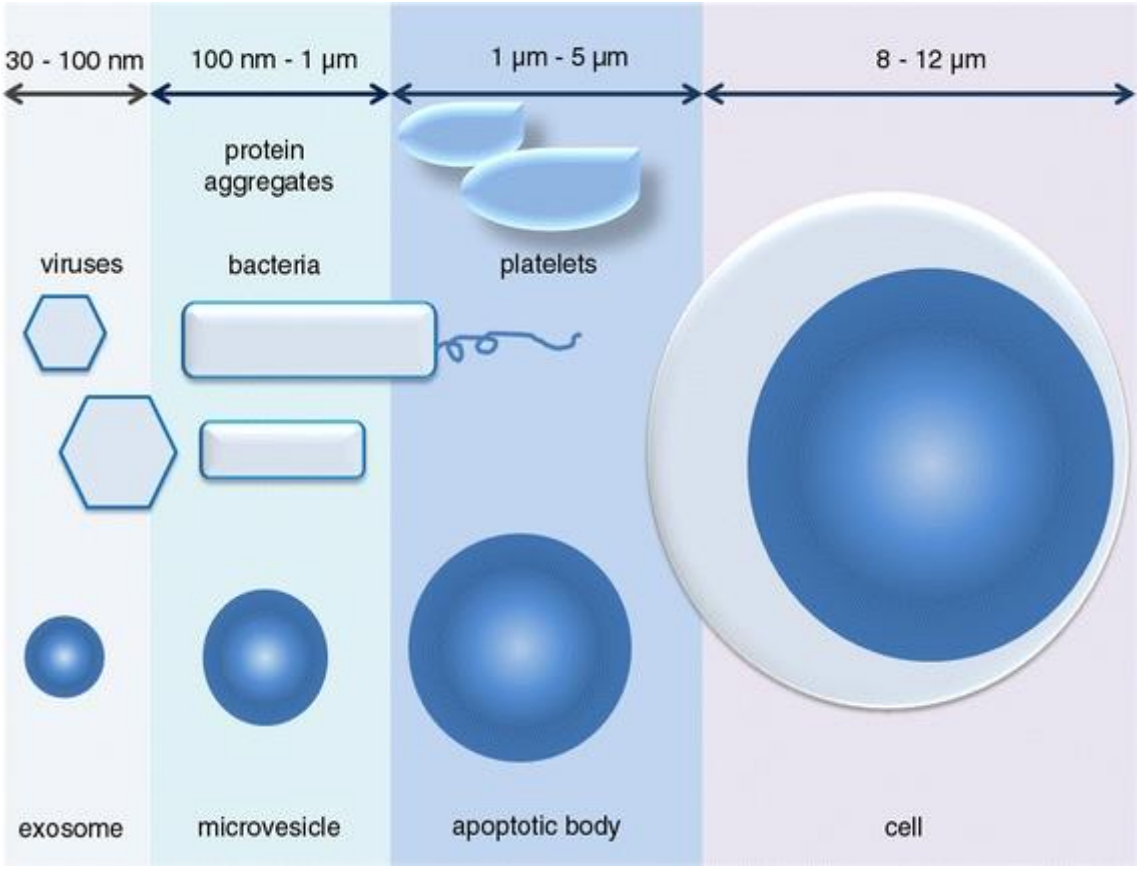

Figure 1.4 - Different classes of BioNPs and the general size ranges. The size cutoffs are generalized and there are overlaps between these groups in sizes. Lipoproteins are not shown but overlap with exosomes and microvesicles. Figure reprinted from reference 70.

1.4.1 - Protein Complexes/Aggregates

Protein complexes are usually constructive protein association[71] while aggregation is considered an undesirable product,[72,73] but both exist is biofluids and both can be of analytical interest. The core and surface are comprised mostly of proteins and peptides. The size range of protein aggregates can cover the whole range shown in Figure 1.4. Ophthalmology injections have strict FDA regulations for particulates above 2.5 µm and small HMW species are evaluated by SEC for stability studies in biological drug products.[74–78]

1.4.2 - Lipoproteins

Lipoproteins are particles that are composed of a hydrophobic core surrounded by a monolayer of lipids and encasing apolipoprotein.[79–82] Each subclass of lipoprotein has a different apolipoprotein marker unique to the BioNP. The monolayer is composed mostly of cholesterol and triglycerides, however many different lipids can be associated in the complex.[69,79,83,84] The size range of these particles can be from approximately ~5 nm to 100 nm.[69,79,85] The bulk of these vesicles are in the smaller range of 50 nm or less for very low-density lipoprotein (VLDL), low-density lipoproteins (LDL), and high-density lipoproteins (HDL). Lipoproteins are commonly measured to evaluate cholesterol levels; however, this is mainly from protein levels only and not from a perspective of nanoparticle quantification. The ratio of the different sub classes of lipoproteins indicates risk of heart disease and eventual blockages of arteries as the abundance of larger lipoprotein classes increases.[69,80,84]

1.4.3 - Exosomes

Overlapping in size with lipoproteins and aggregates are exosomes. Exosomes are usually bigger than lipoproteins and are usually in the size range of ~50-200 nm, even though some research suggests there are smaller exosomes in the ~20-50 nm range.[86–89] Exosomes are a lipid bilayer particle that is generated from a parent cell.[68,88–96] All mammalian cells secrete exosomes in some form, and it is thought this is a primary mechanism of cellular communication through exchange of vesicle cargo and surface receptors.[97–103] Exosomes are generated from a specific mechanism of budding during endocytosis (Figure 1.5), but the mechanism is still poorly understood. During

endocytosis, a multivesicular body (MVB) forms from the outer cell wall (Figure 1.5 (A) and (Figure 1.5 (B)) which caves inward, surrounding the molecules accumulated in the extracellular space. The MVB starts budding exosomes from the inner membrane (Figure 1.5 (C)), shedding them into the inner space of the MVB (Figure 1.5 (D)) that contains the encapsulated extracellular fluid. These buddings carry cell surface membrane proteins, cytosolic proteins and metabolites, and nucleic acids like miRNA and mRNA. The MVB begins to fill up with generated exosomes, plus the exosomes and cargo taken in during endocytosis. The MVB has two possible pathways: degradation (Figure 1.5 (E)) or secretion (Figure 1.5 (F)). In the degradation pathway, the MVB is chaperoned to lysosomes where the hydrolytic degradation of the vesicle and MVB releases the cargo contents of the outside exosome into the receiving cell. With secretion, the MVB fuses with the outer membrane and causes the exosomes to be released into extracellular space around the cell, which can then be taken in by neighboring cells (Figure 1.5 (G)). Each exosome is composed of a membrane bilayer from the parent cell enveloped around a small volume of the cell cytosol. Figure 1.6 shows a diagram of an exosome containing some of the parent contents after secretion. The exosome protects the cargo contents from degradation (especially RNA) as it is cycled through the body.[104–106] Exosomes also contain surface markers specific to exosomes, such as CD63, CD9 and CD81.[68,88,103,105,107–111] Additionally, many cancers show increased secretion rates of exosomes and microvesicles that alter the tumor microenvironment.[92,92,97,99,101,112–115] Not only does the cargo content tell information about the cell, so does the size and number of exosomes being secreted.

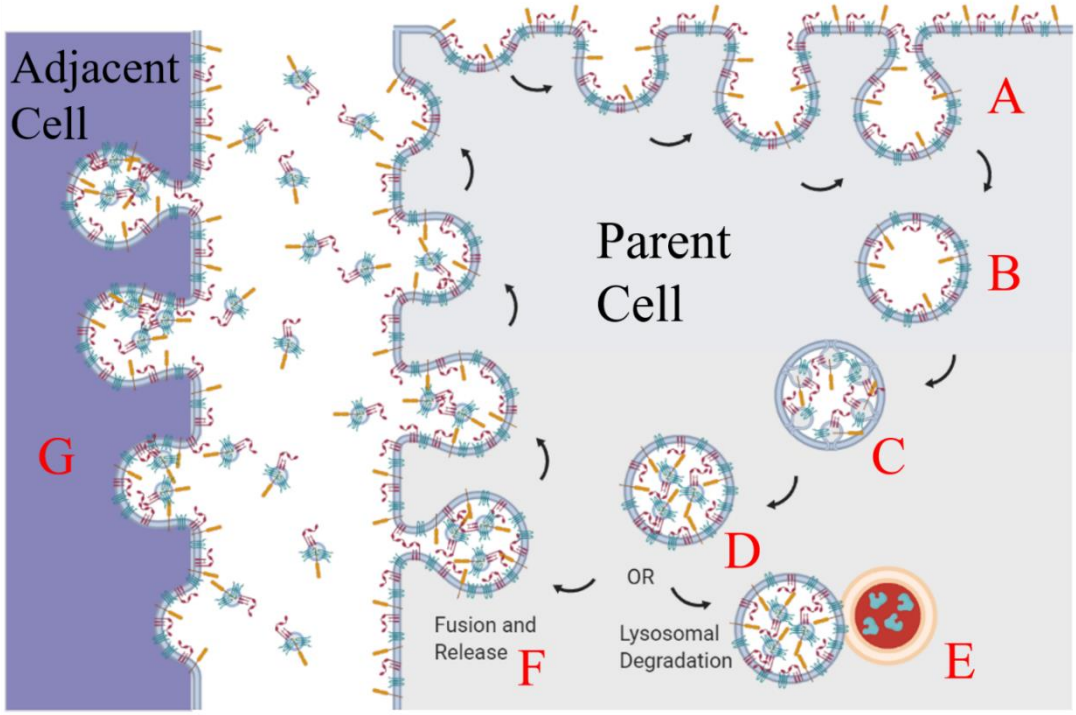

Figure 1.5 – A diagram showing endo and exocytosis as well as the generation of exosomes in the MVB. Endocytosis begins by an inward budding of the outer membrane (A). The MVB breaks off completely from the membrane and is internalized by the cell (B). Inward budding of the MVB starts the exosome formation with the inner space containing the cytosol from the interior of the cell (C). MVB containing freshly generated exosomes as well as the neighboring exosomes taken in during endocytosis (D) is sorted for lysosomal degradation (E) or fusion and release with the outer membrane wall (F). Released exosomes are then taken in by neighboring cells (G) or taken back in by the parent cell. Created with BioRender.com.

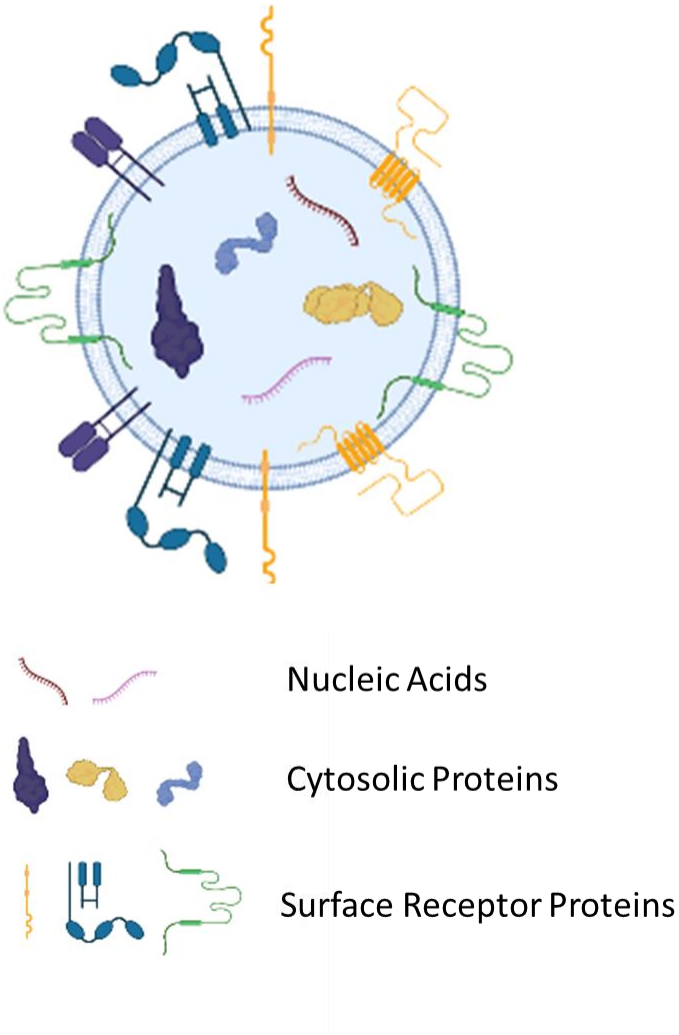

Figure 1.6 - Example diagram of an exosome and the biochemical targets for analysis. Created with Biorender.com

1.4.4 - Microvesicles

Microvesicles are lipid bilayer particles that are approximately ~50 nm to 1 μm in diameter and has some overlap with exosome size and NP properties.[66,89,113,116–118] These vesicles are budded off the cellular membrane surface directly into the extracellular region, but still are lipid bilayers from the parent host that envelope the cell's cytosol. Different

biogenesis routes do create particles with slightly different composition as CD63, CD9 and CD81 that are not expressed on microvesicles, but they do carry disease signature and alter the tumor microenvironment in a similar fashion as exosomes.[104,115,119–121] Regardless of the differences, microvesicles and exosomes both contain information from the parent cell that can be analyzed for disease markers.

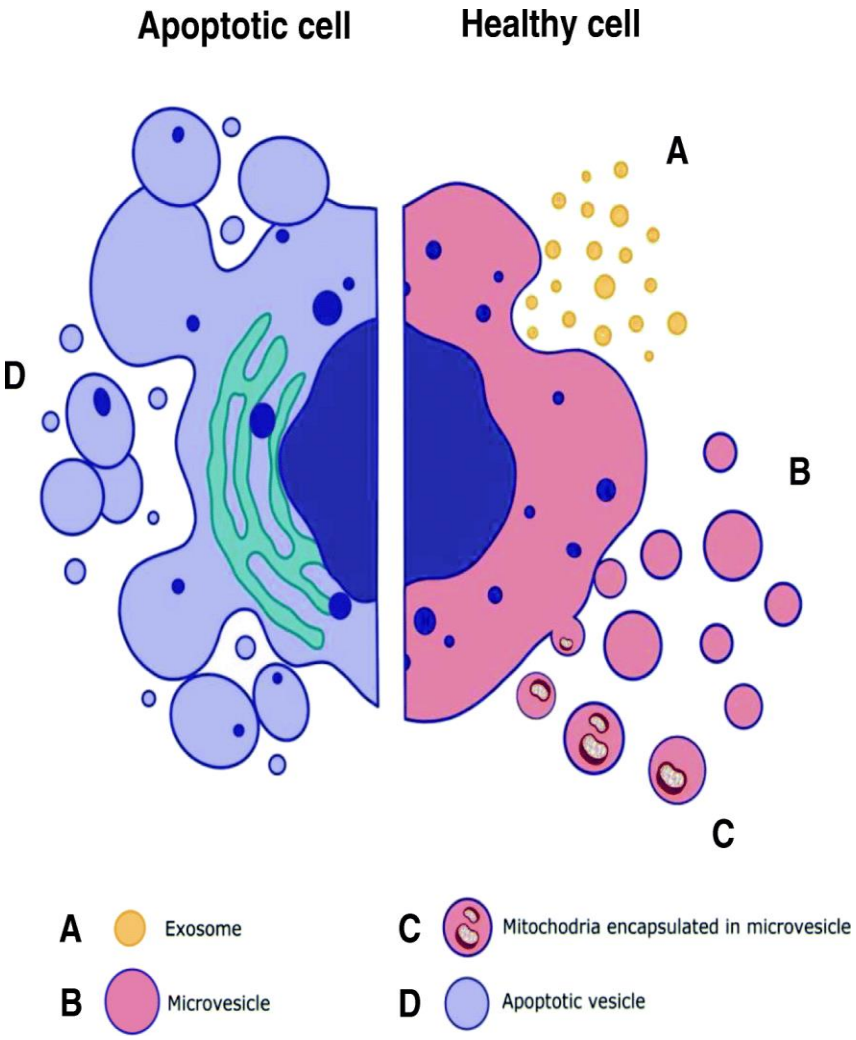

Figure 1.7 – A diagram showing and a cell undergoing apoptosis and a cell normally releasing BioNPs. There will be overlap in sizes with the different types of particles. Reprinted from reference 122.

1.4.5 - Apoptotic Bodies

Apoptotic bodies are generated when the cytoskeleton breaks down during normal programmed cell death. These share a similar lipid bilayer structure as microvesicles and exosomes and have a very wide size range and would overlap with most particles; however, the cargo content could be quite different from the metabolic changes and activated cascade pathways a cell undergoes during apoptosis. Figure 1.7 shows the differences in biogenesis mechanisms between exosomes and apoptotic bodies.[122] Some overlap in size can make these BioNPs appear as exosomes, but they carry different chemical signatures and would not carry CD63, CD9, CD81, etc.

1.5 - Nanoparticle Characterization Techniques

All NPs have some base material, whether it is a polymer, an amino acid, a lipid, or a metal ion that can be measured to confirm the composition of the NP. Individual layers may need to be measured, such as biocorona or passivation layer thickness. Metal nanoparticles can be dissolved and analyzed by ICP-MS for analysis of the metal ion ratios for the different layer thicknesses needed, while proteolytic digestion of the proteins in the biocorona can identify biocorona components after the quantum dot had encountered a biofluid.[123–129]

BioNPs have biochemical signatures that can be targeted to isolate selective subpopulations or to analyze the composition and components of a BioNP for disease signature. Biochemical assays on surface receptors, lipid content, miRNA, or mRNA can quantify various cargo components to observe disease biomarkers in relation to housekeeping or normalizing markers. Exosomes from HER2 positive breast cancer have

been shown to not only overexpress HER2, the HER2+ exosomes can alter treatment efficacy due to the competitive binding with cell surface receptors.[106,130–134] POC assays have been developed for HER2 expression levels showing relative signal intensity of HER2 on exosomes collected from serum by anti-CD63 magnetic beads.[133] All biofluids show the presence of exosomes to some degree, but urine has shown promise due to the filtering of the biofluid the kidney does enriches the fluid to only have exosomes from the renal organs. Overexpressed biomarkers such as engrailed-2 or annexin A3 can be specifically quantified as biomarkers of prostate cancer.[135] Coupling traditional biochemical assays to NP characterization techniques provides very rich information about the BioNP and the originating cell. The size, shape, number, as well as the identification of surface proteins and cargo contents can be analyzed to determine certain disease, especially cancers where the BioNP has unique signatures compared to healthy cells.

1.5.1 - Microscopy

The most straightforward way to determine morphology is to use microscopy techniques to image the NPs. The resolution of traditional light microscope is diffraction limited based on the wavelength of light used.[136–138] The equation governing this is:

$$R = \lambda / 2n \sin\theta \quad (1)$$

where R is the resolution, λ is the wavelength of the incident light, n is the refractive index of the imaging medium, and θ is the aperture angle. This simply states that the resolution of the image is limited by the size of the incident wavelength and the medium the image is taken in. When the θ is maximized at 90° and the medium is air, the maximum resolution

that can be achieved is the wavelength of incident light. The *R* with D_2 light would be 190-380 nm and would not be sufficient to give any detail about the morphology of a NP.

A very expensive but powerful microscope is an electron microscope (EM). Electron microscopy increases *R* from the duality of an electron.[139,140] The De Broglie wavelength of an electron is about 1000 times smaller than a photon, which can reduce the 200 nm resolution of a light microscope to 200 pm. Transmission and scanning electron microscopy (TEM and SEM) are both employed to image NPs using electron beams instead of photon beams. TEM works on the transmission of electrons through the particle while SEM works by imaging the electrons backscattered from the NP surface and gives better information about the surface structure and shape of a NP. It can perform additional analysis like energy-dispersive X-ray spectroscopy (EDS). EDS can identify atomic signatures by the energy difference of the displaced electrons. EDS is limited to the surface coating but can be very helpful in identifying the surface reactive groups and the surface composition of a NP.[141,142] Figure 1.8 shows different silver NP structures under SEM and TEM magnification. SEM provides detailed surface images and can resolve surface defects and imperfections due to the detection angle of the instrument while TEM is a 2D image created from the different intensities transmitted through the material.

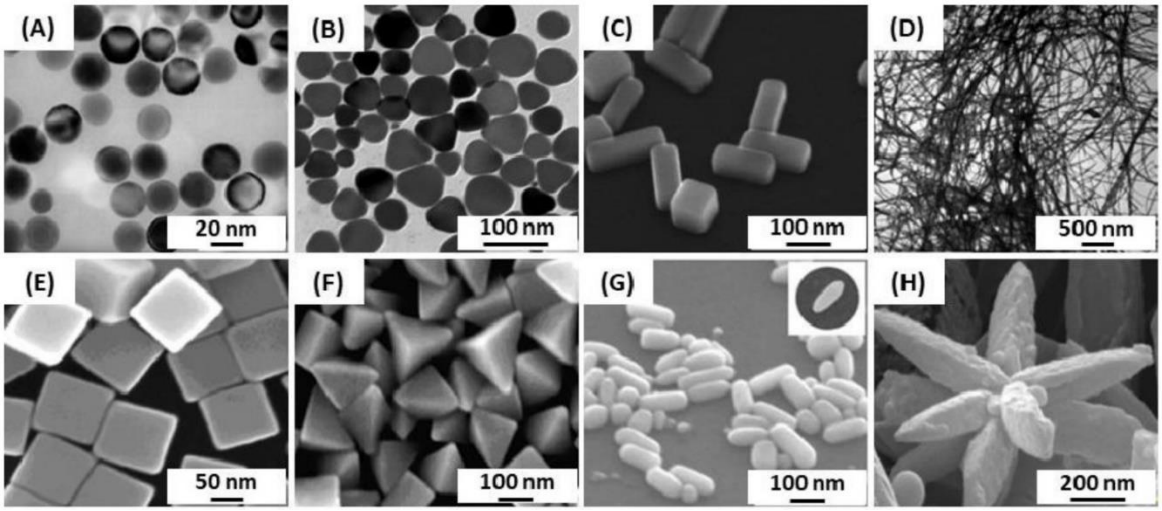

Figure 1.8 - Different EM images of various shapes and sizes of silver NPs. A, B, and D are TEM images evident from the brightfield image. C and E-H are SEM images, and a much better image of the NP surface can be seen. Even very fine imperfections as seen on the arms of the starred shape can be identified. Reprinted from Reference 143.

*1.5.2 - **Dynamic Light Scattering***

DLS is an optical technique that determines the diffusion coefficient of the bulk solution by measuring the fluctuation intensity of monochromatic light being scattered by macromolecules in solution to determine *D*.[144–148] The light undergoes a phenomenon called Doppler broadening which causes intensity fluctuations that change at a specific rate dictated by the Brownian motion of the particle.[149] Using the Stokes Einstein equation, the *D* can be related to a spherical hydrodynamic diameter by:[150,151]

$$D = \frac{K_B T}{6\pi\mu R_h} \qquad (2)$$

Where K_B is the Boltzmann's constant, T is temperature, μ is solvent viscosity, and R_h is the hydrodynamic radius. The rate of fluctuation is related to the speed of the particle in solution, which relates to its size by Equation (2). The drawback to DLS over NTA is it

involves bulk analysis. Coeluted analytes or multiple populations measured simultaneously will bias the data.

1.5.3 - Nanoparticle Tracking Analysis

Nanoparticle Tracking Analysis (NTA) is a simple, yet powerful, optical detector that utilizes a high-power objective to visualize particles in the channel.[148,152–157] Figure 1.9 shows a schematic of the optics arrangement for NTA. A fluidic channel on top of a laser module with the beam aimed at the critical angle causes NPs to scatter light towards a 60× objective positioned above the channel.[158] The system takes a video of the channel and tracks the scatter point, measuring the mean squared displacement (MSD) of the particle over a series of frames. The system determines a diffusion coefficient from the MSD with a simple equation:

$$MSD = 2D * d * t \quad (3)$$

Where D is the self-diffusion coefficient (commonly known as diffusion coefficient), d is the number of dimensions observed and t is the timescale the displacement is measured over.[159] The software takes multiple D measurements over multiple time scales and averages D for each tracked particle. The system then converts the hydrodynamic diameter from D using Equation (2). The system's power comes from the individual sizing and counting that generates a true number distribution.

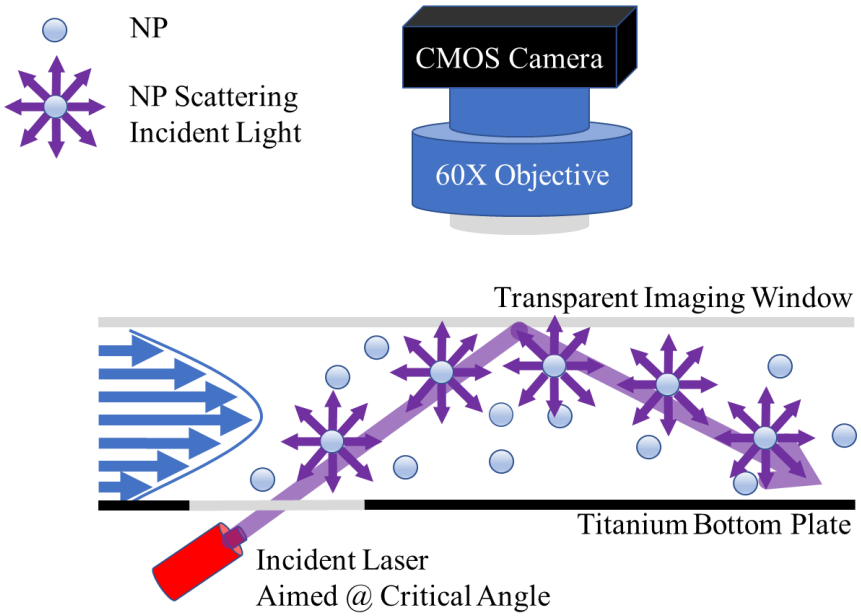

Figure 1.9 - Diagram of the NTA flow cell and camera setup. The critical angle allows NPs to show up as bright scatter points against a negative background, allowing them to be recorded so D can be determined.

One of the main drawbacks in NTA is the limited working range for concentration. The Stokes-Einstein is only accurate at near infinite dilution in an incompressible Newtonian fluid.[144] This results in a working range of about 10^7 to 10^9 particles/mL for NTA. It is estimated that the viewing window for NTA is only approximately 20 nL, which is the bounds of the visible laser beam in the channel.[160] The small volume decreases sensitivity when converting the particles/frame to particles/mL because a single particle represents ~10^6 particles in solution. To increase distribution repeatability, it is common to measure NTA under a slow flow rate to cycle more particles into the viewing window during analysis.

1.6 - Nanoparticle Isolation Techniques

NP analysis usually needs enrichment or purification from matrix components before analysis. NPs and BioNPs can be isolated using filtration, size separation, immunoprecipitation, or centrifuge precipitation. Each method has pros and cons and is selected based on the downstream process or analysis being performed. AF4 was used in this dissertation as an enrichment technique for NPs from complex matrices and below is the background information of the orthogonal techniques that could be used in place of AF4 and the drawbacks of each.

1.6.1 - Precipitation

Precipitation is a common way of isolating NPs with centrifugation.[161–168] Metallic core NPs tend to have high densities and can easily be spun down in a benchtop centrifuge, but less dense and smaller particles require ultracentrifuge speeds to pellet the sample. BioNPs generally have lower density, but large particles can spin down much easier than smaller particles and this can be exploited to separate populations with large differences in diameter.[67,165,169,170] Figure 1.10 shows a standard differential UC protocol with increasing speeds to collect debris, microvesicles, and then exosomes sequentially.[171] Density gradient UC is able to isolate particles based on density instead of size and can be a valuable tool for BioNP and NP separation.[166,172–174] UC is the most common protocol for BioNPs but some studies suggest high amounts of vesicle fusion, coprecipitation, and poor yield make BioNP analysis difficult.[66,175–177] Vesicle fusion can lead to false assumptions about BioNP surface area, number of secreted exosomes, or the native aggregation state.

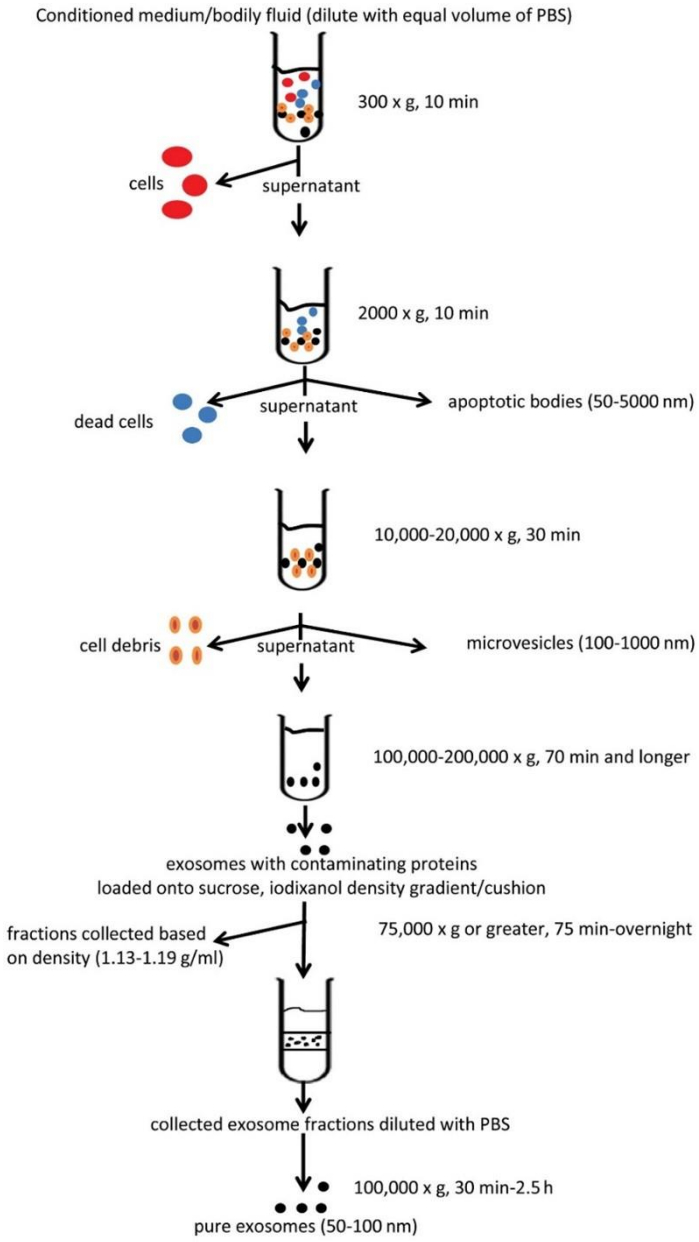

Figure 1.10 - Differential ultracentrifugation involves multiple steps of increasing speeds to isolate different populations of BioNPs. A density ultracentrifugation was performed to isolate exosomes from lipoproteins. In all, 6 pelleting steps taking a minimum o of 4-5 hours is needed to collect enriched exosomes. Reprinted from Reference 171.

1.6.2 - Precipitation Reagents

Exosomes and small microvesicles require ultracentrifuge to pellet, but some commercial products have been developed to precipitate vesicles using benchtop speeds.[175–179] A similar process of preclearing the biological matrix is needed similar to UC, but once the debris and apoptotic bodies are cleared, an additive that either reversibly dehydrates or crosslinks the exosomes into denser or larger structures that can easily be spun down at speeds of 20k ×g or less. These methods have very high yield, especially dehydration because osmolytes dehydrate bilayer specifically without altering the density of proteins or lipoproteins. All precipitation processes (UC, benchtop, chemical) coprecipitates proteins with the charged vesicles from electrostatic drag as the vesicles pellet, so it is common to do a second precipitation to reduce the background impurities.[180–183] Both work by pelleting the sample, and then resuspending the pellet in fresh buffer, which dilutes the reagent below functional concentrations. Some reagents can be retained and can affect downstream analysis, but the specificity and high yields make this a very good method to compare recovery of exosomes and microvesicles.

1.6.3 - Filtration

Filtration can be done with a variety of filters and membranes, setup in various fluidic configurations.[184–189] Filters have a molecular weight cut off (MWCO) that will retain molecules sufficiently larger than the cut off, usually around 5 to 7 times the MWCO. Different MWCO filtration steps can be used to enrich a sample for a certain size range. Figure 1.11 shows a filtration protocol using three filtration steps, a prefiltration, tangential filtration and then a final filtration that produces particles approximately between 50 and

100 nm.[190] Each subsequent filtration step enriches the sample further but also adds to sample loss due to irreversible membrane adsorption.[191,192] Filtration is often done as a buffer exchange or concentration technique and is not a primary size selection technique except in specific applications.

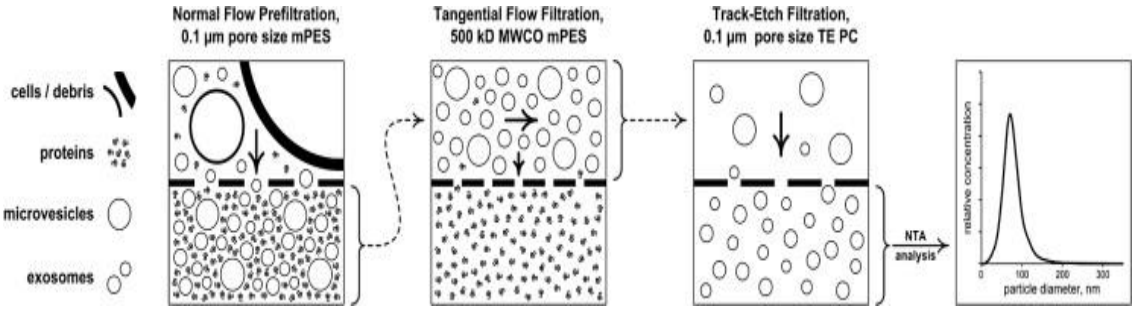

Figure 1.11 - Sequential filtration using different MWCO. The final product is an enriched sample between approximately 50 and 100 nm based on the average pore sizes. Reprinted from Reference 190.

1.6.4 - Immunoprecipitation

Immunoprecipitation uses functionalized nanoparticles or stationary phases to separate antigen presenting analytes from the matrix.[193–197] Commonly, magnetic beads are functionalized with anti-CD63/9/81, which can be separated by an external magnetic force.[198–201] Some care with this material is needed to make sure non-specific adsorption is minimized. Chemical conjugation with polyethylene glycol (PEG), glycine, or bovine serum albumin (BSA) irreversibly blocks the reactive sites after conjugation of the probes to the NP surface.[202,203] Immunoprecipitation has good specificity and simple operation, but recovery of the collected vesicles is more challenging as many of the disruption mechanisms to release the exosomes may also damage the proteins or lipid bilayer of the vesicle.

1.6.5 - Size Exclusion Chromatography

SEC is a liquid chromatography (LC) method utilizing a gel matrix to retain molecules based on size.[75,164,184,204–212] SEC utilizes micron sized beads with pores that allow molecular diffusion into the pores and around interstitial space between the packed beads. Larger pore sizes retain matrix components but allow the NP to pass by without much interaction. Figure 1.12 shows the difference between a small protein and large protein in an SEC column.[213] Smaller molecules will be retained longer because they have higher diffusivity into the pores, which results in more time in the stationary phase than larger molecules. Drawbacks to this approach lay mostly in the packing material and recovery.[204,214–216] SEC materials are somewhat expensive, and require care to maintain proper performance. This and the low yields are generally why SEC is not used for complex matrices like serum.[217,218] lipid interactions with the stationary phase have shown to cause large losses and sample retention in the column.[219–222] SEC is compatible with aqueous buffers, but pH, ionic strength and salt components can affect adsorption to the stationary phase and can limit buffer selection.

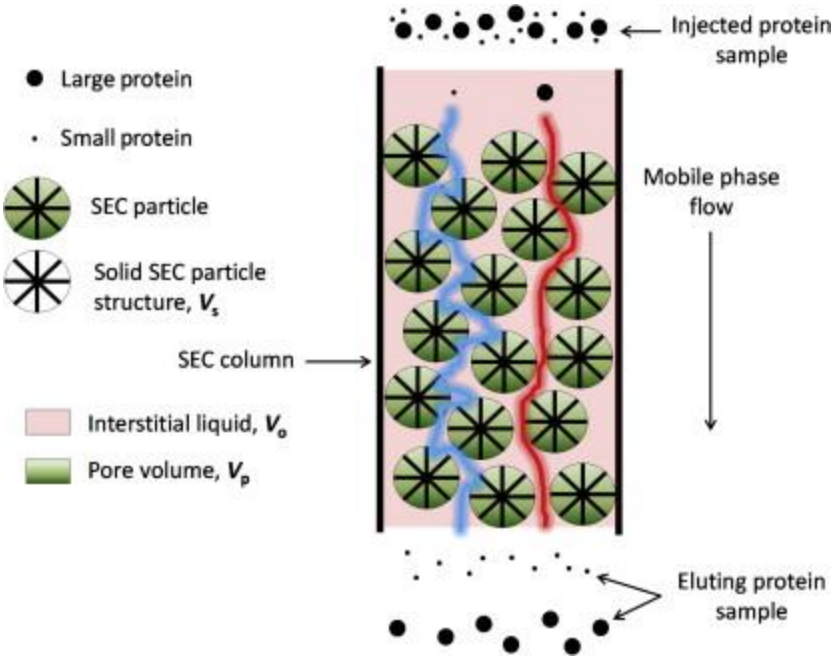

Figure 1.12 - SEC size separation theory. Larger particles diffuse less and take a straighter path through the column. Reprinted from Reference 213

1.6.6 - Field Flow Fractionation (FFF)

There are many kinds of FFF, such as thermal, centrifugal, and electrical which utilize different external forces to provide the orthogonal force needed for separation.[223–229] The most common design is AF4 which uses a flat channel with a vacuum pump pulling a cross flow through a porous membrane wall (Figure 1.13). The drag from the orthogonal flow acts as the separation force and the retention time is governed by crossflow intensity. The size range that FFF can separate is about ~1 nm to 10 um,[230,231] depending on the type of FFF used and the intensity of the separation forces used. Recovery of NPs in a native state is an advantage over other stressful isolation techniques. The gentle forces maintain the biocorona and separates native NPs in a stable buffer.[162,232–236] These advantages combined with the advantages and disadvantages of NTA were the basis of the work

presented in this dissertation. The following section goes into AF4 theory in more detail and describes the benefits over other isolation techniques.

1.7 - AF4 Theory

AF4 utilizes a particle's diffusion coefficient to separate different sized particles without the need of a stationary phase.[223,224,226,230] AF4 generates a velocity gradient between the laminar boundary layers. Particles with higher diffusion coefficients will diffuse higher in the channel and would have a faster average velocity (*v)* due to the velocity gradient created by the boundary layers of the laminar flow profile. Figure 1.13 shows a channel schematic and the parameters that drive the size separation. The following equation can estimate the retention time of a particle in channel:[226,237,238]

$$t_r = \frac{w^2}{6D}\ln(1 + \frac{F_{Cross}}{F_{Detector}}) \qquad (3)$$

With t_R being retention time, w being channel thickness, D is the particles diffusion coefficient in the separation medium, F_C is the cross flow and $F_{Detector}$ is the detector flow. The retention time directly relates to the average height from the membrane, so any factor that changes the height of the particle (F_C) or the laminar flow profile (w and $F_{Detector}$) will change the retention time.

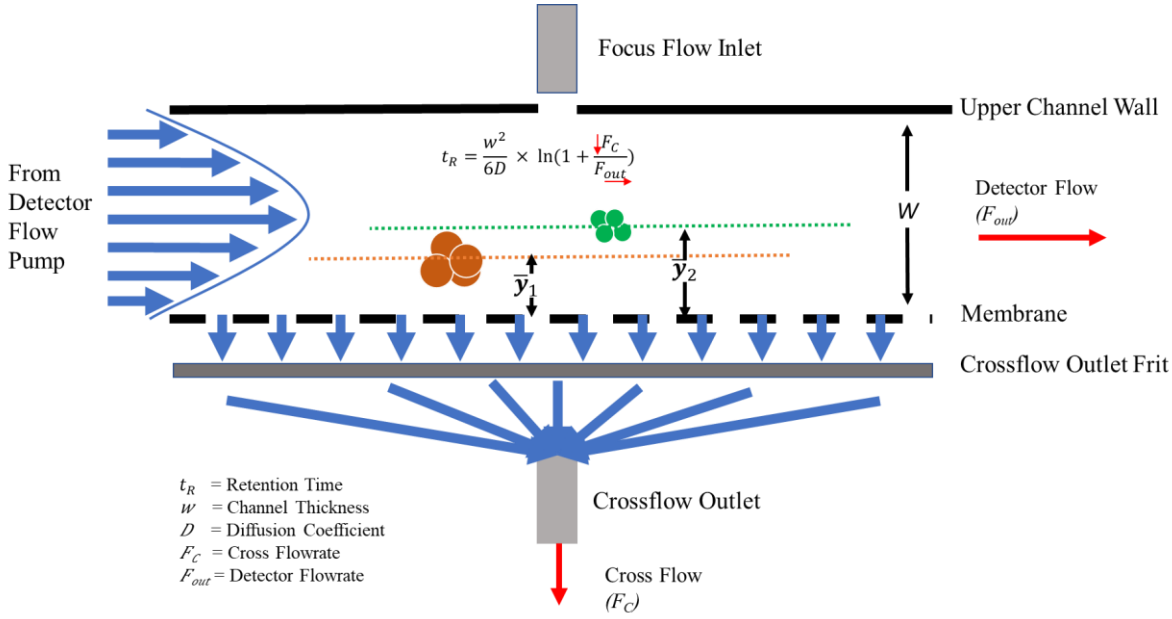

Figure 1.13 - Schematic showing the basis for separation in AF4. The retention time directly relates to the average height from the membrane, so any factor that changes the height of the particle (F_C) or the laminar flow profile (w and F_{out}) will change the retention time.

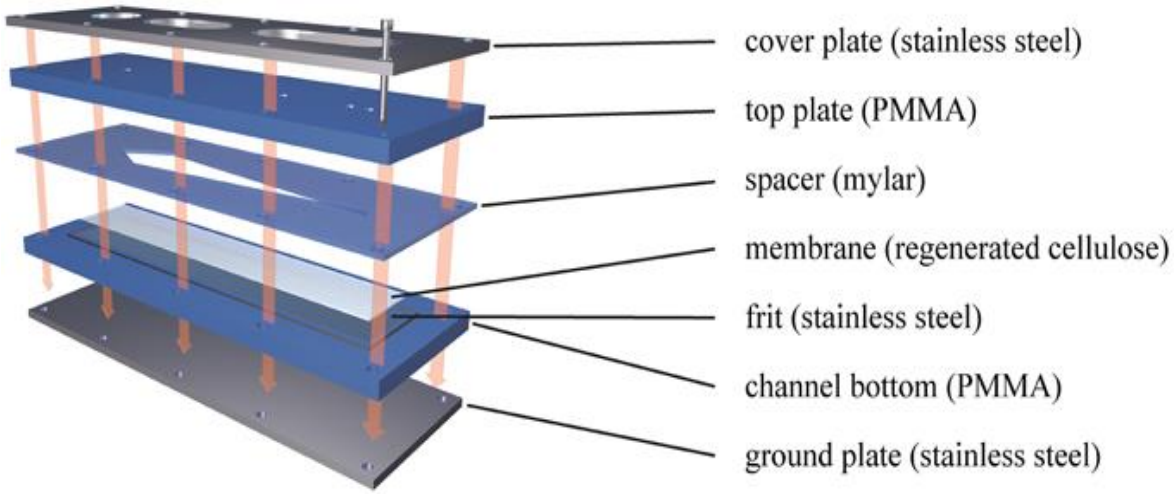

Figure 1.14 - Channel construction of an AF4 channel. The only consumable part is the separation membrane, which is much cheaper than column packing material but requires more frequent replacements. Reprinted from reference 231.

The main advantage of AF4 is the channel design. AF4 uses a channel constructed of a spacer between two plates (Figure 1.14).[231] The open channel does not have a stationary phase and removes shear forces between the stationary and mobile phases.[239–244] The buffer can be selected for the NP and is not selected to achieve sufficient elution from a stationary phase.[245,246] The low shear forces preserve aggregates, agglomerates, and biocorona as the NP is separated from the soluble matrix.[21,83,162,162,232–236] AF4's ability to gently separate a wide range of sizes and types of nanomaterials make it ideal for generalized NP isolation and analysis.

1.8 - Conclusion

NP analysis has many considerations and variables that make rapid and informative analysis difficult and time consuming. The motivation for the work in the following chapters are based on the need for simple, online particle counting, and sizing. NTA that can be connected to AF4 to analyze the eluent as NPs are separated by size. The individual counting of NTA make it ideal to be the first online nanoparticle detector for AF4, and the individual sizing increases performance by identifying multiple populations that may have coeluted together from the lower resolution that is a drawback of FFF. AF4 has broad applicability in NP separations and label free NTA can analyze the same broad types of NPs without the need for modifications from a native state. The coupling of the two together combined with the versatility of AF4 separation make it a versatile and capable NP characterization system.

1.9 - References

(1) Auffan, M.; Rose, J.; Bottero, J.-Y.; Lowry, G. V.; Jolivet, J.-P.; Wiesner, M. R. Towards a Definition of Inorganic Nanoparticles from an Environmental, Health and Safety Perspective. *Nat. Nanotechnol.* **2009**, *4* (10), 634–641. https://doi.org/10.1038/nnano.2009.242.

(2) Suttiponparnit, K.; Jiang, J.; Sahu, M.; Suvachittanont, S.; Charinpanitkul, T.; Biswas, P. Role of Surface Area, Primary Particle Size, and Crystal Phase on Titanium Dioxide Nanoparticle Dispersion Properties. *Nanoscale Res Lett* **2010**, *6* (1), 27. https://doi.org/10.1007/s11671-010-9772-1.

(3) Zhai, Y.; Dou, Y.; Liu, X.; Park, S. S.; Ha, C.-S.; Zhao, D. Soft-Template Synthesis of Ordered Mesoporous Carbon/Nanoparticle Nickel Composites with a High Surface Area. *Carbon* **2011**, *49* (2), 545–555. https://doi.org/10.1016/j.carbon.2010.09.055.

(4) Van Der Voort, P.; Esquivel, D.; De Canck, E.; Goethals, F.; Van Driessche, I.; Romero-Salguero, F. J. Periodic Mesoporous Organosilicas: From Simple to Complex Bridges; a Comprehensive Overview of Functions, Morphologies and Applications. *Chem Soc Rev* **2013**, *42* (9), 3913–3955. https://doi.org/10.1039/C2CS35222B.

(5) Park, S. S.; Santha Moorthy, M.; Ha, C.-S. Periodic Mesoporous Organosilicas for Advanced Applications. *NPG Asia Mater.* **2014**, *6* (4), e96–e96. https://doi.org/10.1038/am.2014.13.

(6) Croissant, J. G.; Cattoën, X.; Wong Chi Man, M.; Durand, J.-O.; Khashab, N. M. Syntheses and Applications of Periodic Mesoporous Organosilica Nanoparticles. *Nanoscale* **2015**, *7* (48), 20318–20334. https://doi.org/10.1039/C5NR05649G.

(7) Sharma, A.; Madhunapantula, S. V.; Robertson, G. P. Toxicological Considerations When Creating Nanoparticle-Based Drugs and Drug Delivery Systems. *Expert Opin. Drug Metab. Toxicol.* **2012**, *8* (1), 47–69. https://doi.org/10.1517/17425255.2012.637916.

(8) González-Gálvez, D.; Janer, G.; Vilar, G.; Vílchez, A.; Vázquez-Campos, S. The Life Cycle of Engineered Nanoparticles. In *Modelling the Toxicity of Nanoparticles*; Tran, L., Bañares, M. A., Rallo, R., Eds.; Advances in Experimental Medicine and Biology; Springer International Publishing: Cham, 2017; pp 41–69. https://doi.org/10.1007/978-3-319-47754-1_3.

(9) Khan, I.; Saeed, K.; Khan, I. Nanoparticles: Properties, Applications and Toxicities. *Arab. J. Chem.* **2019**, *12* (7), 908–931. https://doi.org/10.1016/j.arabjc.2017.05.011.

(10) BJNANO - Different endocytotic uptake mechanisms for nanoparticles in epithelial cells and macrophages https://www.beilstein-journals.org/bjnano/articles/2190-4286-5-174 (accessed 2021 -08 -01).

(11) Kuhn, D. A.; Vanhecke, D.; Michen, B.; Blank, F.; Gehr, P.; Petri-Fink, A.; Rothen-Rutishauser, B. Different Endocytotic Uptake Mechanisms for Nanoparticles in Epithelial Cells and Macrophages. *Beilstein J. Nanotechnol.* **2014**, *5* (1), 1625–1636. https://doi.org/10.3762/bjnano.5.174.

(12) Saha, K.; Kim, S. T.; Yan, B.; Miranda, O. R.; Alfonso, F. S.; Shlosman, D.; Rotello, V. M. Surface Functionality of Nanoparticles Determines Cellular Uptake Mechanisms in Mammalian Cells. *Small* **2013**, *9* (2), 300–305. https://doi.org/10.1002/smll.201201129.

(13) Agarwal, R.; Singh, V.; Jurney, P.; Shi, L.; Sreenivasan, S. V.; Roy, K. Mammalian Cells Preferentially Internalize Hydrogel Nanodiscs over Nanorods and Use Shape-Specific Uptake Mechanisms. *Proc. Natl. Acad. Sci.* **2013**, *110* (43), 17247–17252. https://doi.org/10.1073/pnas.1305000110.

(14) Herd, H.; Daum, N.; Jones, A. T.; Huwer, H.; Ghandehari, H.; Lehr, C.-M. Nanoparticle Geometry and Surface Orientation Influence Mode of Cellular Uptake. *ACS Nano* **2013**, *7* (3), 1961–1973. https://doi.org/10.1021/nn304439f.

(15) Kettler, K.; Veltman, K.; Meent, D. van de; Wezel, A. van; Hendriks, A. J. Cellular Uptake of Nanoparticles as Determined by Particle Properties, Experimental Conditions, and Cell Type. *Environ. Toxicol. Chem.* **2014**, *33* (3), 481–492. https://doi.org/10.1002/etc.2470.

(16) Manzanares, D.; Ceña, V. Endocytosis: The Nanoparticle and Submicron Nanocompounds Gateway into the Cell. *Pharmaceutics* **2020**, *12* (4), 371. https://doi.org/10.3390/pharmaceutics12040371.

(17) Westmeier, D.; Stauber, R. H.; Docter, D. The Concept of Bio-Corona in Modulating the Toxicity of Engineered Nanomaterials (ENM). *Toxicol. Appl. Pharmacol.* **2016**, *299*, 53–57. https://doi.org/10.1016/j.taap.2015.11.008.

(18) Bhattacharya, K.; Mukherjee, S. P.; Gallud, A.; Burkert, S. C.; Bistarelli, S.; Bellucci, S.; Bottini, M.; Star, A.; Fadeel, B. Biological Interactions of Carbon-Based Nanomaterials: From Coronation to Degradation. *Nanomedicine Nanotechnol. Biol. Med.* **2016**, *12* (2), 333–351. https://doi.org/10.1016/j.nano.2015.11.011.

(19) Neagu, M.; Piperigkou, Z.; Karamanou, K.; Engin, A. B.; Docea, A. O.; Constantin, C.; Negrei, C.; Nikitovic, D.; Tsatsakis, A. Protein Bio-Corona:

Critical Issue in Immune Nanotoxicology. *Arch. Toxicol.* **2017**, *91* (3), 1031–1048. https://doi.org/10.1007/s00204-016-1797-5.

(20) Vilanova, O.; Mittag, J. J.; Kelly, P. M.; Milani, S.; Dawson, K. A.; Rädler, J. O.; Franzese, G. Understanding the Kinetics of Protein–Nanoparticle Corona Formation. *ACS Nano* **2016**, *10* (12), 10842–10850. https://doi.org/10.1021/acsnano.6b04858.

(21) Liu, W.; Rose, J.; Plantevin, S.; Auffan, M.; Bottero, J.-Y.; Vidaud, C. Protein Corona Formation for Nanomaterials and Proteins of a Similar Size: Hard or Soft Corona? *Nanoscale* **2013**, *5* (4), 1658–1668. https://doi.org/10.1039/c2nr33611a.

(22) Bertrand, N.; Grenier, P.; Mahmoudi, M.; Lima, E. M.; Appel, E. A.; Dormont, F.; Lim, J.-M.; Karnik, R.; Langer, R.; Farokhzad, O. C. Mechanistic Understanding of in Vivo Protein Corona Formation on Polymeric Nanoparticles and Impact on Pharmacokinetics. *Nat. Commun.* **2017**, *8* (1), 777. https://doi.org/10.1038/s41467-017-00600-w.

(23) Yu, Q.; Zhao, L.; Guo, C.; Yan, B.; Su, G. Regulating Protein Corona Formation and Dynamic Protein Exchange by Controlling Nanoparticle Hydrophobicity. *Front. Bioeng. Biotechnol.* **2020**, *0*. https://doi.org/10.3389/fbioe.2020.00210.

(24) Huang, Y.-W.; Cambre, M.; Lee, H.-J. The Toxicity of Nanoparticles Depends on Multiple Molecular and Physicochemical Mechanisms. *Int. J. Mol. Sci.* **2017**, *18* (12), 2702. https://doi.org/10.3390/ijms18122702.

(25) Bahadar, H.; Maqbool, F.; Niaz, K.; Abdollahi, M. Toxicity of Nanoparticles and an Overview of Current Experimental Models. *Iran Biomed J* 11.

(26) Elkin, S. R.; Lakoduk, A. M.; Schmid, S. L. Endocytic Pathways and Endosomal Trafficking: A Primer. *Wien. Med. Wochenschr. 1946* **2016**, *166* (7–8), 196–204. https://doi.org/10.1007/s10354-016-0432-7.

(27) Aguilar, R. C.; Wendland, B. Endocytosis of Membrane Receptors: Two Pathways Are Better than One. *Proc. Natl. Acad. Sci.* **2005**, *102* (8), 2679–2680. https://doi.org/10.1073/pnas.0500213102.

(28) Grant, B. D.; Donaldson, J. G. Pathways and Mechanisms of Endocytic Recycling. *Nat. Rev. Mol. Cell Biol.* **2009**, *10* (9), 597–608. https://doi.org/10.1038/nrm2755.

(29) Gruenberg, J. The Endocytic Pathway: A Mosaic of Domains. *Nat. Rev. Mol. Cell Biol.* **2001**, *2* (10), 721–730. https://doi.org/10.1038/35096054.

(30) Manshian, B. B.; Pokhrel, S.; Mädler, L.; Soenen, S. J. The Impact of Nanoparticle-Driven Lysosomal Alkalinization on Cellular Functionality. *J. Nanobiotechnology* **2018**, *16* (1), 85. https://doi.org/10.1186/s12951-018-0413-7.

(31) Fröhlich, E. Cellular Elimination of Nanoparticles. *Environ. Toxicol. Pharmacol.* **2016**, *46*, 90–94. https://doi.org/10.1016/j.etap.2016.07.003.

(32) Sabella, S.; P. Carney, R.; Brunetti, V.; Ada Malvindi, M.; Al-Juffali, N.; Vecchio, G.; M. Janes, S.; M. Bakr, O.; Cingolani, R.; Stellacci, F.; Paolo Pompa, P. A General Mechanism for Intracellular Toxicity of Metal-Containing Nanoparticles. *Nanoscale* **2014**, *6* (12), 7052–7061. https://doi.org/10.1039/C4NR01234H.

(33) Halamoda Kenzaoui, B.; Chapuis Bernasconi, C.; Guney-Ayra, S.; Juillerat-Jeanneret, L. Induction of Oxidative Stress, Lysosome Activation and Autophagy by Nanoparticles in Human Brain-Derived Endothelial Cells. *Biochem. J.* **2012**, *441* (3), 813–821. https://doi.org/10.1042/BJ20111252.

(34) Wang, F.; Salvati, A.; Boya, P. Lysosome-Dependent Cell Death and Deregulated Autophagy Induced by Amine-Modified Polystyrene Nanoparticles. *Open Biol. 8* (4), 170271. https://doi.org/10.1098/rsob.170271.

(35) Deng, J.; Gao, C. Recent Advances in Interactions of Designed Nanoparticles and Cells with Respect to Cellular Uptake, Intracellular Fate, Degradation and Cytotoxicity. *Nanotechnology* **2016**, *27* (41), 412002. https://doi.org/10.1088/0957-4484/27/41/412002.

(36) Peng, L.; Fu, D.; Qi, H.; Lan, C. Q.; Yu, H.; Ge, C. Micro- and Nano-Plastics in Marine Environment: Source, Distribution and Threats — A Review. *Sci. Total Environ.* **2020**, *698*, 134254. https://doi.org/10.1016/j.scitotenv.2019.134254.

(37) Chae, Y.; An, Y.-J. Effects of Micro- and Nanoplastics on Aquatic Ecosystems: Current Research Trends and Perspectives. *Mar. Pollut. Bull.* **2017**, *124* (2), 624–632. https://doi.org/10.1016/j.marpolbul.2017.01.070.

(38) Revel, M.; Châtel, A.; Mouneyrac, C. Micro(Nano)Plastics: A Threat to Human Health? *Curr. Opin. Environ. Sci. Health* **2018**, *1*, 17–23. https://doi.org/10.1016/j.coesh.2017.10.003.

(39) Chang, X.; Xue, Y.; Li, J.; Zou, L.; Tang, M. Potential Health Impact of Environmental Micro- and Nanoplastics Pollution. *J. Appl. Toxicol.* **2020**, *40* (1), 4–15. https://doi.org/10.1002/jat.3915.

(40) Pinto da Costa, J.; Reis, V.; Paço, A.; Costa, M.; Duarte, A. C.; Rocha-Santos, T. Micro(Nano)Plastics – Analytical Challenges towards Risk Evaluation. *TrAC*

Trends Anal. Chem. **2019**, *111*, 173–184. https://doi.org/10.1016/j.trac.2018.12.013.

(41) Kumar, M.; Chen, H.; Sarsaiya, S.; Qin, S.; Liu, H.; Awasthi, M. K.; Kumar, S.; Singh, L.; Zhang, Z.; Bolan, N. S.; Pandey, A.; Varjani, S.; Taherzadeh, M. J. Current Research Trends on Micro- and Nano-Plastics as an Emerging Threat to Global Environment: A Review. *J. Hazard. Mater.* **2021**, *409*, 124967. https://doi.org/10.1016/j.jhazmat.2020.124967.

(42) Oliveri Conti, G.; Ferrante, M.; Banni, M.; Favara, C.; Nicolosi, I.; Cristaldi, A.; Fiore, M.; Zuccarello, P. Micro- and Nano-Plastics in Edible Fruit and Vegetables. The First Diet Risks Assessment for the General Population. *Environ. Res.* **2020**, *187*, 109677. https://doi.org/10.1016/j.envres.2020.109677.

(43) Nie, H.; Li, M.; Li, Q.; Liang, S.; Tan, Y.; Sheng, L.; Shi, W.; Zhang, S. X. A.; Hui Nie, Minjie Li, Quanshun Li, Shaojun Liang, Yingying Tan, Lan Sheng, W. S. and S. X.-A. Z. Carbon Dots with Continuously Tunable Full-Colour Emission and Their Application in Ratiometric PH Sensing. *Chem. Mater.* **2014**, *26* (10), 3104–3112. https://doi.org/10.1021/cm5003669.

(44) Pankhurst, Q. A.; Connolly, J.; Jones, S. K.; Dobson, J. Applications of Magnetic Nanoparticles in Biomedicine. *J. Phys. Appl. Phys.* **2003**, *36* (13), R167–R181. https://doi.org/10.1088/0022-3727/36/13/201.

(45) Eustis, S.; el-Sayed, M. A. Why Gold Nanoparticles Are More Precious than Pretty Gold: Noble Metal Surface Plasmon Resonance and Its Enhancement of the Radiative and Nonradiative Properties of Nanocrystals of Different Shapes. *Chem. Soc. Rev.* **2006**, *35* (3), 209–217. https://doi.org/10.1039/b514191e.

(46) Ding, C.; Zhu, A.; Tian, Y. Functional Surface Engineering of C-Dots for Fluorescent Biosensing and in Vivo Bioimaging. *Acc. Chem. Res.* **2014**, *47* (1), 20–30. https://doi.org/10.1021/ar400023s.

(47) Jiang, S.; Win, K. Y.; Liu, S.; Teng, C. P.; Zheng, Y.; Han, M.-Y. Surface-Functionalized Nanoparticles for Biosensing and Imaging-Guided Therapeutics. *Nanoscale* **2013**, *5* (8), 3127–3148. https://doi.org/10.1039/c3nr34005h.

(48) Montalti, M.; Prodi, L.; Rampazzo, E.; Zaccheroni, N. Dye-Doped Silica Nanoparticles as Luminescent Organized Systems for Nanomedicine. *Chem. Soc. Rev.* **2014**, *43* (12), 4243–4268. https://doi.org/10.1039/c3cs60433k.

(49) Wang, Y.; Hu, A. Carbon Quantum Dots: Synthesis, Properties and Applications. *J. Mater. Chem. C* **2014**, *2* (34), 6921. https://doi.org/10.1039/C4TC00988F.

(50) Ding, X.; Ding, G.; Xie, X.; Huang, F.; Jiang, M. Direct Growth of Few Layer Graphene on Hexagonal Boron Nitride by Chemical Vapor Deposition. *Carbon* **2011**, *49* (7), 2522–2525. https://doi.org/10.1016/j.carbon.2011.02.022.

(51) Shi, X.; Zhou, F.; Peng, J.; Wu, R.; Wu, Z.-S.; Bao, X. One-Step Scalable Fabrication of Graphene-Integrated Micro-Supercapacitors with Remarkable Flexibility and Exceptional Performance Uniformity. *Adv. Funct. Mater.* **2019**, *29* (50), 1902860. https://doi.org/10.1002/adfm.201902860.

(52) Puster, M.; Balan, A.; Rodríguez-Manzo, J. A.; Danda, G.; Ahn, J.-H.; Parkin, W.; Drndi, M. Graphene Nanoribbon-Nanopore Sensors for Single Molecule Detection. 7.

(53) Min, S. K.; Kim, W. Y.; Cho, Y.; Kim, K. S. Fast DNA Sequencing with a Graphene-Based Nanochannel Device. *Nat. Nanotechnol.* **2011**, *6* (3), 162–165. https://doi.org/10.1038/nnano.2010.283.

(54) Teixeira, S.; Burwell, G.; Castaing, A.; Gonzalez, D.; Conlan, R. S.; Guy, O. J. Epitaxial Graphene Immunosensor for Human Chorionic Gonadotropin. *Sens. Actuators B Chem.* **2014**, *190*, 723–729. https://doi.org/10.1016/j.snb.2013.09.019.

(55) Jeyaraj, M.; Gurunathan, S.; Qasim, M.; Kang, M.-H.; Kim, J.-H. A Comprehensive Review on the Synthesis, Characterization, and Biomedical Application of Platinum Nanoparticles. *Nanomaterials* **2019**, *9* (12), 1719. https://doi.org/10.3390/nano9121719.

(56) Temizel-Sekeryan, S.; Hicks, A. L. Global Environmental Impacts of Silver Nanoparticle Production Methods Supported by Life Cycle Assessment. *Resour. Conserv. Recycl.* **2020**, *156*, 104676. https://doi.org/10.1016/j.resconrec.2019.104676.

(57) Stavis, S. M.; Fagan, J. A.; Stopa, M.; Liddle, J. A. Nanoparticle Manufacturing – Heterogeneity through Processes to Products. *ACS Appl. Nano Mater.* **2018**, *1* (9), 4358–4385. https://doi.org/10.1021/acsanm.8b01239.

(58) Tsuzuki, T. Commercial Scale Production of Inorganic Nanoparticles. *Int. J. Nanotechnol.* **2009**, *6* (5–6), 567–578. https://doi.org/10.1504/IJNT.2009.024647.

(59) Kosinova, A.; Wang, D.; Baradács, E.; Parditka, B.; Kups, T.; Klinger, L.; Erdélyi, Z.; Schaaf, P.; Rabkin, E. Tuning the Nanoscale Morphology and Optical Properties of Porous Gold Nanoparticles by Surface Passivation and Annealing. *Acta Mater.* **2017**, *127*, 108–116. https://doi.org/10.1016/j.actamat.2017.01.014.

(60) Matoussevitch, N.; Gorschinski, A.; Habicht, W.; Bolle, J.; Dinjus, E.; Bönnemann, H.; Behrens, S. Surface Modification of Metallic Co Nanoparticles. *J. Magn. Magn. Mater.* **2007**, *311* (1), 92–96. https://doi.org/10.1016/j.jmmm.2006.10.1203.

(61) Liang, S.; Zhang, M.; He, Y.; Kang, Z.; Tian, M.; Zhang, M.; Miao, H.; Lin, Z. Polymer-Ligated Uniform Lead Chalcogenide Nanoparticles with Tunable Size and Robust Stability Enabled by Judiciously Designed Surface Chemistry. *Chem. Mater.* **2021**. https://doi.org/10.1021/acs.chemmater.1c01132.

(62) Morais, E.; Moloney, C.; O'Modhrain, C.; McKiernan, E.; Brougham, D. F.; Sullivan, J. A. Enhanced Stability and Emission Properties of Perylene Dyes by Surface Tethering: Preparation of Fluorescent Ru Nanoparticle Suspensions by Alkyne Linker Chemistry. *Chem. – Eur. J.* **2021**, *27* (3), 1023–1030. https://doi.org/10.1002/chem.202003514.

(63) Trompoukis, C.; Feng, J.-Y.; Bosserez, T.; Rongé, J.; Dendooven, J.; Detavernier, C.; Baets, R.; A. Martens, J. ALD Pt Nanoparticles and Thin-Film Coatings Enhancing the Stability and Performance of Silicon Photocathodes for Solar Water Splitting. *Sustain. Energy Fuels* **2021**, *5* (12), 3115–3123. https://doi.org/10.1039/D1SE00293G.

(64) Derjaguin, B.; Landau, L. Theory of the Stability of Strongly Charged Lyophobic Sols and of the Adhesion of Strongly Charged Particles in Solutions of Electrolytes. *Prog. Surf. Sci.* **1993**, *43* (1), 30–59. https://doi.org/10.1016/0079-6816(93)90013-L.

(65) Verwey, E. J. W. Theory of the Stability of Lyophobic Colloids. 6.

(66) Brennan, K.; Martin, K.; FitzGerald, S. P.; O'Sullivan, J.; Wu, Y.; Blanco, A.; Richardson, C.; Mc Gee, M. M. A Comparison of Methods for the Isolation and Separation of Extracellular Vesicles from Protein and Lipid Particles in Human Serum. *Sci. Rep.* **2020**, *10* (1), 1039. https://doi.org/10.1038/s41598-020-57497-7.

(67) Helwa, I.; Cai, J.; Drewry, M. D.; Zimmerman, A.; Dinkins, M. B.; Khaled, M. L.; Seremwe, M.; Dismuke, W. M.; Bieberich, E.; Stamer, W. D.; Hamrick, M. W.; Liu, Y. A Comparative Study of Serum Exosome Isolation Using Differential Ultracentrifugation and Three Commercial Reagents. *PLOS ONE* **2017**, *12* (1), e0170628. https://doi.org/10.1371/journal.pone.0170628.

(68) Akers, J. C.; Gonda, D.; Kim, R.; Carter, B. S.; Chen, C. C. Biogenesis of Extracellular Vesicles (EV): Exosomes, Microvesicles, Retrovirus-like Vesicles, and Apoptotic Bodies. *J. Neurooncol.* **2013**, *113* (1), 1–11. https://doi.org/10.1007/s11060-013-1084-8.

(69) Simonsen, J. B. What Are We Looking At? Extracellular Vesicles, Lipoproteins, or Both? *Circ. Res.* **2017**, *121* (8), 920–922. https://doi.org/10.1161/CIRCRESAHA.117.311767.

(70) György, B.; Szabó, T. G.; Pásztói, M.; Pál, Z.; Misják, P.; Aradi, B.; László, V.; Pállinger, É.; Pap, E.; Kittel, Á.; Nagy, G.; Falus, A.; Buzás, E. I. Membrane Vesicles, Current State-of-the-Art: Emerging Role of Extracellular Vesicles. *Cell. Mol. Life Sci.* **2011**, *68* (16), 2667–2688. https://doi.org/10.1007/s00018-011-0689-3.

(71) Havugimana, P. C.; Hart, G. T.; Nepusz, T.; Yang, H.; Turinsky, A. L.; Li, Z.; Wang, P. I.; Boutz, D. R.; Fong, V.; Phanse, S.; Babu, M.; Craig, S. A.; Hu, P.; Wan, C.; Vlasblom, J.; Dar, V.-N.; Bezginov, A.; Clark, G. W.; Wu, G. C.; Wodak, S. J.; Tillier, E. R. M.; Paccanaro, A.; Marcotte, E. M.; Emili, A. A Census of Human Soluble Protein Complexes. *Cell* **2012**, *150* (5), 1068–1081. https://doi.org/10.1016/j.cell.2012.08.011.

(72) De, S.; Klenerman, D. Imaging Individual Protein Aggregates to Follow Aggregation and Determine the Role of Aggregates in Neurodegenerative Disease. *Biochim. Biophys. Acta Proteins Proteomics* **2019**, *1867* (10), 870–878. https://doi.org/10.1016/j.bbapap.2018.12.010.

(73) Falsone, A.; Falsone, S. F. Legal but Lethal: Functional Protein Aggregation at the Verge of Toxicity. *Front. Cell. Neurosci.* **2015**, *0*. https://doi.org/10.3389/fncel.2015.00045.

(74) Pardeshi, N. N.; Zhou, C.; Randolph, T. W.; Carpenter, J. F. Protein Nanoparticles Promote Microparticle Formation in Intravenous Immunoglobulin Solutions During Freeze-Thawing and Agitation Stresses. *J. Pharm. Sci.* **2018**, *107* (7), 1852–1857. https://doi.org/10.1016/j.xphs.2018.03.016.

(75) Carpenter, J. F.; Randolph, T. W.; Jiskoot, W.; Crommelin, D. J. A.; Middaugh, C. R.; Winter, G. Potential Inaccurate Quantitation and Sizing of Protein Aggregates by Size Exclusion Chromatography: Essential Need to Use Orthogonal Methods to Assure the Quality of Therapeutic Protein Products. *J. Pharm. Sci.* **2010**, *99* (5), 2200–2208. https://doi.org/10.1002/jps.21989.

(76) Gerhardt, A.; Mcgraw, N. R.; Schwartz, D. K.; Bee, J. S.; Carpenter, J. F.; Randolph, T. W. Protein Aggregation and Particle Formation in Prefilled Glass Syringes. *J. Pharm. Sci.* **2014**, *103* (6), 1601–1612. https://doi.org/10.1002/jps.23973.

(77) Puhl, S.; Meinel, L.; Germershaus, O. Recent Advances in Crystalline and Amorphous Particulate Protein Formulations for Controlled Delivery. *Asian J. Pharm. Sci.* **2016**, *11* (4), 469–477. https://doi.org/10.1016/j.ajps.2016.06.003.

(78) Sahin, E.; Grillo, A. O.; Perkins, M. D.; Roberts, C. J. Comparative Effects of PH and Ionic Strength on Protein-Protein Interactions, Unfolding, and Aggregation for IgG1 Antibodies. *J. Pharm. Sci.* **2010**, *99* (12), 4830–4848. https://doi.org/10.1002/jps.22198.

(79) Kuklenyik, Z.; Jones, J. I.; Gardner, M. S.; Schieltz, D. M.; Parks, B. A.; Toth, C. A.; Rees, J. C.; Andrews, M. L.; Carter, K.; Lehtikoski, A. K.; McWilliams, L. G.; Williamson, Y. M.; Bierbaum, K. P.; Pirkle, J. L.; Barr, J. R. Core Lipid, Surface Lipid and Apolipoprotein Composition Analysis of Lipoprotein Particles as a Function of Particle Size in One Workflow Integrating Asymmetric Flow Field-Flow Fractionation and Liquid Chromatography-Tandem Mass Spectrometry. *PLOS ONE* **2018**, *13* (4), e0194797. https://doi.org/10.1371/journal.pone.0194797.

(80) Lee, J. H.; Yang, J. S.; Lee, S.-H.; Moon, M. H. Analysis of Lipoprotein-Specific Lipids in Patients with Acute Coronary Syndrome by Asymmetrical Flow Field-Flow Fractionation and Nanoflow Liquid Chromatography-Tandem Mass Spectrometry. *J. Chromatogr. B* **2018**, *1099*, 56–63. https://doi.org/10.1016/J.JCHROMB.2018.09.016.

(81) Kuklenyik, Z.; Gardner, M. S.; Parks, B. A.; Schieltz, D. M.; Rees, J. C.; Mcwilliams, L. G.; Williamson, Y. M.; Pirkle, J. L.; Barr, J. R. Multivariate DoE Optimization of Asymmetric Flow Field Flow Fractionation Coupled to Quantitative LC-MS/MS for Analysis of Lipoprotein Subclasses. *Chromatography* **2015**, *2*, 96–117. https://doi.org/10.3390/chromatography2010096.

(82) Feingold, K. R.; Grunfeld, C. *Introduction to Lipids and Lipoproteins*; MDText.com, Inc., 2000.

(83) Lima, T.; Bernfur, K.; Vilanova, M.; Cedervall, T. Understanding the Lipid and Protein Corona Formation on Different Sized Polymeric Nanoparticles. *Sci. Rep.* **2020**, *10* (1), 1129. https://doi.org/10.1038/s41598-020-57943-6.

(84) Ridker, P. M.; Rifai, N.; Cook, N. R.; Bradwin, G.; Buring, J. E. Non HDL Cholesterol, Apolipoproteins A-I and B100, Standard Lipid Measures, Lipid Ratios, and CRP as Risk Factors for Cardiovascular Disease in Women. 8.

(85) German, J. B.; Smilowitz, J. T.; Zivkovic, A. M. Lipoproteins: When Size Really Matters. *Curr. Opin. Colloid Interface Sci.* **2006**, *11* (2–3), 171–183. https://doi.org/10.1016/j.cocis.2005.11.006.

(86) Willms, E.; Johansson, H. J.; Mäger, I.; Lee, Y.; Blomberg, K. E. M.; Sadik, M.; Alaarg, A.; Smith, C. I. E.; Lehtiö, J.; EL Andaloussi, S.; Wood, M. J. A.; Vader, P. Cells Release Subpopulations of Exosomes with Distinct Molecular and

Biological Properties. *Sci. Rep.* **2016**, *6* (1), 22519. https://doi.org/10.1038/srep22519.

(87) Zhang, H.; Freitas, D.; Kim, H. S.; Fabijanic, K.; Li, Z.; Chen, H.; Mark, M. T.; Molina, H.; Martin, A. B.; Bojmar, L.; Fang, J.; Rampersaud, S.; Hoshino, A.; Matei, I.; Kenific, C. M.; Nakajima, M.; Mutvei, A. P.; Sansone, P.; Buehring, W.; Wang, H.; Jimenez, J. P.; Cohen-Gould, L.; Paknejad, N.; Brendel, M.; Manova-Todorova, K.; Magalhães, A.; Ferreira, J. A.; Osório, H.; Silva, A. M.; Massey, A.; Cubillos-Ruiz, J. R.; Galletti, G.; Giannakakou, P.; Cuervo, A. M.; Blenis, J.; Schwartz, R.; Brady, M. S.; Peinado, H.; Bromberg, J.; Matsui, H.; Reis, C. A.; Lyden, D. Identification of Distinct Nanoparticles and Subsets of Extracellular Vesicles by Asymmetric Flow Field-Flow Fractionation. *Nat. Cell Biol.* **2018**, *20* (3), 332–343. https://doi.org/10.1038/s41556-018-0040-4.

(88) Théry, C.; Zitvogel, L.; Amigorena, S. Exosomes: Composition, Biogenesis and Function. *Nat. Rev. Immunol. Publ. Online 01 August 2002 Doi101038nri855* **2002**, *2* (8), 569. https://doi.org/10.1038/NRI855.

(89) Colombo, M.; Raposo, G.; Théry, C. Biogenesis, Secretion, and Intercellular Interactions of Exosomes and Other Extracellular Vesicles. *Annu. Rev. Cell Dev. Biol.* **2014**, *30* (1), 255–289. https://doi.org/10.1146/annurev-cellbio-101512-122326.

(90) Belov, L.; Matic, K. J.; Hallal, S.; Best, O. G.; Mulligan, S. P.; Christopherson, R. I. Extensive Surface Protein Profiles of Extracellular Vesicles from Cancer Cells May Provide Diagnostic Signatures from Blood Samples. *J. Extracell. Vesicles* **2016**, *5* (1), 25355. https://doi.org/10.3402/jev.v5.25355.

(91) Nilsson, J.; Skog, J.; Nordstrand, A.; Baranov, V.; Mincheva-Nilsson, L.; Breakefield, X. O.; Widmark, A. Prostate Cancer-Derived Urine Exosomes: A Novel Approach to Biomarkers for Prostate Cancer. *Br. J. Cancer* **2009**, *100* (10), 1603–1607. https://doi.org/10.1038/sj.bjc.6605058.

(92) Huang, T.; Deng, C.-X. Current Progresses of Exosomes as Cancer Diagnostic and Prognostic Biomarkers. *Int. J. Biol. Sci.* **2019**, *15* (1), 1–11. https://doi.org/10.7150/ijbs.27796.

(93) Yang, J. S.; Lee, J. C.; Byeon, S. K.; Rha, K. H.; Moon, M. H. Size Dependent Lipidomic Analysis of Urinary Exosomes from Patients with Prostate Cancer by Flow Field-Flow Fractionation and Nanoflow Liquid Chromatography-Tandem Mass Spectrometry. *Anal. Chem.* **2017**, *89* (4), 2488–2496. https://doi.org/10.1021/acs.analchem.6b04634.

(94) Johnstone, R. M. Exosomes Biological Significance: A Concise Review. *Blood Cells. Mol. Dis.* **2006**, *36* (2), 315–321. https://doi.org/10.1016/j.bcmd.2005.12.001.

(95) Lea, J.; Sharma, R.; Yang, F.; Zhu, H.; Ward, E. S.; Schroit, A. J. Detection of Phosphatidylserine-Positive Exosomes as a Diagnostic Marker for Ovarian Malignancies: A Proof of Concept Study. *Oncotarget* **2017**, *8* (9), 14395–14407. https://doi.org/10.18632/oncotarget.14795.

(96) Howitt, J.; Hill, A. F. Exosomes in the Pathology of Neurodegenerative Diseases. *J. Biol. Chem.* **2016**, *291* (52), 26589–26597. https://doi.org/10.1074/jbc.R116.757955.

(97) Maia, J.; Caja, S.; Strano Moraes, M. C.; Couto, N.; Costa-Silva, B. Exosome-Based Cell-Cell Communication in the Tumor Microenvironment. *Front. Cell Dev. Biol.* **2018**, *0*. https://doi.org/10.3389/fcell.2018.00018.

(98) Corrado, C.; Raimondo, S.; Chiesi, A.; Ciccia, F.; De Leo, G.; Alessandro, R. Exosomes as Intercellular Signaling Organelles Involved in Health and Disease: Basic Science and Clinical Applications. *Int. J. Mol. Sci.* **2013**, *14* (3), 5338–5366. https://doi.org/10.3390/ijms14035338.

(99) Lotvall, J.; Valadi, H. Cell to Cell Signalling via Exosomes Through EsRNA. *Cell Adhes. Migr.* **2007**, *1* (3), 156–158.

(100) Men, Y.; Yelick, J.; Jin, S.; Tian, Y.; Chiang, M. S. R.; Higashimori, H.; Brown, E.; Jarvis, R.; Yang, Y. Exosome Reporter Mice Reveal the Involvement of Exosomes in Mediating Neuron to Astroglia Communication in the CNS. *Nat. Commun.* **2019**, *10* (1), 4136. https://doi.org/10.1038/s41467-019-11534-w.

(101) Dai, J.; Su, Y.; Zhong, S.; Cong, L.; Liu, B.; Yang, J.; Tao, Y.; He, Z.; Chen, C.; Jiang, Y. Exosomes: Key Players in Cancer and Potential Therapeutic Strategy. *Signal Transduct. Target. Ther.* **2020**, *5* (1), 1–10. https://doi.org/10.1038/s41392-020-00261-0.

(102) Zhang, H.-G.; Grizzle, W. E. Exosomes: A Novel Pathway of Local and Distant Intercellular Communication That Facilitates the Growth and Metastasis of Neoplastic Lesions. *Am. J. Pathol.* **2014**, *184* (1), 28–41. https://doi.org/10.1016/j.ajpath.2013.09.027.

(103) Simons, M.; Raposo, G. Exosomes – Vesicular Carriers for Intercellular Communication. *Curr. Opin. Cell Biol.* **2009**, *21* (4), 575–581. https://doi.org/10.1016/j.ceb.2009.03.007.

(104) Martins, V. R.; Dias, M. S.; Hainaut, P. Tumor-Cell-Derived Microvesicles as Carriers of Molecular Information in Cancer. *Curr. Opin. Oncol.* **2013**, *25* (1), 66–75. https://doi.org/10.1097/CCO.0b013e32835b7c81.

(105) Shen, M.; Di, K.; He, H.; Xia, Y.; Xie, H.; Huang, R.; Liu, C.; Yang, M.; Zheng, S.; He, N.; Li, Z. Progress in Exosome Associated Tumor Markers and Their Detection Methods. *Mol. Biomed.* **2020**, *1* (1), 3. https://doi.org/10.1186/s43556-020-00002-3.

(106) Flack, K.; Jimenez, L. A.; Zhong, W. Analysis of the Distribution Profiles of Circulating MicroRNAs by Asymmetrical Flow Field Flow Fractionation. *Methods Mol. Biol. Clifton NJ* **2017**, *1509*, 161–168. https://doi.org/10.1007/978-1-4939-6524-3_15.

(107) Andreu, Z.; YÃ¡Ã±ez-MÃ[3], M. Tetraspanins in Extracellular Vesicle Formation and Function. *Front. Immunol.* **2014**, *5*. https://doi.org/10.3389/fimmu.2014.00442.

(108) Wu, Y.; Deng, W.; Klinke, D. J.; Klinke II, D. J.; Théry, C.; Ostrowski, M. C.; Segura, E.; Andaloussi, S. E.; Mäger, I.; Breakefield, X. O.; Wood, M. J.; Robbins, P. D.; Morelli, A. E.; Harding, C.; Heuser, J.; Stahl, P.; Pan, B. T.; Teng, K.; Wu, C.; Adam, M.; Johnstone, R. M.; Valadi, H.; Ekström, K.; Bossios, A.; Sjöstrand, M.; Lee, J. J.; Lötvall, J. O.; Skog, J.; Würdinger, T.; Rijn, S. van; Meijer, D. H.; Gainche, L.; Sena-Esteves, M.; Curry, W. T.; Carter, B. S.; Krichevsky, A. M.; Breakefield, X. O.; Taylor, D. D.; Gercel-Taylor, C.; Al-Nedawi, K.; Meehan, B.; Micallef, J.; Lhotak, V.; May, L.; Guha, A.; Rak, J.; Peinado, H.; Alečković, M.; Lavotshkin, S.; Matei, I.; Costa-Silva, B.; Moreno-Bueno, G.; Hergueta-Redondo, M.; Williams, C.; García-Santos, G.; Ghajar, C.; Nitadori-Hoshino, A.; Hoffman, C.; Badal, K.; Garcia, B. a.; Callahan, M. K.; Yuan, J.; Martins, V. R.; Skog, J.; Kaplan, R. N.; Brady, M. S.; Wolchok, J. D.; Chapman, P. B.; Kang, Y.; Bromberg, J.; Lyden, D.; Peinado, H.; Lavotshkin, S.; Lyden, D.; Luketic, L.; Delanghe, J.; Sobol, P. T.; Yang, P.; Frotten, E.; Mossman, K. L.; Gauldie, J.; Bramson, J. L.; Wan, Y.; Balaj, L.; Lessard, R.; Dai, L.; Cho, Y.-J.; Pomeroy, S. L.; Breakefield, X. O.; Skog, J.; Boelens, M. C.; Wu, T. J.; Nabet, B. Y.; Xu, B.; Qiu, Y.; Yoon, T.; Azzam, D. J.; Victor, C. T.-S.; Wiemann, B. Z.; Ishwaran, H.; Brugge, P. J. ter; Jonkers, J.; Slingerland, J.; Minn, A. J.; Bronisz, A.; Wang, Y.; Nowicki, M. O.; Peruzzi, P.; Ansari, K. I.; Ogawa, D.; Balaj, L.; Rienzo, G. D.; Mineo, M.; Nakano, I.; Ostrowski, M. C.; Hochberg, F.; Weissleder, R.; Lawler, S. E.; Chiocca, E. A.; Godlewski, J.; Clayton, A.; Mitchell, J. P.; Court, J.; Mason, M. D.; Tabi, Z.; Linnane, S.; Iero, M.; Valenti, R.; Huber, V.; Filipazzi, P.; Parmiani, G.; Fais, S.; Rivoltini, L.; Webber, J. P.; Spary, L. K.; Sanders, A. J.; Chowdhury, R.; Jiang, W. G.; Steadman, R.; Wymant, J.; Jones, A. T.; Kynaston, H.; Mason, M. D.; Tabi, Z.; Clayton, A.; Webber, J. P.; Steadman, R.; Mason, M. D.; Tabi, Z.; Clayton, A.;

Kulkarni, Y. M.; II, D. J. K.; Wu, Y.; Byrne-Hoffman, C.; Ratajczak, J.; Wysoczynski, M.; Hayek, F.; Janowska-Wieczorek, A.; Ratajczak, M. Z.; Somasundaram, R.; Herlyn, M.; Hood, J. L.; San, R. S.; Wickline, S. A.; Andre, F.; Schartz, N. E. C.; Movassagh, M.; Flament, C.; Pautier, P.; Morice, P.; Pomel, C.; Lhomme, C.; Escudier, B.; Chevalier, T. L.; Tursz, T.; Amigorena, S.; Raposo, G.; Angevin, E.; Zitvogel, L.; Hood, J. L.; Pan, H.; Lanza, G. M.; Wickline, S. A.; Taylor, D. D.; Gerçel-Taylor, C.; Dai, S.; Wan, T.; Wang, B.; Zhou, X.; Xiu, F.; Chen, T.; Wu, Y.; Cao, X.; Wolfers, J.; Lozier, A.; Raposo, G.; Regnault, A.; Théry, C.; Masurier, C.; Flament, C.; Pouzieux, S.; Faure, F.; Tursz, T.; Angevin, E.; Amigorena, S.; Zitvogel, L.; Nilsson, J.; Skog, J.; Nordstrand, A.; Baranov, V.; Mincheva-Nilsson, L.; Breakefield, X. O.; Widmark, A.; Mitchell, P. J.; Welton, J.; Staffurth, J.; Court, J.; Mason, M. D.; Tabi, Z.; Clayton, A.; Villarroya-Beltri, C.; Baixauli, F.; Gutiérrez-Vázquez, C.; Sánchez-Madrid, F.; Mittelbrunn, M.; Filipazzi, P.; Bürdek, M.; Villa, A.; Rivoltini, L.; Huber, V.; Keller, S.; Ridinger, J.; Rupp, A.-K.; Janssen, J. W. G.; Altevogt, P.; Clayton, A.; Mason, M. D.; Gross, J. C.; Chaudhary, V.; Bartscherer, K.; Boutros, M.; Xu, D.; Tahara, H.; Sharma, P.; Schiapparelli, L.; Cline, H. T.; Okoye, I. S.; Coomes, S. M.; Pelly, V. S.; Czieso, S.; Papayannopoulos, V.; Tolmachova, T.; Seabra, M. C.; Wilson, M. S.; Fleming, A. B.; Saltzman, W. M.; Cocucci, E.; Racchetti, G.; Meldolesi, J.; Raposo, G.; Stoorvogel, W.; Mathivanan, S.; Ji, H.; Simpson, R. J.; Kulkarni, Y. M.; Chambers, E.; McGray, A. J. R.; Ware, J. S.; Bramson, J. L.; II, D. J. K.; Kulkarni, Y. M.; II, D. J. K.; Théry, C.; Amigorena, S.; Raposo, G.; Clayton, A.; Hu, W.; Zhang, C.; Fang, Y.; Lou, C.; II, D. J. K.; Brundage, K. M.; Pol, E. van der; Hoekstra, a. G.; Sturk, A.; Otto, C.; Leeuwen, T. G. van; Nieuwland, R.; Sokolova, V.; Ludwig, A.-K.; Hornung, S.; Rotan, O.; Horn, P. A.; Epple, M.; Giebel, B.; Sharma, S.; Rasool, H. I.; Palanisamy, V.; Mathisen, C.; Schmidt, M.; Wong, D. T.; Gimzewski, J. K.; György, B.; Szabó, T. G.; Pásztói, M.; Pál, Z.; Misják, P.; Aradi, B.; László, V.; Pállinger, E.; Pap, E.; Kittel, A.; Nagy, G.; Falus, A.; Buzás, E. I.; Tang, L.; Fan, T. M.; Borst, L. B.; Cheng, J.; Reddy, S. T.; Vlies, A. J. van der; Simeoni, E.; O'Neil, C. P.; Swartz, M. A.; Hubbell, J. A.; Irvine, D. J.; Swartz, M. A.; Szeto, G. L.; Pol, E. van der; Gemert, M. J. van; Sturk, A.; Nieuwland, R.; Leeuwen, T. G. van; Maas, S. L. N.; Vrij, J. de; Vlist, E. J. van der; Geragousian, B.; Bloois, L. van; Mastrobattista, E.; Schiffelers, R. M.; Wauben, M. H. M.; Broekman, M. L. D.; Hoen, E. N. N.-'t M. N.-'t; Erlandsen, S. L.; Bemrick, W. J.; Schupp, D. E.; Shields, J. M.; Jarroll, E. L.; Sauch, J. F.; Pawley, J. B.; Speirs, V.; Eich-Bender, S.; Youngson, C. R.; Cutz, E.; Hoen, E. N. N.-'t M. N.-'t; Vlist, E. J. van der; Aalberts, M.; Mertens, H. C.; Bosch, B. J.; Bartelink, W.; Mastrobattista, E.; Gaal, E. V. B. van; Stoorvogel, W.; Arkesteijn, G. J.; Wauben, M. H. M.; Vlist, E. J. van der; Hoen, E. N. N.-'t M. N.-'t; Stoorvogel, W.; Arkesteijn, G. J.; Wauben, M. H. M.; Higginbotham, J. N.; Beckler, M. D.; Gephart, J. D.; Franklin, J. L.; Bogatcheva, G.; Kremers, G. J.; Piston, D. W.; Ayers, G. D.; McConnell, R. E.; Tyska, M. J.; Coffey, R. J.; Batagov, A. O.; Kurochkin, I. V.; Ekstrom, K.; Valadi, H.; Sjostrand, M.;

Malmhall, C.; Bossios, A.; Eldh, M.; Lotvall, J.; Pegtel, D. M.; Cosmopoulos, K.; Thorley-Lawson, D. A.; Eijndhoven, M. A. van; Hopmans, E. S.; Lindenberg, J. L.; Gruijl, T. D. de; Würdinger, T.; Middeldorp, J. M.; Klinke, D. J. Exosomes: Improved Methods to Characterize Their Morphology, RNA Content, and Surface Protein Biomarkers. *The Analyst* **2015**, *140* (19), 6631–6642. https://doi.org/10.1039/c5an00688k.

(109) Campos-Silva, C.; Suárez, H.; Jara-Acevedo, R.; Linares-Espinós, E.; Martinez-Piñeiro, L.; Yáñez-Mó, M.; Valés-Gómez, M. High Sensitivity Detection of Extracellular Vesicles Immune-Captured from Urine by Conventional Flow Cytometry. *Sci. Rep.* **2019**, *9* (1), 2042. https://doi.org/10.1038/s41598-019-38516-8.

(110) Khushman, M.; Bhardwaj, A.; Patel, G. K.; Laurini, J. A.; Roveda, K.; Tan, M. C.; Patton, M. C.; Singh, S.; Taylor, W.; Singh, A. P. Exosomal Markers (CD63 and CD9) Expression Pattern Using Immunohistochemistry in Resected Malignant and Non-Malignant Pancreatic Specimens. *Pancreas* **2017**, *46* (6), 782–788. https://doi.org/10.1097/MPA.0000000000000847.

(111) Wong, C.-H.; Chen, Y.-C. Clinical Significance of Exosomes as Potential Biomarkers in Cancer. *World J. Clin. Cases* **2019**, *7* (2), 171–190. https://doi.org/10.12998/wjcc.v7.i2.171.

(112) Yang, E.; Wang, X.; Gong, Z.; Yu, M.; Wu, H.; Zhang, D. Exosome-Mediated Metabolic Reprogramming: The Emerging Role in Tumor Microenvironment Remodeling and Its Influence on Cancer Progression. *Signal Transduct. Target. Ther.* **2020**, *5* (1), 1–13. https://doi.org/10.1038/s41392-020-00359-5.

(113) Bebelman, M. P.; Smit, M. J.; Pegtel, D. M.; Baglio, S. R. Biogenesis and Function of Extracellular Vesicles in Cancer. *Pharmacol. Ther.* **2018**, *188*, 1–11. https://doi.org/10.1016/j.pharmthera.2018.02.013.

(114) Brinton, L. T.; Sloane, H. S.; Kester, M.; Kelly, K. A. Formation and Role of Exosomes in Cancer. *Cell. Mol. Life Sci.* **2015**, *72* (4), 659–671. https://doi.org/10.1007/s00018-014-1764-3.

(115) D'Souza-Schorey, C.; Clancy, J. W. Tumor-Derived Microvesicles: Shedding Light on Novel Microenvironment Modulators and Prospective Cancer Biomarkers. *Genes Dev.* **2012**, *26* (12), 1287–1299. https://doi.org/10.1101/gad.192351.112.

(116) Doyle, L. M.; Wang, M. Z. Overview of Extracellular Vesicles, Their Origin, Composition, Purpose, and Methods for Exosome Isolation and Analysis. *Cells* **2019**, *8* (7), 727. https://doi.org/10.3390/cells8070727.

(117) Bebelman, M. P.; Janssen, E.; Pegtel, D. M.; Crudden, C. The Forces Driving Cancer Extracellular Vesicle Secretion. *Neoplasia N. Y. N* **2020**, *23* (1), 149–157. https://doi.org/10.1016/j.neo.2020.11.011.

(118) Raposo, G.; Stoorvogel, W. Extracellular Vesicles: Exosomes, Microvesicles, and Friends. *J. Cell Biol.* **2013**, *200* (4).

(119) Menck, K.; Sivaloganathan, S.; Bleckmann, A.; Binder, C. Microvesicles in Cancer: Small Size, Large Potential. *Int. J. Mol. Sci.* **2020**, *21* (15), 5373. https://doi.org/10.3390/ijms21155373.

(120) Bian, X.; Xiao, Y.-T.; Wu, T.; Yao, M.; Du, L.; Ren, S.; Wang, J. Microvesicles and Chemokines in Tumor Microenvironment: Mediators of Intercellular Communications in Tumor Progression. *Mol. Cancer* **2019**, *18* (1), 50. https://doi.org/10.1186/s12943-019-0973-7.

(121) Minciacchi, V. R.; Freeman, M. R.; Di Vizio, D. Extracellular Vesicles in Cancer: Exosomes, Microvesicles and the Emerging Role of Large Oncosomes. *Semin. Cell Dev. Biol.* **2015**, *40*, 41–51. https://doi.org/10.1016/j.semcdb.2015.02.010.

(122) Gebara, N.; Rossi, A.; Skovronova, R.; Aziz, J. M.; Asthana, A.; Bussolati, B. Extracellular Vesicles, Apoptotic Bodies and Mitochondria: Stem Cell Bioproducts for Organ Regeneration. *Curr. Transplant. Rep.* **2020**, *7* (2), 105–113. https://doi.org/10.1007/s40472-020-00282-2.

(123) Vasudevan, D.; Gaddam, R. R.; Trinchi, A.; Cole, I. Core–Shell Quantum Dots: Properties and Applications. *J. Alloys Compd.* **2015**, *636*, 395–404. https://doi.org/10.1016/j.jallcom.2015.02.102.

(124) Medintz, I. L.; Uyeda, H. T.; Goldman, E. R.; Mattoussi, H. Quantum Dot Bioconjugates for Imaging, Labelling and Sensing. *Nat. Mater.* **2005**, *4* (6), 435–446. https://doi.org/10.1038/nmat1390.

(125) Bilan, R.; Fleury, F.; Nabiev, I.; Sukhanova, A. Quantum Dot Surface Chemistry and Functionalization for Cell Targeting and Imaging. *Bioconjug. Chem.* **2015**, *26* (4), 609–624. https://doi.org/10.1021/acs.bioconjchem.5b00069.

(126) Goldman, E. R.; Anderson, G. P.; Tran, P. T.; Mattoussi, H.; Charles, P. T.; Mauro, J. M. Conjugation of Luminescent Quantum Dots with Antibodies Using an Engineered Adaptor Protein To Provide New Reagents for Fluoroimmunoassays. *Anal. Chem.* **2002**, *74* (4), 841–847. https://doi.org/10.1021/ac010662m.

(127) Laborda, F.; Jiménez-Lamana, J.; Bolea, E.; R. Castillo, J. Critical Considerations for the Determination of Nanoparticle Number Concentrations, Size and Number

Size Distributions by Single Particle ICP-MS. *J. Anal. At. Spectrom.* **2013**, *28* (8), 1220–1232. https://doi.org/10.1039/C3JA50100K.

(128) Schmidt, B.; Loeschner, K.; Hadrup, N.; Mortensen, A.; Sloth, J. J.; Koch, C. B.; Larsen, E. H. Quantitative Characterization of Gold Nanoparticles by Field-Flow Fractionation Coupled Online with Light Scattering Detection and Inductively Coupled Plasma Mass Spectrometry. *Anal. Chem.* **2011**, *83* (7), 2461–2468. https://doi.org/10.1021/ac102545e.

(129) Hetzer, B.; Burcza, A.; Gräf, V.; Walz, E.; Greiner, R. Online-Coupling of AF4 and Single Particle-ICP-MS as an Analytical Approach for the Selective Detection of Nanosilver Release from Model Food Packaging Films into Food Simulants. *Food Control* **2017**, *80*, 113–124. https://doi.org/10.1016/j.foodcont.2017.04.040.

(130) Ciravolo, V.; Huber, V.; Ghedini, G. C.; Venturelli, E.; Bianchi, F.; Campiglio, M.; Morelli, D.; Villa, A.; Della Mina, P.; Menard, S.; Filipazzi, P.; Rivoltini, L.; Tagliabue, E.; Pupa, S. M. Potential Role of HER2-Overexpressing Exosomes in Countering Trastuzumab-Based Therapy. *J. Cell. Physiol.* **2012**, *227* (2), 658–667. https://doi.org/10.1002/jcp.22773.

(131) Barok, M.; Puhka, M.; Vereb, G.; Szollosi, J.; Isola, J.; Joensuu, H. Cancer-Derived Exosomes from HER2-Positive Cancer Cells Carry Trastuzumab-Emtansine into Cancer Cells Leading to Growth Inhibition and Caspase Activation. *BMC Cancer* **2018**, *18*, 504. https://doi.org/10.1186/s12885-018-4418-2.

(132) Wang, L.; Zhou, X.; Zou, W.; Wu, Y.; Zhao, J.; Chen, X.; Zhou, G. G. Exosomes Containing MiRNAs Targeting HER2 Synthesis and Engineered to Adhere to HER2 on Tumor Cells Surface Exhibit Enhanced Antitumor Activity. *J. Nanobiotechnology* **2020**, *18* (1), 153. https://doi.org/10.1186/s12951-020-00711-5.

(133) Fang, S.; Tian, H.; Li, X.; Jin, D.; Li, X.; Kong, J.; Yang, C.; Yang, X.; Lu, Y.; Luo, Y.; Lin, B.; Niu, W.; Liu, T. Clinical Application of a Microfluidic Chip for Immunocapture and Quantification of Circulating Exosomes to Assist Breast Cancer Diagnosis and Molecular Classification. *PLOS ONE* **2017**, *12* (4), e0175050. https://doi.org/10.1371/journal.pone.0175050.

(134) Han, M.; Hu, J.; Lu, P.; Cao, H.; Yu, C.; Li, X.; Qian, X.; Yang, X.; Yang, Y.; Han, N.; Dou, D.; Zhang, F.; Ye, M.; Yang, C.; Gu, Y.; Dong, H. Exosome-Transmitted MiR-567 Reverses Trastuzumab Resistance by Inhibiting ATG5 in Breast Cancer. *Cell Death Dis.* **2020**, *11* (1), 1–15. https://doi.org/10.1038/s41419-020-2250-5.

(135) Jakobsen, N. A.; Hamdy, F. C.; Bryant, R. J. Novel Biomarkers for the Detection of Prostate Cancer. *J. Clin. Urol.* **2016**, *9* (2 Suppl), 3–10. https://doi.org/10.1177/2051415816656121.

(136) Hell, S. W.; Kroug, M. Ground-State-Depletion Fluorscence Microscopy: A Concept for Breaking the Diffraction Resolution Limit. *Appl. Phys. B* **1995**, *60* (5), 495–497. https://doi.org/10.1007/BF01081333.

(137) Heintzmann, R.; Ficz, G. Breaking the Resolution Limit in Light Microscopy. *Brief. Funct. Genomics* **2006**, *5* (4), 289–301. https://doi.org/10.1093/bfgp/ell036.

(138) Wollman, A. J. M.; Nudd, R.; Hedlund, E. G.; Leake, M. C. From Animaculum to Single Molecules: 300 Years of the Light Microscope. *Open Biol. 5* (4), 150019. https://doi.org/10.1098/rsob.150019.

(139) Harada, K.; Akashi, T.; Niitsu, K.; Shimada, K.; Ono, Y. A.; Shindo, D.; Shinada, H.; Mori, S. Interference Experiment with Asymmetric Double Slit by Using 1.2-MV Field Emission Transmission Electron Microscope. *Sci. Rep.* **2018**, *8* (1), 1008. https://doi.org/10.1038/s41598-018-19380-4.

(140) Smith, D. J. Ultimate Resolution in the Electron Microscope? *Mater. Today* **2008**, *11*, 30–38. https://doi.org/10.1016/S1369-7021(09)70005-7.

(141) Benhiba, F.; Benzekri, Z.; Guenbour, A.; Tabyaoui, M.; Bellaouchou, A.; Boukhris, S.; Oudda, H.; Warad, I.; Zarrouk, A. Combined Electronic/Atomic Level Computational, Surface (SEM/EDS), Chemical and Electrochemical Studies of the Mild Steel Surface by Quinoxalines Derivatives Anti-Corrosion Properties in 1 mol·L-1 HCl Solution. *Chin. J. Chem. Eng.* **2020**, *28* (5), 1436–1458. https://doi.org/10.1016/j.cjche.2020.03.002.

(142) Moro, D.; Ulian, G.; Valdrè, G. SEM-EDS Nanoanalysis of Mineral Composite Materials: A Monte Carlo Approach. *Compos. Struct.* **2021**, *259*, 113227. https://doi.org/10.1016/j.compstruct.2020.113227.

(143) Synthesis of silver nanoparticles with different shapes - ScienceDirect https://www.sciencedirect.com/science/article/pii/S1878535214003645 (accessed 2021 -08 -02).

(144) Berger Bioucas, F. E.; Damm, C.; Peukert, W.; Rausch, M. H.; Koller, T. M.; Giraudet, C.; Fröba, A. P. Translational and Rotational Diffusion Coefficients of Gold Nanorods Dispersed in Mixtures of Water and Glycerol by Polarized Dynamic Light Scattering. *J. Phys. Chem. B* **2019**, *123* (44), 9491–9502. https://doi.org/10.1021/acs.jpcb.9b08274.

(145) Stetefeld, J.; McKenna, S. A.; Patel, T. R. Dynamic Light Scattering: A Practical Guide and Applications in Biomedical Sciences. *Biophys. Rev.* **2016**, *8* (4), 409–427. https://doi.org/10.1007/s12551-016-0218-6.

(146) Hoo, C. M.; Starostin, N.; West, P.; Mecartney, M. L. A Comparison of Atomic Force Microscopy (AFM) and Dynamic Light Scattering (DLS) Methods to Characterize Nanoparticle Size Distributions. *J. Nanoparticle Res.* **2008**, *10* (SUPPL. 1), 89–96. https://doi.org/10.1007/s11051-008-9435-7.

(147) Sitar, S.; Vezocňik, V.; Maceˇk, P.; Kogej, K.; Pahovnik, D.; Žagar, E. Pitfalls in Size Characterization of Soft Particles by Dynamic Light Scattering Online Coupled to Asymmetrical Flow Field-Flow Fractionation. *Anal. Chem.* **2017**, *89* (21). https://doi.org/10.1021/acs.analchem.7b03251.

(148) Varenne, F.; Makky, A.; Gaucher-Delmas, M.; Violleau, F.; Vauthier, C. Multimodal Dispersion of Nanoparticles: A Comprehensive Evaluation of Size Distribution with 9 Size Measurement Methods. *Pharm. Res.* **2016**, *33* (5), 1220–1234. https://doi.org/10.1007/s11095-016-1867-7.

(149) Thomas, S.; Thomas, R.; Zachariah, A. K.; Kumar, R. *Thermal and Rheological Measurement Techniques for Nanomaterials Characterization*; Elsevier, 2017.

(150) Li, Z. Critical Particle Size Where the Stokes-Einstein Relation Breaks Down. https://doi.org/10.1103/PhysRevE.80.061204.

(151) Miller, C. C.; Walker, J. The Stokes-Einstein Law for Diffusion in Solution. *Proc. R. Soc. Lond. Ser. Contain. Pap. Math. Phys. Character* **1924**, *106* (740), 724–749. https://doi.org/10.1098/rspa.1924.0100.

(152) Ansar, S. M.; Mudalige, T. Characterization of Doxorubicin Liposomal Formulations for Size-Based Distribution of Drug and Excipients Using Asymmetric-Flow Field-Flow Fractionation (AF4) and Liquid Chromatography-Mass Spectrometry (LC-MS). *Int. J. Pharm.* **2020**, *574*, 118906. https://doi.org/10.1016/j.ijpharm.2019.118906.

(153) Maguire, C. M.; Rösslein, M.; Wick, P.; Prina-Mello, A. Characterisation of Particles in Solution–a Perspective on Light Scattering and Comparative Technologies. *Sci. Technol. Adv. Mater.* **2018**, *19* (1), 732–745. https://doi.org/10.1080/14686996.2018.1517587.

(154) Filipe, V.; Hawe, A.; Jiskoot, W. Critical Evaluation of Nanoparticle Tracking Analysis (NTA) by NanoSight for the Measurement of Nanoparticles and Protein Aggregates. *Pharm. Res.* **2010**, *27* (5), 796–810. https://doi.org/10.1007/s11095-010-0073-2.

(155) Nanoparticle tracking analysis for the multiparameter characterization and counting of nanoparticle suspensions - PubMed https://pubmed.ncbi.nlm.nih.gov/22791460/ (accessed 2021 -07 -14).

(156) Gollwitzer, C.; Bartczak, D.; Goenaga-Infante, H.; Kestens, V.; Krumrey, M.; Minelli, C.; Pálmai, M.; Ramaye, Y.; Roebben, G.; Sikora, A.; Varga, Z. A Comparison of Techniques for Size Measurement of Nanoparticles in Cell Culture Medium. *Anal. Methods* **2016**, *8* (26), 5272–5282. https://doi.org/10.1039/c6ay00419a.

(157) Gruia, F.; Parupudi, A.; Polozova, A. Practical Considerations for Detection and Characterization of Sub-Micron Particles in Protein Solutions by Nanoparticle Tracking Analysis. *PDA J. Pharm. Sci. Technol.* **2015**, *69* (3), 427–439. https://doi.org/10.5731/pdajpst.2015.01051.

(158) Carr, B.; Malloy, A. NanoParticle Tracking Analysis – The NANOSIGHT System. 8.

(159) Ernst, D.; Köhler, J. Measuring a Diffusion Coefficient by Single-Particle Tracking: Statistical Analysis of Experimental Mean Squared Displacement Curves. *Phys. Chem. Chem. Phys.* **2012**, *15* (3), 845–849. https://doi.org/10.1039/C2CP43433D.

(160) Zhou, C.; Krueger, A. B.; Barnard, J. G.; Qi, W.; Carpenter, J. F. Characterization of Nanoparticle Tracking Analysis for Quantification and Sizing of Submicron Particles of Therapeutic Proteins. *J. Pharm. Sci.* **2015**, *104* (8), 2441–2450. https://doi.org/10.1002/jps.24510.

(161) Akbulut, O.; Mace, C. R.; Martinez, R. V.; Kumar, A. A.; Nie, Z.; Patton, M. R.; Whitesides, G. M. Separation of Nanoparticles in Aqueous Multiphase Systems through Centrifugation. *Nano Lett.* **2012**, *12* (8), 4060–4064. https://doi.org/10.1021/nl301452x.

(162) Silvio, D. D.; Rigby, N.; Bajka, B.; Mayes, A.; Mackie, A.; Bombelli, F. B. Technical Tip: High-Resolution Isolation of Nanoparticle–Protein Corona Complexes from Physiological Fluids. *Nanoscale* **2015**, *7* (28), 11980–11990. https://doi.org/10.1039/C5NR02618K.

(163) Chen, G.; Wang, Y.; Tan, L. H.; Yang, M.; Tan, L. S.; Chen, Y.; Chen, H. High-Purity Separation of Gold Nanoparticle Dimers and Trimers. *J. Am. Chem. Soc.* **2009**, *131* (12), 4218–4219. https://doi.org/10.1021/ja900809z.

(164) Novak, J. P.; Nickerson, C.; Franzen, S.; Feldheim, D. L. Purification of Molecularly Bridged Metal Nanoparticle Arrays by Centrifugation and Size

Exclusion Chromatography. *Anal. Chem.* **2001**, *73* (23), 5758–5761. https://doi.org/10.1021/ac010812t.

(165) Langevin, S. M.; Kuhnell, D.; Orr-Asman, M. A.; Biesiada, J.; Zhang, X.; Medvedovic, M.; Thomas, H. E. Balancing Yield, Purity and Practicality: A Modified Differential Ultracentrifugation Protocol for Efficient Isolation of Small Extracellular Vesicles from Human Serum. *RNA Biol.* **2019**, *16* (1), 5–12. https://doi.org/10.1080/15476286.2018.1564465.

(166) Li, K.; Wong, D. K.; Hong, K. Y.; Raffai, R. L. Cushioned–Density Gradient Ultracentrifugation (C–DGUC): A Refined and High Performance Method for the Isolation, Characterization & Use of Exosomes. *Methods Mol. Biol. Clifton NJ* **2018**, *1740*, 69–83. https://doi.org/10.1007/978-1-4939-7652-2_7.

(167) Momen-Heravi, F. Isolation of Extracellular Vesicles by Ultracentrifugation. In *Extracellular Vesicles: Methods and Protocols*; Kuo, W. P., Jia, S., Eds.; Methods in Molecular Biology; Springer: New York, NY, 2017; pp 25–32. https://doi.org/10.1007/978-1-4939-7253-1_3.

(168) Dobson, R. C. J.; Patel, T. R. Analytical Ultracentrifugation: Still the Gold Standard That Offers Multiple Solutions. *Eur. Biophys. J.* **2020**, *49* (8), 673–676. https://doi.org/10.1007/s00249-020-01483-4.

(169) Gupta, S.; Rawat, S.; Arora, V.; Kottarath, S. K.; Dinda, A. K.; Vaishnav, P. K.; Nayak, B.; Mohanty, S. An Improvised One-Step Sucrose Cushion Ultracentrifugation Method for Exosome Isolation from Culture Supernatants of Mesenchymal Stem Cells. *Stem Cell Res. Ther.* **2018**, *9* (1), 180. https://doi.org/10.1186/s13287-018-0923-0.

(170) Cvjetkovic, A.; Lötvall, J.; Lässer, C. The Influence of Rotor Type and Centrifugation Time on the Yield and Purity of Extracellular Vesicles. *J. Extracell. Vesicles* **2014**, *3* (1), 23111. https://doi.org/10.3402/jev.v3.23111.

(171) Lötvall, J.; Hill, A. F.; Hochberg, F.; Buzás, E. I.; Di Vizio, D.; Gardiner, C.; Gho, Y. S.; Kurochkin, I. V.; Mathivanan, S.; Quesenberry, P.; Sahoo, S.; Tahara, H.; Wauben, M. H.; Witwer, K. W.; Théry, C. Minimal Experimental Requirements for Definition of Extracellular Vesicles and Their Functions: A Position Statement from the International Society for Extracellular Vesicles. *J. Extracell. Vesicles* **2014**, *3*, 26913. https://doi.org/10.3402/JEV.V3.26913.

(172) Bai, L.; Ma, X.; Liu, J.; Sun, X.; Zhao, D.; Evans, D. G. Rapid Separation and Purification of Nanoparticles in Organic Density Gradients. *J. Am. Chem. Soc.* **2010**, *132* (7), 2333–2337. https://doi.org/10.1021/ja908971d.

(173) Tauro, B. J.; Greening, D. W.; Mathias, R. A.; Ji, H.; Mathivanan, S.; Scott, A. M.; Simpson, R. J. Comparison of Ultracentrifugation, Density Gradient Separation, and Immunoaffinity Capture Methods for Isolating Human Colon Cancer Cell Line LIM1863-Derived Exosomes. *Methods* **2012**, *56* (2), 293–304. https://doi.org/10.1016/j.ymeth.2012.01.002.

(174) Xiong, B.; Cheng, J.; Qiao, Y.; Zhou, R.; He, Y.; Yeung, E. S. Separation of Nanorods by Density Gradient Centrifugation. *J. Chromatogr. A* **2011**, *1218* (25), 3823–3829. https://doi.org/10.1016/J.CHROMA.2011.04.038.

(175) Weng, Y.; Sui, Z.; Shan, Y.; Hu, Y.; Chen, Y.; Zhang, L.; Zhang, Y. Effective Isolation of Exosomes with Polyethylene Glycol from Cell Culture Supernatant for In-Depth Proteome Profiling. *The Analyst* **2016**, *141* (15), 4640–4646. https://doi.org/10.1039/c6an00892e.

(176) Patel, G. K.; Khan, M. A.; Zubair, H.; Srivastava, S. K.; Khushman, M.; Singh, S.; Singh, A. P. Comparative Analysis of Exosome Isolation Methods Using Culture Supernatant for Optimum Yield, Purity and Downstream Applications. *Sci. Rep.* **2019**, *9* (1). https://doi.org/10.1038/s41598-019-41800-2.

(177) Zlotogorski-Hurvitz, A.; Dayan, D.; Chaushu, G.; Korvala, J.; Salo, T.; Sormunen, R.; Vered, M. Human Saliva-Derived Exosomes: Comparing Methods of Isolation. *J. Histochem. Cytochem.* **2015**, *63* (3), 181–189. https://doi.org/10.1369/0022155414564219.

(178) Yamauchi, M.; Shimizu, K.; Rahman, M.; Ishikawa, H.; Takase, H.; Ugawa, S.; Okada, A.; Inoshima, Y. Efficient Method for Isolation of Exosomes from Raw Bovine Milk. *Drug Dev. Ind. Pharm.* **2018**, 1–6. https://doi.org/10.1080/03639045.2018.1539743.

(179) Van Deun, J.; Mestdagh, P.; Sormunen, R.; Cocquyt, V.; Vermaelen, K.; Vandesompele, J.; Bracke, M.; De Wever, O.; Hendrix, A. The Impact of Disparate Isolation Methods for Extracellular Vesicles on Downstream RNA Profiling. *J. Extracell. Vesicles* **2014**, *3*. https://doi.org/10.3402/jev.v3.24858.

(180) Lobb, R. J.; Becker, M.; Wen, S.; Wong, C. S. F.; Wiegmans, A. P.; Leimgruber, A.; Möller, A. Optimized Exosome Isolation Protocol for Cell Culture Supernatant and Human Plasma. *J. Extracell. Vesicles* **2015**, *4* (1), 27031. https://doi.org/10.3402/jev.v4.27031.

(181) Lobb, R. J.; Becker, M.; Wen, S.; Wong, C. S. F.; Wiegmans, A. P.; Leimgruber, A.; Möller, A. Optimized Exosome Isolation Protocol for Cell Culture Supernatant and Human Plasma. J Extracell Vesicles 2015, 4, 10.3402/jev.v4.27031. https://doi.org/10.3402/jev.v4.27031.

(182) Pavani, K. C.; Hendrix, A.; Van Den Broeck, W.; Couck, L.; Szymanska, K.; Lin, X.; De Koster, J.; Van Soom, A.; Leemans, B. Isolation and Characterization of Functionally Active Extracellular Vesicles from Culture Medium Conditioned by Bovine Embryos In Vitro. *Int. J. Mol. Sci.* **2019**, *20* (1), 38. https://doi.org/10.3390/ijms20010038.

(183) Nath Neerukonda, S.; Egan, N. A.; Patria, J.; Assakhi, I.; Tavlarides-Hontz, P.; Modla, S.; Muñoz, E. R.; Hudson, M. B.; Parcells, M. S. Comparison of Exosomes Purified via Ultracentrifugation (UC) and Total Exosome Isolation (TEI) Reagent from the Serum of Marek's Disease Virus (MDV)-Vaccinated and Tumor-Bearing Chickens. *J. Virol. Methods* **2019**, *263*, 1–9. https://doi.org/10.1016/j.jviromet.2018.10.004.

(184) Kurnik, R. T.; Yu, A. W.; Blank, G. S.; Burton, A. R.; Smith, D.; Athalye, A. M.; Reis, R. van. Buffer Exchange Using Size Exclusion Chromatography, Countercurrent Dialysis, and Tangential Flow Filtration: Models, Development, and Industrial Application. *Biotechnol. Bioeng.* **1995**, *45* (2), 149–157. https://doi.org/10.1002/bit.260450209.

(185) Brocken, L.; D. Price, P.; Whittaker, J.; R. Baxendale, I. Purification of Poly(Acrylic Acid) Using a Membrane Ultra-Filtration Unit in Flow. *React. Chem. Eng.* **2017**, *2* (5), 656–661. https://doi.org/10.1039/C7RE00080D.

(186) Fernandez-Cerezo, L.; Rayat, A. C. M. E.; Chatel, A.; Pollard, J. M.; Lye, G. J.; Hoare, M. An Ultra Scale-down Method to Investigate Monoclonal Antibody Processing during Tangential Flow Filtration Using Ultrafiltration Membranes. *Biotechnol. Bioeng.* **2019**, *116* (3), 581–590. https://doi.org/10.1002/bit.26859.

(187) Ghosh, R.; Cui, Z. F. Purification of Lysozyme Using Ultrafiltration. *Biotechnol. Bioeng.* **2000**, *68* (2), 191–203. https://doi.org/10.1002/(SICI)1097-0290(20000420)68:2<191::AID-BIT8>3.0.CO;2-A.

(188) Dalwadi, G.; Benson, H. A. E.; Chen, Y. Comparison of Diafiltration and Tangential Flow Filtration for Purification of Nanoparticle Suspensions. *Pharm. Res.* **2005**, *22* (12), 2152–2162. https://doi.org/10.1007/s11095-005-7781-z.

(189) Cunningham, R.; Wang, J.; Wellner, D.; Li, L. Investigation and Reduction of Sub-Microgram Peptide Loss Using Molecular Weight Cut-off Fractionation Prior to Mass Spectrometric Analysis. *J. Mass Spectrom. JMS* **2012**, *47* (10), 1327–1332. https://doi.org/10.1002/jms.3069.

(190) Heinemann, M. L.; Ilmer, M.; Silva, L. P.; Hawke, D. H.; Recio, A.; Vorontsova, M. A.; Alt, E.; Vykoukal, J. Benchtop Isolation and Characterization of Functional Exosomes by Sequential Filtration. *J. Chromatogr. A* **2014**, *1371*, 125–135. https://doi.org/10.1016/j.chroma.2014.10.026.

(191) Wilding, A.; Liu, R.; Zhou, J. L. Validation of Cross-Flow Ultrafiltration for Sampling of Colloidal Particles from Aquatic Systems. *J. Colloid Interface Sci.* **2004**, *280* (1), 102–112. https://doi.org/10.1016/j.jcis.2004.07.002.

(192) Powell, M. J.; Timperman, A. T. Quantitative Analysis of Protein Recovery from Dilute, Large Volume Samples by Tangential Flow Ultrafiltration. *J. Membr. Sci.* **2005**, *252* (1), 227–236. https://doi.org/10.1016/j.memsci.2004.12.024.

(193) Füglistaller, P. Comparison of Immunoglobulin Binding Capacities and Ligand Leakage Using Eight Different Protein A Affinity Chromatography Matrices. *J. Immunol. Methods* **1989**, *124* (2), 171–177. https://doi.org/10.1016/0022-1759(89)90350-5.

(194) Zhang, C.; Rodriguez, E.; Bi, C.; Zheng, X.; Suresh, D.; Suh, K.; Li, Z.; Elsebaei, F.; Hage, D. S. High Performance Affinity Chromatography and Related Separation Methods for the Analysis of Biological and Pharmaceutical Agents. *The Analyst* **2018**, *143* (2), 374–391. https://doi.org/10.1039/c7an01469d.

(195) Zarovni, N.; Corrado, A.; Guazzi, P.; Zocco, D.; Lari, E.; Radano, G.; Muhhina, J.; Fondelli, C.; Gavrilova, J.; Chiesi, A. Integrated Isolation and Quantitative Analysis of Exosome Shuttled Proteins and Nucleic Acids Using Immunocapture Approaches. *Methods* **2015**, *87*, 46–58. https://doi.org/10.1016/j.ymeth.2015.05.028.

(196) Yang, L.; P. Banada, P.; R. Chatni, M.; Lim, K. S.; K. Bhunia, A.; Ladisch, M.; Bashir, R. A Multifunctional Micro-Fluidic System for Dielectrophoretic Concentration Coupled with Immuno-Capture of Low Numbers of Listeria Monocytogenes. *Lab. Chip* **2006**, *6* (7), 896–905. https://doi.org/10.1039/B607061M.

(197) Beekman, P.; Enciso-Martinez, A.; Suk Rho, H.; Pundlik Pujari, S.; Lenferink, A.; Zuilhof, H.; M. Terstappen, L. W. M.; Otto, C.; Gac, S. L. Immuno-Capture of Extracellular Vesicles for Individual Multi-Modal Characterization Using AFM, SEM and Raman Spectroscopy. *Lab. Chip* **2019**, *19* (15), 2526–2536. https://doi.org/10.1039/C9LC00081J.

(198) Lässer, C.; Eldh, M.; Lötvall, J. Isolation and Characterization of RNA-Containing Exosomes. *JoVE J. Vis. Exp.* **2012**, No. 59, e3037. https://doi.org/10.3791/3037.

(199) Xu, H.; Liao, C.; Zuo, P.; Liu, Z.; Ye, B.-C. Magnetic-Based Microfluidic Device for On-Chip Isolation and Detection of Tumor-Derived Exosomes. *Anal. Chem.* **2018**, *90* (22), 13451–13458. https://doi.org/10.1021/acs.analchem.8b03272.

(200) Wang, Y.; Li, Q.; Shi, H.; Tang, K.; Qiao, L.; Yu, G.; Ding, C.; Yu, S. Microfluidic Raman Biochip Detection of Exosomes: A Promising Tool for Prostate Cancer Diagnosis. *Lab. Chip* **2020**, *20* (24), 4632–4637. https://doi.org/10.1039/D0LC00677G.

(201) Chen, S.; Shiesh, S.-C.; Lee, G.-B.; Chen, C. Two-Step Magnetic Bead-Based (2MBB) Techniques for Immunocapture of Extracellular Vesicles and Quantification of MicroRNAs for Cardiovascular Diseases: A Pilot Study. *PLOS ONE* **2020**, *15* (2), e0229610. https://doi.org/10.1371/journal.pone.0229610.

(202) Lichtenberg, J. Y.; Ling, Y.; Kim, S. Non-Specific Adsorption Reduction Methods in Biosensing. *Sensors* **2019**, *19* (11), 2488. https://doi.org/10.3390/s19112488.

(203) Contreras-Naranjo, J. E.; Aguilar, O. Suppressing Non-Specific Binding of Proteins onto Electrode Surfaces in the Development of Electrochemical Immunosensors. *Biosensors* **2019**, *9* (1), 15. https://doi.org/10.3390/bios9010015.

(204) Monguió-Tortajada, M.; Gálvez-Montón, C.; Bayes-Genis, A.; Roura, S.; Borràs, F. E. Extracellular Vesicle Isolation Methods: Rising Impact of Size-Exclusion Chromatography. *Cell. Mol. Life Sci.* **2019**, *76* (12), 2369–2382. https://doi.org/10.1007/s00018-019-03071-y.

(205) Ladd Effio, C.; Oelmeier, S. A.; Hubbuch, J. High-Throughput Characterization of Virus-like Particles by Interlaced Size-Exclusion Chromatography. *Vaccine* **2016**, *34* (10), 1259–1267. https://doi.org/10.1016/j.vaccine.2016.01.035.

(206) Liu, F.-K. Analysis and Applications of Nanoparticles in the Separation Sciences: A Case of Gold Nanoparticles. *J. Chromatogr. A* **2009**, *1216* (52), 9034–9047. https://doi.org/10.1016/j.chroma.2009.07.026.

(207) Vilaplana, F.; Gilbert, R. G. Characterization of Branched Polysaccharides Using Multiple-Detection Size Separation Techniques. *J. Sep. Sci.* **2010**, *33* (22), 3537–3554. https://doi.org/10.1002/jssc.201000525.

(208) Tanase, M.; Zolla, V.; Clement, C. C.; Borghi, F.; Urbanska, A. M.; Rodriguez-Navarro, J. A.; Roda, B.; Zattoni, A.; Reschiglian, P.; Cuervo, A. M.; Santambrogio, L. Hydrodynamic Size-Based Separation and Characterization of Protein Aggregates from Total Cell Lysates. *Nat. Protoc.* **2015**, *10* (1), 134–148. https://doi.org/10.1038/nprot.2015.009.

(209) Some, D.; Amartely, H.; Tsadok, A.; Lebendiker, M. Characterization of Proteins by Size-Exclusion Chromatography Coupled to Multi-Angle Light Scattering (SEC-MALS). *JoVE J. Vis. Exp.* **2019**, No. 148, e59615. https://doi.org/10.3791/59615.

(210) Patel, B. A.; Gospodarek, A.; Larkin, M.; Kenrick, S. A.; Haverick, M. A.; Tugcu, N.; Brower, M. A.; Richardson, D. D. Multi-Angle Light Scattering as a Process Analytical Technology Measuring Real-Time Molecular Weight for Downstream Process Control. *mAbs* **2018**, *10* (7), 945–950. https://doi.org/10.1080/19420862.2018.1505178.

(211) Podzimek, S. *Light Scattering, Size Exclusion Chromatography and Asymmetric Flow Field Flow Fractionation: Powerful Tools for the Characterization of Polymers, Proteins and Nanoparticles*; John Wiley and Sons, 2011. https://doi.org/10.1002/9780470877975.

(212) Alamo-Nole, L.; Bailon-Ruiz, S.; Perales-Perez, O.; Roman, F. R. Preparative Size-Exclusion Chromatography for Separation and Purification of Water-Stable Cd-Based Quantum Dots. *Anal. Methods* **2012**, *4* (10), 3127. https://doi.org/10.1039/c2ay25629k.

(213) Berkowitz, S. A.; Houde, D. J. Chapter 7 - Size-Exclusion Chromatograph (SEC) in Biopharmaceutical Process Development. In *Biophysical Characterization of Proteins in Developing Biopharmaceuticals*; Houde, D. J., Berkowitz, S. A., Eds.; Elsevier: Amsterdam, 2015; pp 139–169. https://doi.org/10.1016/B978-0-444-59573-7.00007-5.

(214) Lago, L.; Thomas, O. R. B.; Roberts, B. R. Choice of Mobile Phase: Implications for Size Exclusion Chromatography-Inductively Coupled Plasma-Mass Spectrometry Analyses of Copper, Zinc and Iron Metalloproteins. *J. Chromatogr. A* **2020**, *1616*, 460806. https://doi.org/10.1016/j.chroma.2019.460806.

(215) Ibsen, S.; Sonnenberg, A.; Schutt, C.; Mukthavaram, R.; Yeh, Y.; Ortac, I.; Manouchehri, S.; Kesari, S.; Esener, S.; Heller, M. J. Recovery of Drug Delivery Nanoparticles from Human Plasma Using an Electrokinetic Platform Technology. *Small Weinh. Bergstr. Ger.* **2015**, *11* (38), 5088–5096. https://doi.org/10.1002/smll.201500892.

(216) Pitkänen, L.; Striegel, A. M. Size-Exclusion Chromatography of Metal Nanoparticles and Quantum Dots. *Trends Anal. Chem. TRAC* **2016**, *80*, 311–320. https://doi.org/10.1016/j.trac.2015.06.013.

(217) van Eijndhoven, M. A. J.; Zijlstra, J. M.; Groenewegen, N. J.; Drees, E. E. E.; van Niele, S.; Baglio, S. R.; Koppers-Lalic, D.; van der Voorn, H.; Libregts, S. F. W. M.; Wauben, M. H. M.; de Menezes, R. X.; van Weering, J. R. T.; Nieuwland, R.; Visser, L.; van den Berg, A.; de Jong, D.; Pegtel, D. M. Plasma Vesicle MiRNAs for Therapy Response Monitoring in Hodgkin Lymphoma Patients. *JCI Insight 1* (19), e89631. https://doi.org/10.1172/jci.insight.89631.

(218) Böing, A. N.; van der Pol, E.; Grootemaat, A. E.; Coumans, F. A. W.; Sturk, A.; Nieuwland, R. Single-Step Isolation of Extracellular Vesicles by Size-Exclusion Chromatography. *J. Extracell. Vesicles* **2014**, *3*. https://doi.org/10.3402/jev.v3.23430.

(219) Sorensen, E. N.; Weisman, G.; Vidaver, G. A. A Sephadex Column Procedure for Measuring Uptake and Loss of Low Molecular Weight Solutes from Small, Lipid-Rich Vesicles. *Anal. Biochem.* **1977**, *82* (2), 376–384. https://doi.org/10.1016/0003-2697(77)90175-0.

(220) Barenholz, Y.; Gibbes, D.; Litman, B. J.; Goll, J.; Thompson, T. E.; Carlson, R. D. A Simple Method for the Preparation of Homogeneous Phospholipid Vesicles. *Biochemistry* **1977**, *16* (12), 2806–2810. https://doi.org/10.1021/bi00631a035.

(221) Schurtenberger, P.; Hauser, H. Characterization of the Size Distribution of Unilamellar Vesicles by Gel Filtration, Quasi-Elastic Light Scattering and Electron Microscopy. *Biochim. Biophys. Acta BBA - Biomembr.* **1984**, *778* (3), 470–480. https://doi.org/10.1016/0005-2736(84)90396-1.

(222) Ruysschaert, T.; Marque, A.; Duteyrat, J.-L.; Lesieur, S.; Winterhalter, M.; Fournier, D. Liposome Retention in Size Exclusion Chromatography. *BMC Biotechnol.* **2005**, *5*, 11. https://doi.org/10.1186/1472-6750-5-11.

(223) Messaud, F. A.; Sanderson, R. D.; Runyon, J. R.; Otte, T.; Pasch, H.; Williams, S. K. R. An Overview on Field-Flow Fractionation Techniques and Their Applications in the Separation and Characterization of Polymers. *Prog. Polym. Sci.* **2009**, *34* (4), 351–368. https://doi.org/10.1016/J.PROGPOLYMSCI.2008.11.001.

(224) Kowalkowski, T.; Buszewski, B.; Cantado, C.; Dondi, F. Field-Flow Fractionation: Theory, Techniques, Applications and the Challenges. *Crit. Rev. Anal. Chem.* **2006**, *36* (2), 129–135. https://doi.org/10.1080/10408340600713702.

(225) Reschiglian, P.; Zattoni, A.; Roda, B.; Michelini, E.; Roda, A. Field-Flow Fractionation and Biotechnology. *Trends Biotechnol.* **2005**, *23* (9), 475–483. https://doi.org/10.1016/j.tibtech.2005.07.008.

(226) Giddings, J. C.; Yang, F. J.; Myers, M. N. Flow-Field-Flow Fractionation: A Versatile New Separation Method. *Science* **1976**, *193* (4259), 1244–1245. https://doi.org/10.1126/science.959835.

(227) Schimpf, M. E.; Caldwell, K.; Giddings, J. C. *Field-Flow Fractionation Handbook*; John Wiley & Sons, 2000.

(228) Gale, B. K.; Srinivas, M. Cyclical Electrical Field Flow Fractionation. *ELECTROPHORESIS* **2005**, *26* (9), 1623–1632. https://doi.org/10.1002/elps.200410296.

(229) Palkar, S. A.; Schure, M. R. Mechanistic Study of Electrical Field Flow Fractionation. 1. Nature of the Internal Field. *Anal. Chem.* **1997**, *69* (16), 3223–3229. https://doi.org/10.1021/ac9700134.

(230) Drexel, R.; Sogne, V.; Dinkel, M.; Meier, F.; Klein, T. Asymmetrical Flow Field-Flow Fractionation for Sizing of Gold Nanoparticles in Suspension. *J. Vis. Exp. JoVE* **2020**, No. 163. https://doi.org/10.3791/61757.

(231) Müller, D.; Cattaneo, S.; Meier, F.; Welz, R.; deMello, A. J. Nanoparticle Separation with a Miniaturized Asymmetrical Flow Field-Flow Fractionation Cartridge. *Front. Chem.* **2015**, *0*. https://doi.org/10.3389/fchem.2015.00045.

(232) Abdolahpur Monikh, F.; Grundschober, N.; Romeijn, S.; Arenas-Lago, D.; Vijver, M. G.; Jiskoot, W.; Peijnenburg, W. J. G. M. Development of Methods for Extraction and Analytical Characterization of Carbon-Based Nanomaterials (Nanoplastics and Carbon Nanotubes) in Biological and Environmental Matrices by Asymmetrical Flow Field-Flow Fractionation. *Environ. Pollut.* **2019**, *255*, 113304. https://doi.org/10.1016/j.envpol.2019.113304.

(233) Ashby, J.; Schachermeyer, S.; Pan, S.; Zhong, W. Dissociation-Based Screening of Nanoparticle–Protein Interaction via Flow Field-Flow Fractionation. *Anal. Chem.* **2013**, *85* (15), 7494–7501. https://doi.org/10.1021/ac401485j.

(234) Quattrini, F.; Berrecoso, G.; Crecente-Campo, J.; Alonso, M. J. Asymmetric Flow Field-Flow Fractionation as a Multifunctional Technique for the Characterization of Polymeric Nanocarriers. *Drug Deliv. Transl. Res.* **2021**, *11* (2), 373–395. https://doi.org/10.1007/s13346-021-00918-5.

(235) K. Kari, O.; Ndika, J.; Parkkila, P.; Louna, A.; Lajunen, T.; Puustinen, A.; Viitala, T.; Alenius, H.; Urtti, A. In Situ Analysis of Liposome Hard and Soft Protein Corona Structure and Composition in a Single Label-Free Workflow. *Nanoscale* **2020**, *12* (3), 1728–1741. https://doi.org/10.1039/C9NR08186K.

(236) Rampado, R.; Crotti, S.; Caliceti, P.; Pucciarelli, S.; Agostini, M. Recent Advances in Understanding the Protein Corona of Nanoparticles and in the Formulation of "Stealthy" Nanomaterials. *Front. Bioeng. Biotechnol.* **2020**, *0*. https://doi.org/10.3389/fbioe.2020.00166.

(237) Optimization of Asymmetrical Flow Field-flow Fractionation (AF4) https://www.chromatographyonline.com/view/optimization-asymmetrical-flow-field-flow-fractionation-af4 (accessed 2021 -08 -02).

(238) Dou, H.; Li, Y.; Choi, J.; Huo, S.; Ding, L.; Shen, S.; Lee, S. Asymmetrical Flow Field-Flow Fractionation Coupled with Multiple Detections: A Complementary Approach in the Characterization of Egg Yolk Plasma. *J. Chromatogr. A* **2016**, *1465*, 165–174. https://doi.org/10.1016/j.chroma.2016.08.062.

(239) Eskelin, K.; Poranen, M. M.; Oksanen, H. M. Asymmetrical Flow Field-Flow Fractionation on Virus and Virus-Like Particle Applications. *Microorganisms* **2019**, *7* (11), 555. https://doi.org/10.3390/microorganisms7110555.

(240) Oles, V. Shear-Induced Aggregation and Breakup of Polystyrene Latex Particles. *J. Colloid Interface Sci.* **1992**, *154* (2), 351–358. https://doi.org/10.1016/0021-9797(92)90149-G.

(241) Otte, T.; Pasch, H.; Macko, T.; Brüll, R.; Stadler, F. J.; Kaschta, J.; Becker, F.; Buback, M. Characterization of Branched Ultrahigh Molar Mass Polymers by Asymmetrical Flow Field-Flow Fractionation and Size Exclusion Chromatography. *J. Chromatogr. A* **2011**, *1218* (27), 4257–4267. https://doi.org/10.1016/j.chroma.2010.12.072.

(242) Makan, A. C.; Otte, T.; Pasch, H. Analysis of High Molar Mass Branched Polybutadienes by SEC-MALLS and AF4-MALLS. *Macromolecules* **2012**, *45* (12), 5247–5259. https://doi.org/10.1021/ma3007812.

(243) Ashby, J.; Schachermeyer, S.; Duan, Y.; Jimenez, L. A.; Zhong, W. Probing and Quantifying DNA–Protein Interactions with Asymmetrical Flow Field-Flow Fractionation. *J. Chromatogr. A* **2014**, *1358*, 217–224. https://doi.org/10.1016/j.chroma.2014.07.002.

(244) Schachermeyer, S.; Ashby, J.; Zhong, W. Aptamer–Protein Binding Detected by Asymmetric Flow Field Flow Fractionation. *J. Chromatogr. A* **2013**, *1295*, 107–113. https://doi.org/10.1016/J.CHROMA.2013.04.063.

(245) Zhang, H.; Lyden, D. Asymmetric Flow Field-Flow Fractionation Technology for Exomere and Small Extracellular Vesicle Separation and Characterization. *Nat. Protoc.* **2019**, *14* (4), 1027–1053. https://doi.org/10.1038/s41596-019-0126-x.

(246) Field-Flow Fractionation - The Universal Separation Principle for Particle and Macromolecule Characterization - https://www.chemeurope.com/en/whitepapers/123157/field-flow-fractionation-the-universal-separation-principle-for-particle-and-macromolecule-characterization.html (accessed 2021 -08 -02).

Chapter 2: Asymmetrical Flow Field Flow Fractionation Coupled to Nanoparticle Tracking Analysis for Rapid Online Characterization of a Mixture of Polystyrene Beads

This chapter describes the fluidic connection between AF4 and NTA for simultaneous online counting and sizing while fractionating mixtures of NP sizes.

2.1 Introduction

Nanotechnology has been integrated into a wide array of consumer products, urging governing bodies of these markets to adopt guidelines or regulations regarding the reporting and characterization of those nanomaterials due to their possible adverse environmental or biological effects.[1–6] The first regulation of nanomaterial reporting and labeling in consumer goods was established by the European Union (EU) for cosmetic products being sold in the EU market in 2009.[7] Specifically, the regulation asks: 1) does a product contain nanomaterials that need to be reported; 2) does the size of the nanomaterial fall within the regulation of 1-100 nm; and 3) what is the number size distribution of the nanomaterials?[8] The most challenging requirement in this regulation is the determination of a number size distribution. This means the distribution must be generated from counted nanoparticles that have been sized individually, but not from measurement of the bulk solution. Similarly, in the US, the Food and Drug Administration (FDA) requires that, if a product contains nanomaterials, specific information about the physiochemical properties,

purity, and toxicity of the nanomaterials must be provided.[9] The guidelines of the FDA also demands that the aggregation and agglomeration properties of the nanomaterials in the product should be revealed.

Several techniques exist to satisfy these regulations, but they usually are technically demanding, involve expensive instruments, and need multiple analyses to perform a full characterization. Offline techniques like transmission electron microscopy (TEM)[10], atomic force microscopy (AFM)[11], and scanning electron microscopy (SEM)[12] can produce number counting as well as size, but these methods are low in throughput and often require surface adsorption and drying, which may not capture the total concentration or observe the nanoparticles in their native state in the sample matrix. Access may also be limited to sub 100 nm resolution instruments due to the cost of instruments. Resistive pulse sensing (RPS) is another powerful technique that can individually size nanoparticles in solution, but the low throughput of having to inject samples and the variation of the data with respect to the pore size used in the instrument complicate the data analysis and limit this technology in rapid nanoparticle quantification.[13,14]

NTA is powerful because of the counting ability and is quite promising as an online detector due to the fluidic channel design.[15–18] AF4 is compatible with many different detectors in online and offline configurations such as DLS,[19,20] MALS,[21–25] LC-MS,[26–28] ICP-MS,[29–34] and Raman spectroscopy[35] due to the low operating pressures, wide range of compatible running buffers, and simple fluidic connections. It is reasonable to consider AF4 the best candidate for online NTA over SEC high operating pressures. To our knowledge, there has been no modular LC detector that can count particles individually to

create number distributions configured for online use. As an added advantage, the individual counting allows coeluted populations to be visible on the 3D contour plot that may have normally been disguised in the bulk analysis and could reduce a drawback of AF4.

The following chapter proposes a design for a simple connection interface between NTA and AF4, and the resultant set-up allows rapid particle separation followed by online number distributions at the time of fractionation. We have demonstrated that the connection design can successfully reduce the channel back-pressure and direct the eluent from AF4 to NTA at the desired flow rates for accurate particle sizing. This system can separate and analyze a range of nanomaterial types, has good capacity for different injection volumes and sample concentrations, quick counting and sizing capability, and does this label-free.

2.2 - Methods

2.2.1 - Reagents and Materials.

Polystyrene bead standards with an average diameter of 50 nm, 100 nm, 200 nm, and FL-70 detergent were purchased from Thermo Fisher Scientific (Waltham, MA). NanoXact gold nanorods with the dimensions of 45.5×17.3 nm (Cat # GRCN660-25M) and 69.3×12.0 nm (Cat# GRCN980-10M) were purchased from nanoComposix (San Diego, CA). The 2D nanomaterial of hexagonal boron nitride (hBN) with the average lateral dimension around 150 nm and layer thickness < 10 nm was obtained from the Harvard HSPH-HIEHS Nanosafety Center, the detailed characterization of which was reported in our previous work.[37] A SLI-0430 Sensirion flow sensor kit was purchased from Newark (Centerville, OH) for NTA flow rate measurements. A 9-port manifold was

purchased from Upchurch Scientific (Lakeforest, IL). Ultrapure H_2O (18.2 MΩ) was generated onsite with a Direct-Q 3 UV water purification system (Millipore Sigma; Burlington, MA).

2.2.2 - COMSOL Flow Rate Simulations

COMSOL5.3a simulations were done for different port designs (Y-split, T-split, and multiple port manifolds) to see the best strategy for reducing and controlling the flow rate going to the NTA and FC. The inflow port was set at a constant flow rate of 500 µL/min to simulate the separation conditions for the polystyrene size standards. The inner diameter (ID) of the tubing was kept at 0.02" for all lines, which is the ID of the AF4 tubing running to the UV-Vis detector. To simulate the changes in flow rates due to liquid pump check valves, a sigmoidal function was applied to the inflow in a time dependent solver to add oscillations to the steady flow rate. Boundary conditions of each exit port was set to pressure at zero for open-ended lines or at a constant flow rate to simulate a syringe pump withdrawing at a constant rate. Water was used as the solvent to simulate the aqueous buffers used in AF4.

2.2.3 - AF4-NTA Coupling Connection

Scheme 1 shows the fluidic connection of our setup. A 9-port manifold was attached after the UV-Vis detector and before the NTA channel to split the AF4 line into multiple flow paths, thus reducing the total pressure in each line as well as the reducing the split flow rate ratio between the eluent and NTA. One line was attached directly into the low volume flow cell manifold, while the other three lines were connected to the fraction collector (FC) with equal length tubing. The waste port of the NTA was connected to a New Era NE-500-X

syringe pump controlled by. The lines were purged of air before equilibration. The desired flow rate (15 µL/min) was set in the Syringe Pump Pro software and allowed to equilibrate after gently withdrawing with the syringe pump.

2.2.4 - AF4 Separations

Nanoparticle separations were carried out on a Postnova AF2000 AF4 instrument utilizing an analytical scale channel with a regenerated cellulose membrane sheet having a MWCO value of 10 kDa (Postnova Analytics). The system uses a Shimadzu SPD-20A Prominence UV-Vis detector, and the nanoparticles were measured at 265 nm. A running buffer of 0.1 % FL-70 was freshly prepared daily and filtered with 0.22 µm PVDF membrane to remove any crystals or debris from the running buffer.

The AF4 separation method was developed using the standard polystyrene particles with average diameters of 50 nm, 100 nm, and 200 nm. A graphical display of this method is shown in Figure 2.1. The method starts with a focus, tip, and cross flow of 2.95, 0.30, and 2.75 ml/min, respectively, to allow the sample to be focused in a narrow region at the top of the channel. A focus time of 7 minutes was used to ensure the particles start in a tight band before separation. At the start of separation, the crossflow switches to 1.25 mL/min while the focus flow is turned off and the crossflow is linearly decayed to 0.10 mL/min over 50 minutes. The 0.10 mL/min is maintained for another 10 minutes until the end of the run.

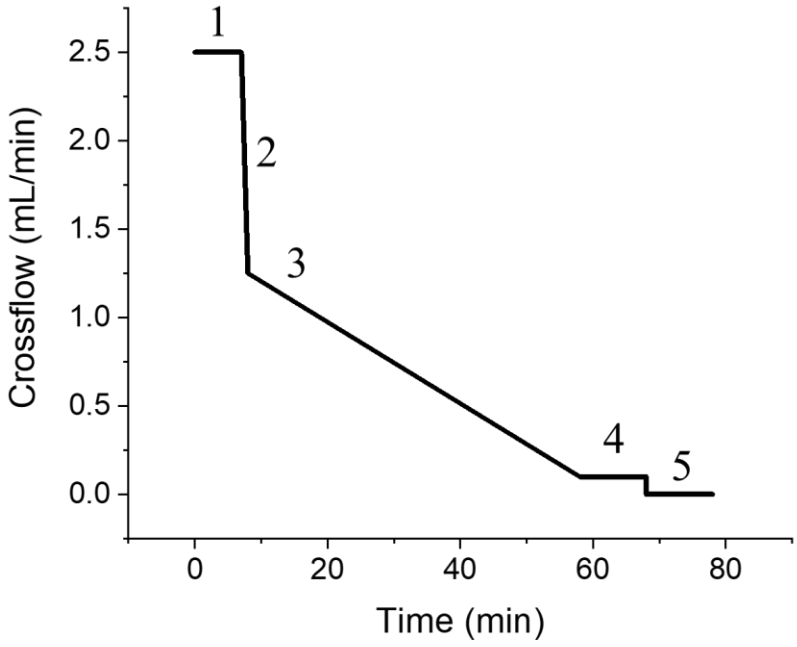

Figure 2.1 - AF4 method graphical display showing the crossflow rate at each point in the separation. The detector flowrate was kept constant at 0.500 mL/min throughout the run. (1) Focusing time of 7 minutes. (2) Transition from focus to separation flows over 1 minute. (3) Separation flow starts at 1.25 mL/min and decays to 0.10 mL/min over 50 minutes. (4) Cross flow at 0.10 mL/min for 10 minutes to elute remaining particles. (5) Rinse flow of 0.00 mL/min cross flow and 0.50 mL/min detector flow to clean membrane.

2.2.5 - Nanoparticle Analysis using NTA

Particle counting was carried out on a Nanosight NS300 from Malvern Panalytical using a low volume flow cell manifold and a 405 nm laser module. For online analysis, time points with 1-minute intervals were selected for NTA analysis to ensure enough nanoparticles are measured per video collection. The video collection time was determined as 60 s minus the processing time of each video, which was 5 s on the current CPU of the system, making the video collection time 55 s. Detection threshold (DT) was kept at 4, with camera levels being dictated by the particle's optical properties. For analysis of

```
CAMERALEVEL 13
DETECTTHRESHOLD 4
DELAY 1020
REPEATSTART
CAPTURE 55
REPEAT 19
REPEATSTART
CAMERALEVEL 11
CAPTURE 55
REPEAT 19
REPEATSTART
CAMERALEVEL 6
CAPTURE 55
REPEAT 19
```

Figure 2.2 - NTA script when analyzing eluent from AF4. The script sets the camera level (CL) and detection threshold (DT) and waits 17 minutes before collecting videos. The system then collects 20 videos at CL 13 and DT 4, then changes the CL to 11 and collects t twenty videos, and then finally switches to CL 6 and collects 20 videos.

mixtures, the camera level was reduced in steps over the separation to avoid oversaturation of the camera when larger particles were being measured. For the polystyrene bead mixture, the camera level (CL) started at 13 for 20 minutes and then decreased to 10 for 20 minutes, before finally dropping to 6 for the final 20 minutes. A flow sensor was connected to the exit port of NTA to monitor flow rates throughout the run. A flow rate of 15 µL/min was induced by withdrawing a connected syringe using a New Era NE-500X syringe pump. Figure 2 shows an example script of online NTA data collection.

Offline analysis was performed using similar conditions with the video capture time of 55 seconds and DT of 4. CL was adjusted per population as necessary before analysis and was the basis for the CLs used during the separation. A Harvard syringe pump was used to push offline samples through the flow cell. Flow rates were set to 15 µL/min using the generated standard curve (Figure 3). A setting of 70 generated a flow of ~15 µL/min.

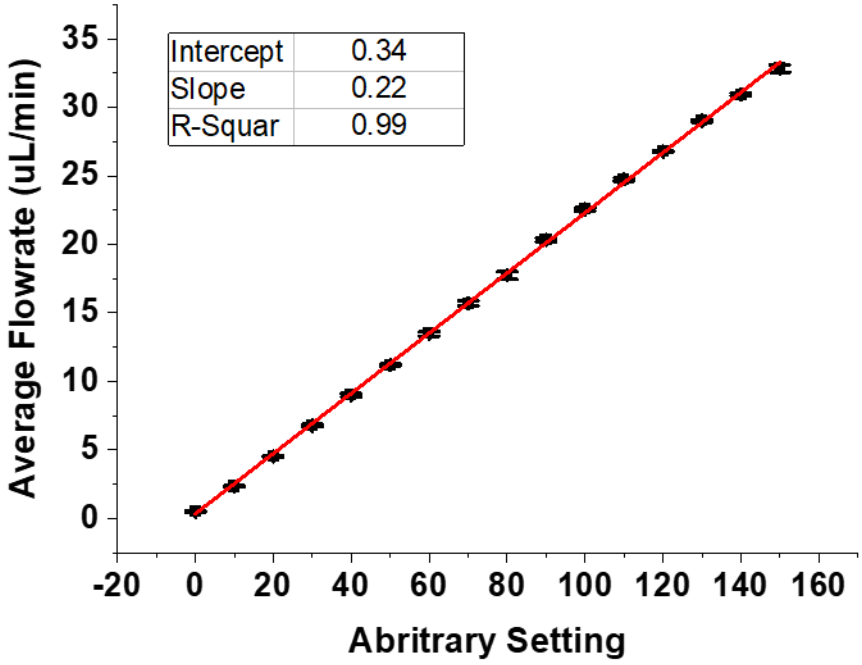

Figure 2.3 - Arbitrary syringe pump setting calibration curve. The flowrate was measured at the exit port of the NTA using a Sensirion flow sensor. The error bar is the standard deviation between the three trials of individual 50 nm, 100 nm, and 200 nm PS bead maximum flow rate experiments.

2.2.6 - Nanoparticle Sample Preparation and Separation

Stock solutions of the polystyrene particles with diameters of 50 nm, 100 nm, and 200 nm were diluted in 0.1% FL-70 to make solutions that contained comparable particle counts for all sizes after AF4. Due to the differences in recovery based on size and elution time in AF4, the 200-nm particles were at a 10× higher concentration than the 50- and 100-nm ones. Samples were sonicated for 2 minutes at 90% power using a 2s on and 2s off pulsing method directly before injection. For comparison of the single versus mixed population, 10 µL of each size was injected individually, and then mixed to make a 30-µL

mixture for injection. For comparison of the online versus offline analysis, 30 µL of the mix was injected and collected, with the collected fractions undergoing offline NTA analysis. For the standard curves with increasing injection amounts, 6, 12, 18, 24, and 30 µL of the mix was injected sequentially.

2.2.7 - Data Analysis

Online NTA data files were processed using the Malvern NTA 3.3 software and the resulting experiment summary file was used as the data matrix. Each 55-s video and the resultant distribution was shown as one entry in the summary file, and the summary file containing all video entries was viewed as the result for one separation experiment. The matrix from the file was used to generate the 3D contour map in Origin Pro 2020 software. Processing of the video files were done after each separation using a single script command or done at the end of the day's experiments with a combined file using the NTA merge file command. The file combination increased throughput as multiple runs were collected, and the file processed overnight. To make the graphs visually presentable, a baseline of 1×10^6 was set in the 3D contour plot; however, this baseline was not used in the quantification analysis. The volume area is defined by the Region of Interest Box (ROI Box). The volume under each peak resulted in a volumetric particle concentration (min × particles/mL). To extract total nanoparticle counts, the volumetric particle concentration was multiplied by the AF4 detector flow rate before the splitter manifold (0.5 mL/min) resulting in the number of particles eluted within each ROI. This value defines the number of particles per size bin, which was 1 nm for all analyses. This distribution shows the number of particles per size bin, which is the definition of a number distribution.

2.3 - Results and Discussion

2.3.1 - Flow Splitting Design and COMSOL Simulations

The outlet flow rate of AF4 can be as low as 0.1 mL/min up to a few mL/min, which is much higher than the NTA channel limitations. Therefore, to use NTA as an online detector, a flow splitter is needed to direct only a small portion of the AF4 eluent to NTA at compatible flow rates. As shown in Figure 2.4, we solved this issue by using a multi-port manifold (part C in Figure 2.4). The challenge of such a junction design is to maintain a highly consistent flow rate going into NTA regardless of any pressure changes occurring in the AF4 channel. This is because a typical AF4 separation method gradually decreases crossflow to obtain optimal elution times and resolution while the system pressure decreases to maintain constant outlet flow rate. This constant flow rate but variable system pressure limits the ability to split and control flow with static back pressure regulators, such as smaller ID tubing, or through hydrodynamic pressures using exit ports with different heights relative to each other. In our design, a syringe pump (part E in Figure 2.4) is connected to the exit port of NTA to withdraw liquid through NTA at a constant flow rate. The constant flow rate provided by the syringe pump would also maintain a stable back pressure in the NTA line, owing to the incompressibility of the liquid and components in that line. In this way, the flow rate in the NTA line could be controlled constant and at the desired value, while the FC flow rates from other outlets of the multi-port manifold would vary slightly in response to the pressure change in the AF4 system. The small ~5 µL/min fluctuations can affect the NTA data analysis but will not affect the FC performance in the slightest.

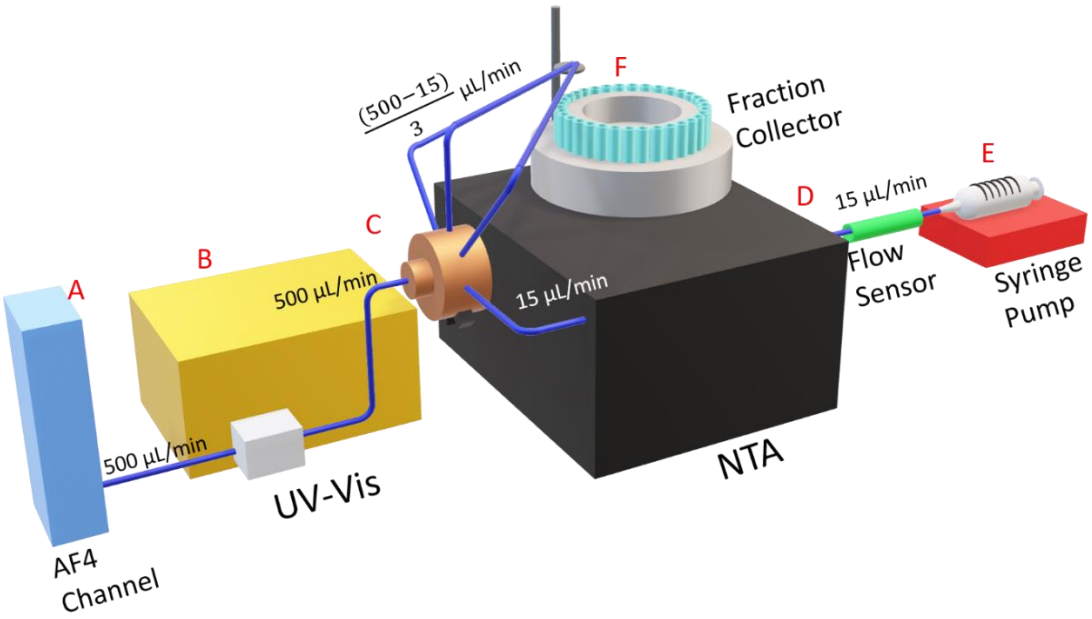

Figure 2.4 - Schematic of AF4-NTA Connection. Eluent from the AF4 channel (A) is pushed at a constant 500 µL/min through the UV-Vis (B) until the flow is split at the splitter manifold (C). The line feeding the NTA is kept at a constant 15 µL/min by the flow sensor (D) and syringe pump (E). The remaining eluent lines feed the fraction collector. (F) The fraction collector flow rate can be calculated by:

$$FC\ Lines\ Flow\ Rate = \frac{AF4\ Detector\ Flow\ Rate\ - NTA\ Detector\ Flow\ Rate}{Number\ of\ FC\ Lines}$$

COMSOL simulations were employed to prove the plausibility of our design. The simulation was set up in the way that, the splitter would have even output flow rate at all outlets when a time dependent solver showed no modulations in the inflow of fluid; but when the flow rate changed, mimicking the conditions commonly seen in AF4 separations due to pressure fluctuations from liquid pump check valves, the flow rates in the FC lines changed, with a boundary constraint put on the NTA line to fix its flow rate as constant. Figure 2.5 in Supporting Information shows the simulation result of a 4-port manifold, with

the pressure modulated by a sigmoidal function to imitate flow rate fluctuations in the AF4 system. The simulation result shows that, the sigmoidal fluctuation in the AF4 flow rate only affected the rates in the lines heading towards the FC, while a constant, steady flow rate was seen in the NTA.

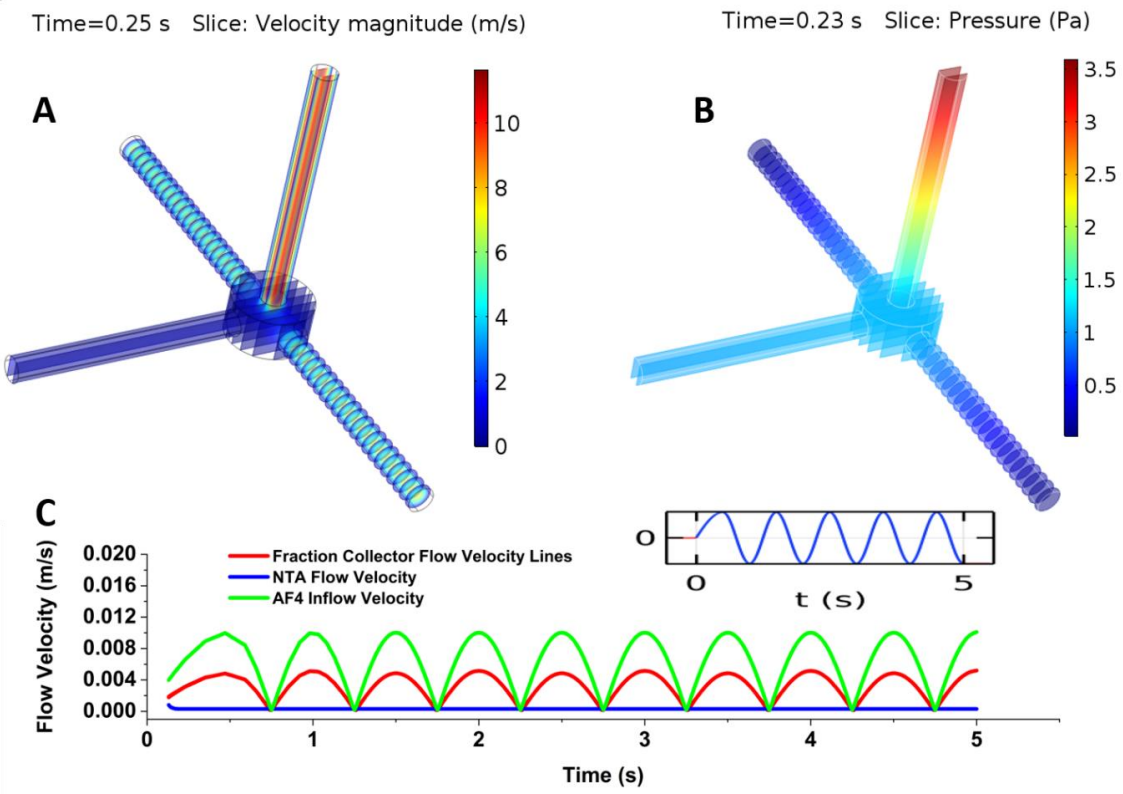

Figure 2.5 - COMSOL simulations of flowrates using a fluctuating inflow with a constant NTA line outflow. Fluctuations in pressure or flowrate are seen in the fraction collector lines and not seen in the syringe pump-controlled line. Flowrate (A) and pressure (B) of resulting fluctuations at shown time points. Resulting flowrates (C) of simulation taken at 0.01 s intervals. FC line #1 and #2 are equal and show up as FC line. Inset of (C) shows the sigmoidal function used to modulate the flowrate over time to simulate inconsistent flowrates caused by pump functions.

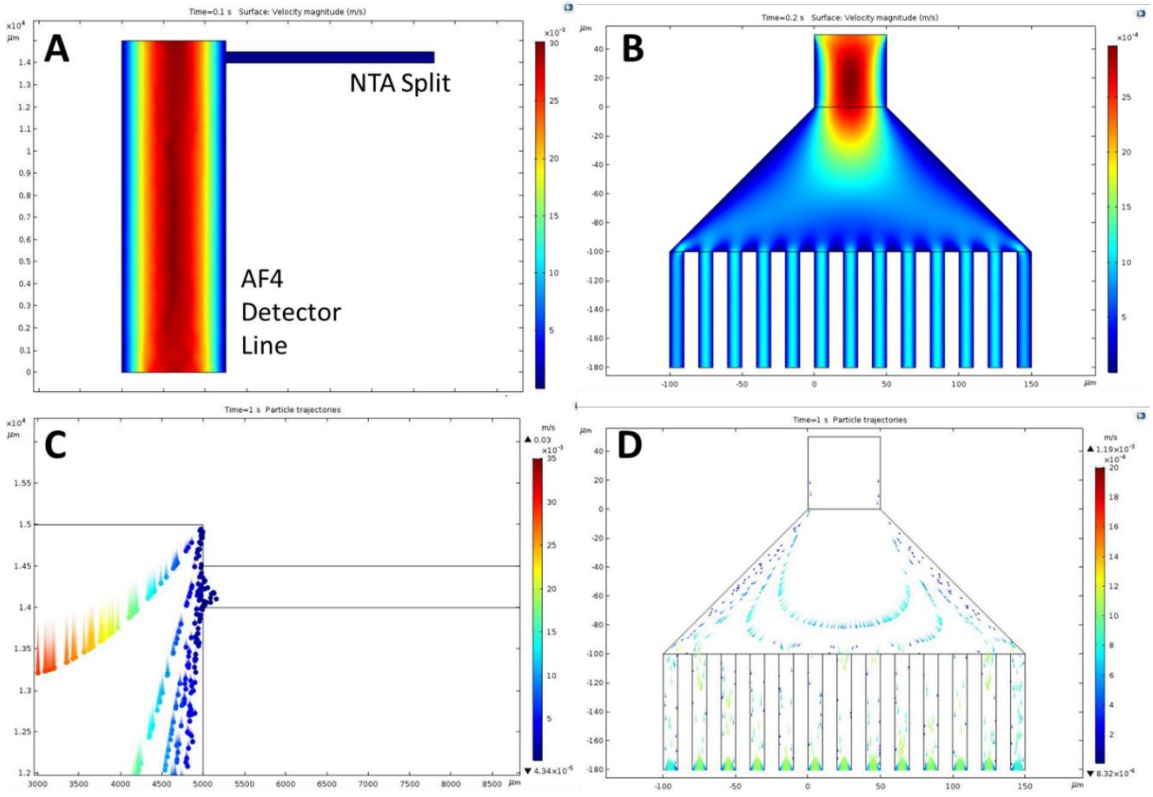

Figure 2.6 - COMSOL flowrate and NP flow of a simulated T junction and splitter manifold. The T junction shows a high split flow ratio of 66:1, which would translate into an eluent flow of 1.0 mL/min and a NTA flow of 15 µL/min.

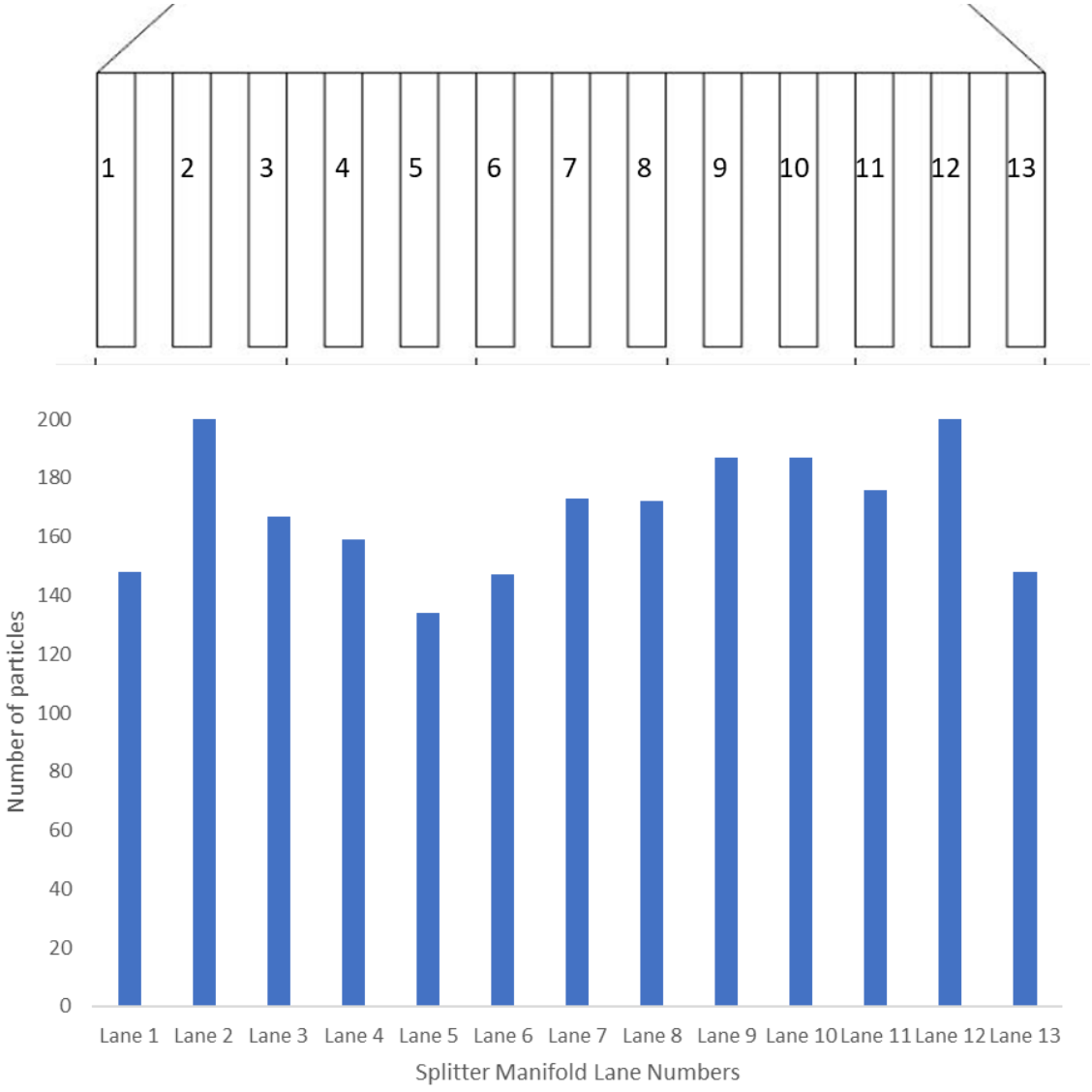

Figure 2.7 - NP flow into a splitter manifold of evenly split lines.

COMSOL simulations were ran on a T-junction and splitter manifold showing the flowrate split and NP flow at a theoretical junction. Figure 2.6 shows the simulation results. The Figure 2.6A and 2.6C show the flow rate and NP flow T-junction split uses a narrow ID tubing to regulate the backflow, which is a common coupling technique to control flow rate. AF4 eluent flows at higher rates (1.0 mL/min) than the split slow (15

µL/min) creates a high split flow ratio of 66:1. The NP flow in this condition shows numerous NPs flowing past while only a small percentage is captured by the split flow. A way to visualize the split flow ratio is there are 66 boundary layers going to the FC while 1 boundary layer goes to the NTA. Only the slowest layer at the edge of the tubing is fed into the NTA. This limits the NTA sampling to only NPs that are traveling close to the edges of the tubing. This is thought to be the source of irreproducibility observed in the early attempts at connecting the two instruments. As a comparison, a splitter manifold design was tested using multiple split lines. Figure 2.6B and 2.6D show a much better spread as each line is split evenly as seen in Figure 2.7. The splitter manifold design is not ideal because the simulation required 2-D shape for computation time, and thus caused a flat design of a circular splitter manifold. This causes some of the edge lanes to have less particles while the neighboring lane has the missing particles, but the rest of the lanes are expected to be similar in flow to a three-dimensional shape using the same split design. The effect the multiple line design does is this effectively reduces the split flow ratio because the NTA line will still be 15 µL/min but each line at the split is reduced based on how many lines are open. With a theoretical situation like Figure 6 of 13 lanes with one going to the NTA at 15 µL/min, the 12 other lines would only have 83.3 µL/min instead of the 985 µL/min the T-junction split has. The new split flow ratio would be 5.5:1. Even though the total split flow ratio is still 66:1 when you total the 12 lines together, the NTA line will have 1/5 the laminar flow boundary layers as the other lines instead of 1/66 and would have a much better representation of the eluent sample plug. These revelations

confirmed the splitter manifold gave the best chance to control pressure, flow rate, and split flow ratio to ensure good reproducibility between runs.

One experimental factor that was unknown was the channel design of the NTA Low Volume Flow Cell. The flow cell has complex geometries as well as pressure release points that make accurate modeling of the channel too difficult. In most simulations, the resulting overall pressure would have been too high for the NTA channel to successfully control the flow without risking high amounts of leaking or over pressurization of the plastic NTA channel, leading to cracks. To maintain a low volume flow rate in the NTA line and accommodate a wide range of system pressure in AF4, instead of using a 4-port manifold as done in Figure 4, a 9-port manifold was employed in our design. More ports of the splitter manifold allowed additional exit lines to be opened, which also reduced the total pressure in each FC line to be close to atmospheric and eliminated the risk of leakage and damage to the NTA channel. For example, if a system runs at 3-4 bar during separation, opening 1 NTA line and 3 FC lines was sufficient to keep the total pressure in each line at 1 bar or less.

Another important aspect of the connection design was the tubing length and physical rejoining of the FC lines. To reduce band broadening and retention time shifts due to the drastically different flow rates, the tubing length after the splitter going to the NTA must be reduced to a minimal amount as well as connected into the “short” end of the channel that feeds directly into the viewing window (See Figure 2.8). Additionally, the lines feeding the FC must be kept to identical lengths or the sample bands would not be delivered at the same time into the collection tubes. Finally, the FC lines must be kept open

to atmosphere and not be rejoined using a second manifold to prevent over pressurization of the NTA channel.

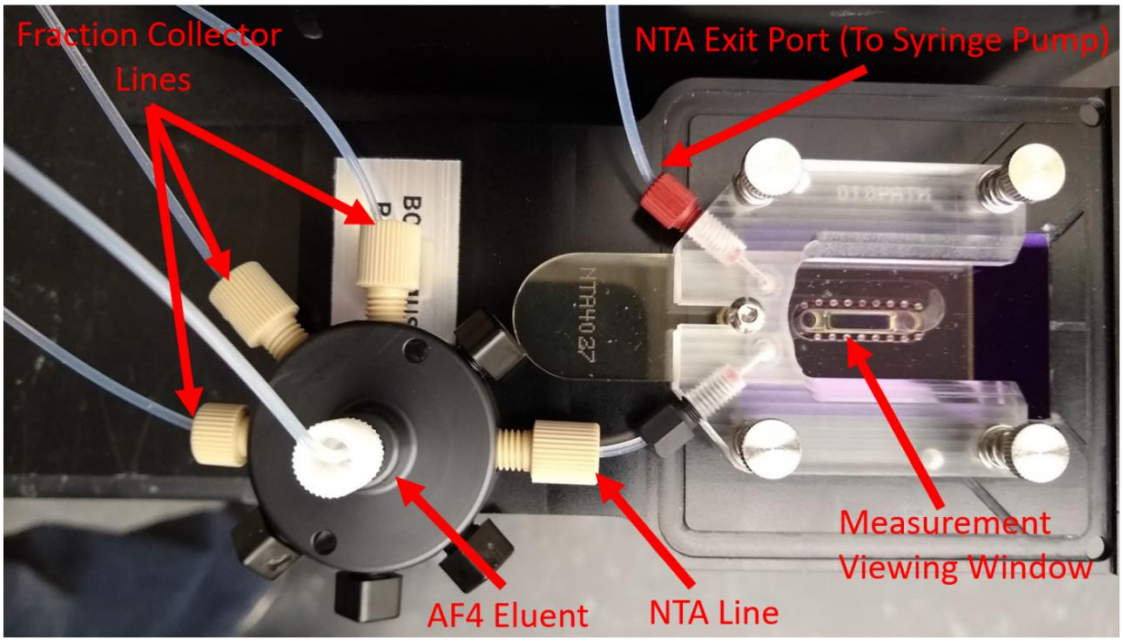

Figure 2.8 - Picture showing the splitter manifold connection to the low volume flow cell of the NTA sitting on top of the laser module. The tubing length must be a minimum amount as the slow flow rate causes band broadening with this short of a connection. The number of FC ports connected are dictated by system pressure. The pressure and flowrate coming from the AF4 eluent is split between all the open ports, including the NTA line.

The effectiveness of using a syringe pump at the exit port of NTA to control constant flow rates in NTA while connected to AF4 was tested experimentally against the hydrodynamic control, i.e., using the height difference between the NTA and FC exit ports to control the flow rate in the NTA line. Due to continuous pressure change throughout the AF4 separation process, the hydrodynamic control method was not able to maintain a steady flow rate and thus would only be accurate for a small range of separation conditions (Figure 2.9A). In contrast, using a syringe pump provided a nice consistent flow rate over

the whole separation. In addition, the minor pulses of the flow rate generated from the check valves were mostly eliminated (Inset of Fig. 2.9A).

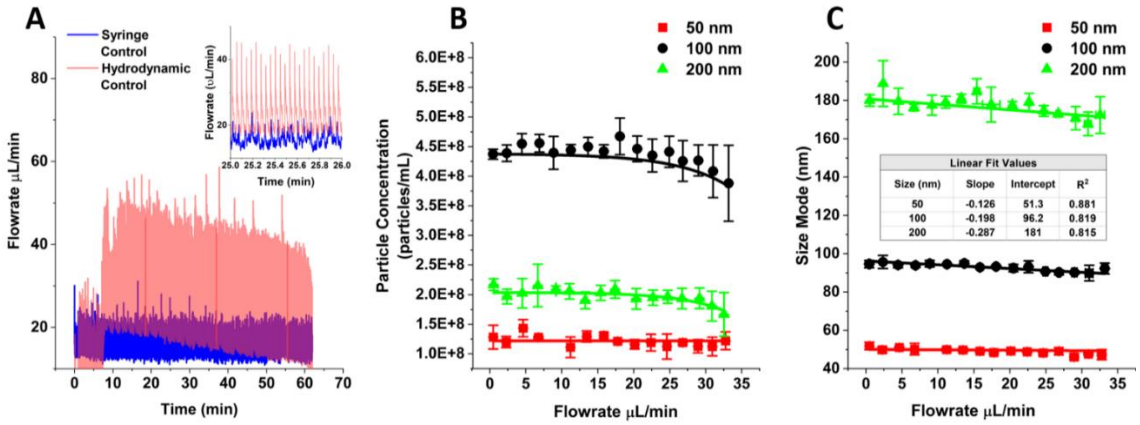

Figure 2.9 - Flow rate control and maximum flow rate determination. Hydrodynamic-controlled flow rates and syringe pump-controlled flow rates are shown in (A) and a zoomed scale in (Inset). (B) Particle concentration maximum flow rate that was determined by the intersection of the linear portions of the exponential function. (C) Maximum flow rates were determined by determining a 5% error tolerance and solving for the value at 0 µL/min flow rate multiplied by 0.95 for size mode.

2.3.2 - NTA Maximum Flow Rate Determination

The Malvern NTA 3.3 software measures the speed of Brownian motion of each particle to calculate its size. Since the particle moves together with the NTA channel flow, correction for a particle's velocity is made by taking the average velocity and direction of all particles for a certain number of advanced frames, then removing that average particle drift from each particle's measurement. This processing can cause differences in particle sizing and counting depending on the flow rate of the medium the particle is suspended in. A flow rate too high would decrease accuracy in particle sizing. To determine the maximum flow rate the AF4-NTA system can handle, a calibrated flow sensor was

connected directly after the NTA exit port. Then, we controlled the syringe pump setting to result in different flow rates in the NTA channel (Figure 2.3) and investigated the effect of flow rates on the analysis of the polystyrene size standards.

We found that, the particle concentration (Figure 2.9B), as well as the size mean and mode (Figure 2.9C), of the 100- and 200-nm particles decreased as the flow rate increased; while the smaller, 50-nm particles were affected less within this flow rate range. The maximum flow rate was then determined as the rate able to induce 5% change in particle concentration and size mode compared to the average values measured at all slower rates. Using particle concentration, the maximum flow rate for 100 nm and 200 nm was estimated to be 30.0 µL/min and 27.75 µL/min, respectively, but change in particle concentration for the 50-nm particles was smaller than 5% in the entire flow rate range investigated. On the other hand, using size mode, the maximum flow rate for the 50-, 100- and 200-nm particles was found to be, 34.84 µL/min, 31.96 µL/min, and 16.08 µL/min respectively. Since the smallest flow rate determined was 16.08 µL/min from the size mode analysis, a flow rate of 15.00 µL/min was employed as the operating flow rate for online NTA analysis in the present work.

2.3.3 - Polystyrene Bead Standard Analysis

The purpose of building the AF4-NTA system is to provide accurate and repeatable counting of each particle population in a nanoparticle mixture as it is fractionated. To test the performance of our system, individual injections of the 50-, 100-, and 200-nm polystyrene particles were carried out; and the resultant retention time, peak shape and total particle quantification were compared with those obtained from injection of the mixture of

the 3 populations. The contour plots graphing the size, retention time, and particle concentration are displayed in Figure 2.10. No noticeable difference was found between the plots from injection of the mixed and single particle populations. The coefficient of variability (CV %) in particle quantification using the peak volume for each particle population was found to be below 5% (Table 2.1). These results support that, our system can perform reproducible particle counting from solutions containing pure or mixed particle populations.

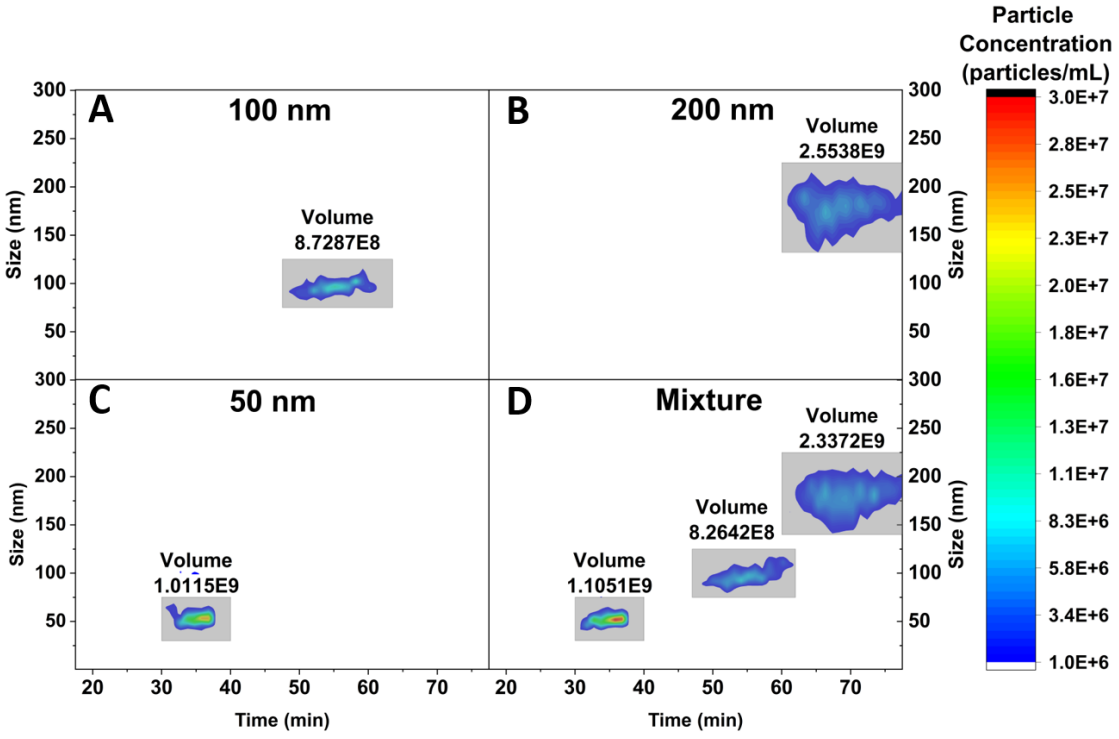

Figure 2.10 - Contour plots showing the single populations (A-C) and mixed population (D) injections. Quantification is taken as the volume under the curve. The gray box highlights the quantification region for each peak. For total quantification, the peak area was multiplied by the detector volumetric flow rate (0.5 mL/min).

Table 2.1 - Total particle recovery comparison between injections of mixed populations of beads versus injections of single size populations. CV: Coefficient of Variability

SIZE (NM)	PARTICLE COUNTS BY SINGLE INJECTION	PARTICLE COUNTS BY MIXTURE INJECTION	CV (%)
50	1.01×10^9	1.11×10^9	4.72
100	8.36×10^8	8.26×10^8	0.601
200	2.57×10^9	2.34×10^9	4.68

Next, we compared the performance of particle quantification between stand-alone NTA and AF4-NTA. Although the measurement by NTA alone displayed the presence of three particle populations when analyzing the equal molar mixture of the particles (Figure 2.11), size resolution in the histogram was poor and the intensities of the three peaks were not equal. Additionally, the peaks for the 50- and 100-nm particles were not reproducible, with the 50-nm particle population not always accurately determined due to the camera level settings: using the optimal camera level for detection of the 50-nm particles resulted in heavy optical flaring of the 200-nm particles, causing many of the 50- and 100-nm particles to be shielded from the camera by the bright flair.

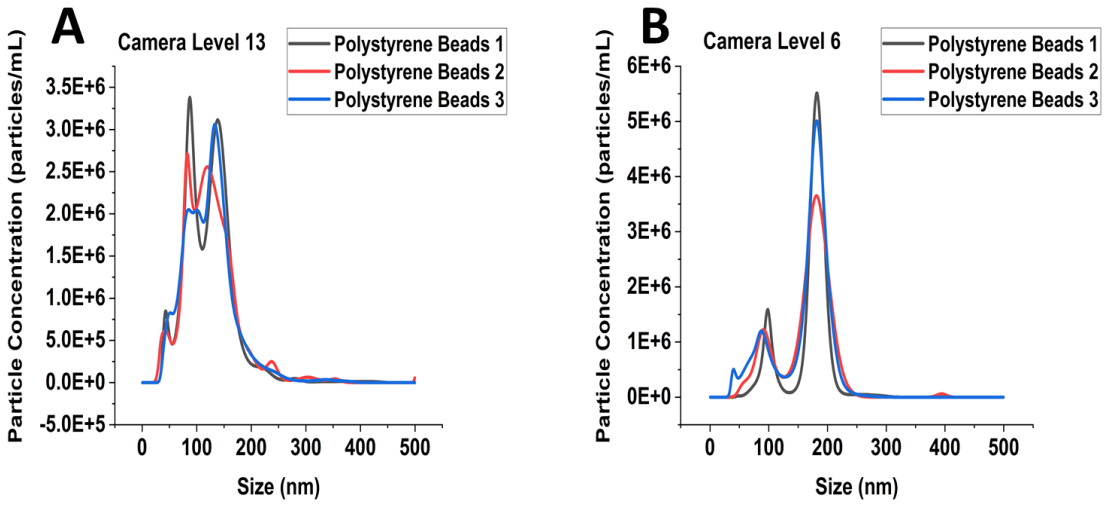

Figure 2.11 - Offline NTA of the PS bead mixture at the maximum and minimum camera levels used in the AF4-NTA separation. NTA is unable to accurately analyze the 3 populations due to the optical differences between the particles causing bias in the camera imaging.

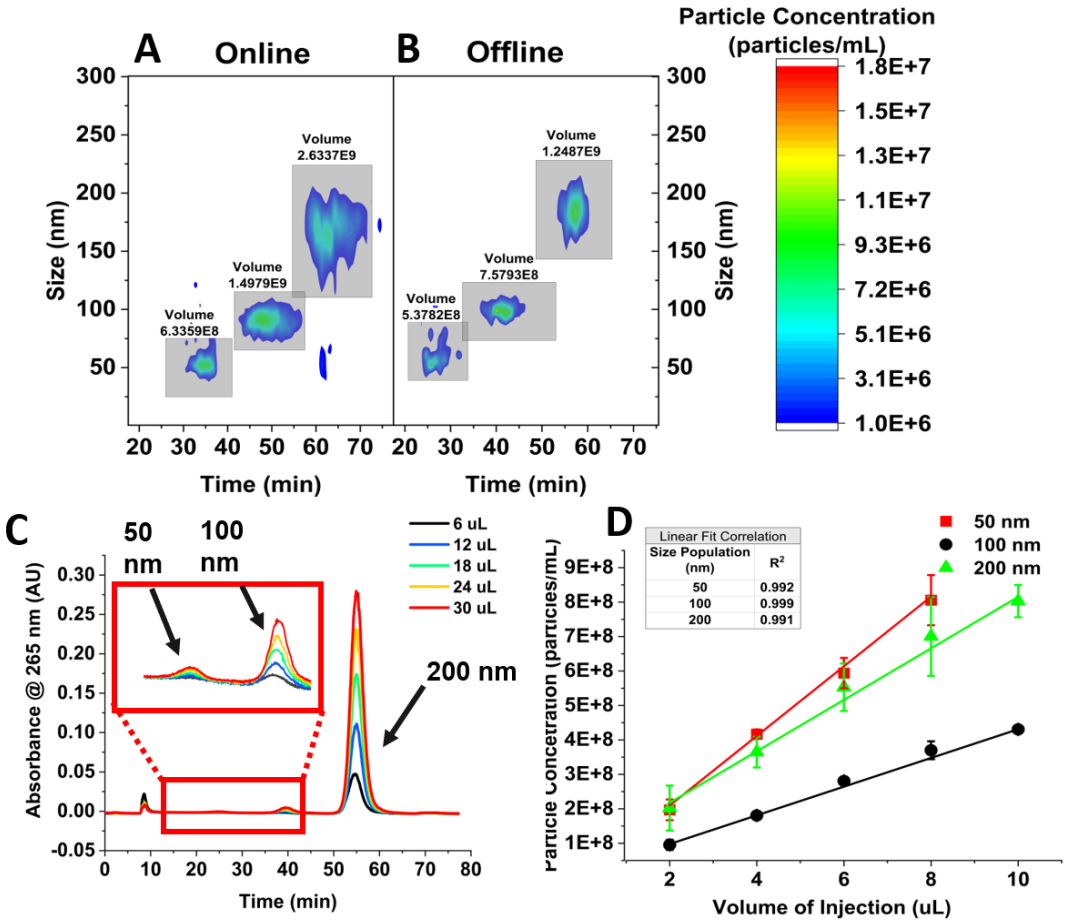

Figure 2.12 - Standard bead quantification tests. (A) Online NTA analysis and (B) offline NTA analysis of a 30 µL injection of a polystyrene bead mixture. (C) UV-Vis Absorbance and (D) NTA online quantification standard curve of increasing injection volumes of the polystyrene bead mixture.

On contrary, when the NTA was coupled to AF4, we were able to solve this issue by decreasing the NTA camera level during the separation process, since the smaller particles were eluted earlier than the larger particles. Three well-separated particle populations were then detected with both the size and concentration information obtained (online analysis, Figure 2.12A). We also collected the particles eluted after AF4 and measured them by NTA (offline analysis, Fig. 2.12B). The particle sizes and elution

windows measured by the online and the offline methods agreed well with each other, with some shifts in retention times due to the different flow rates between the ports of the NTA and FC. Another artifact of the different flow rates is band broadening in the online analysis due to the increased dead-volume. The current design uses a minimal amount of tubing to connect, but the manifold, the connectors, and the NTA channel all add up to approximately 100 µL in dead volume. Comparing the particle volumes shown in Fig. 2.12A and 2.12B, we could see the particle counts obtained with the off-line coupling method were lower, which is quite significant for the larger, 100- and 200-nm particles. This is probably due to particle absorption to the collection tube walls and syringe barrels that are needed to collect the AF4 eluent in the FC.

Additionally, we evaluated the accuracy of particle quantification using AF4-NTA by injecting different amounts (represented by injection volume) of the mixed polystyrene particles. The fractograms collected in the UV-Vis detector clearly showed increasing peak areas with increasing injection volumes (Fig. 2.12C). Agreeing well with the UV-Vis detection, NTA measurement also gave out linear ($R^2 > 0.99$) increase in the detected particle concentration with increasing injection volume.

The results shown in Fig. 2.12C & 2.12D also illustrates the increased sensitivity of NTA compared to the UV-Vis detector in particle detection. With UV-Vis detection, the larger particles can absorb more light than the smaller ones, and thus have better detectability. On contrary, NTA allows all particles to be measured which provides an unbiased counting instead of calculations derived from bulk analysis like light adsorption techniques. The limit of detection (LOD) of the 200-nm, 100-nm and 50-nm particles by

UV-Vis detection was 3.51×10^7, 5.47×10^6, and 4.07×10^7, respectively. Using the AF4-NTA system, the LOD for the 200-nm, 100-nm, and 50-nm particles were 2.84×10^8, 5.19×10^6, and 1.37×10^7, respectively. The LOD is lower for UV-VIS than AF4-NTA when analyzing the 200-nm particles, but comparable or higher for the smaller ones. NTA calculates particle concentration by taking a simple average of the particles visible per frame, which is converted to a particle per volume of viewing area (exact volume unknown but estimated to be ~20 nL). The system then converts that count to a particle concentration that represents the larger solution. This small to large volume concentration conversion limits the LOD and LOQ obtained with NTA because one particle on screen could represent 1×10^5 to 1×10^6 particles in solution. Additionally, with NTA, particle concentration can be obtained directly, but with the bulk optical methods, the conversion constants such as extinction coefficient would need to be known before the actual particle molar concentration can be determined. Moreover, with NTA providing measurement on sizes, even if the particles of different sizes were not well separated in AF4, size resolution could be improved by connecting it to NTA. Smaller particles that are co-eluted with the larger particle populations can be easily recognized in the 3D contour plot.

2.4 - Conclusion

A hyphenated system of particle separation by AF4 and sizing by NTA has been developed in the present work for rapid and accurate nanoparticle quantification and characterization. Because AF4 can separate diverse types of analytes falling within a wide size based on their hydrodynamic diameters, this coupling provides a versatile nanoparticle characterization system that also allows collection of separated particle populations for

further characterization. Flow rate was shown to be important to the analytical accuracy of the instrument, and a reduction in channel pressure was needed to protect the NTA channel from damage or leaks. The relative simplicity and straightforward nature of the setup and data collection process improves the speed at which this data can be collected and analyzed, generally being able to get quantification data in not much longer than the time a separation would take. NTA has some limitations as an online detector, such as its narrow working range, low flow rates, low pressure thresholds, and a dependence on optimal detector settings, but the added simplicity, efficiency, and unbiased particle counting make NTA an efficient online detector that could be coupled to any fluidic system where pressure and flow rates can be specifically controlled.

2.5 - References

(1) Mohammad, F.; Al-Lohedan, H. A. Toxicity Assessment of Engineered Mn–ZnS Quantum Dots in Vitro. *J. Mater. Sci.* **2016**, *51* (20), 9207–9216. https://doi.org/10.1007/s10853-016-0149-4.

(2) Khan, I.; Saeed, K.; Khan, I. Nanoparticles: Properties, Applications and Toxicities. *Arabian Journal of Chemistry*. Elsevier B.V. November 1, 2019, pp 908–931. https://doi.org/10.1016/j.arabjc.2017.05.011.

(3) Orecna, M.; De Paoli, S. H.; Janouskova, O.; Tegegn, T. Z.; Filipova, M.; Bonevich, J. E.; Holada, K.; Simak, J. Toxicity of Carboxylated Carbon Nanotubes in Endothelial Cells Is Attenuated by Stimulation of the Autophagic Flux with the Release of Nanomaterial in Autophagic Vesicles. *Nanomedicine Nanotechnol. Biol. Med.* **2014**, *10* (5), 939–948. https://doi.org/10.1016/j.nano.2014.02.001.

(4) Puster, M.; Rodríguez-Manzo, J. A.; Balan, A.; Drndić, M. Toward Sensitive Graphene Nanoribbon–Nanopore Devices by Preventing Electron Beam-Induced Damage. *ACS Nano* **2013**, *7* (12), 11283–11289. https://doi.org/10.1021/nn405112m.

(5) Xiao, A.; Wang, C.; Chen, J.; Guo, R.; Yan, Z.; Chen, J. Carbon and Metal Quantum Dots Toxicity on the Microalgae Chlorella Pyrenoidosa. *Ecotoxicol. Environ. Saf.* **2016**, *133*, 211–217. https://doi.org/10.1016/j.ecoenv.2016.07.026.

(6) Bahadar, H.; Maqbool, F.; Niaz, K.; Abdollahi, M. Toxicity of Nanoparticles and an Overview of Current Experimental Models. *Iranian Biomedical Journal*. Pasteur Institute of Iran January 1, 2016, pp 1–11. https://doi.org/10.7508/ibj.2016.01.001.

(7) Bowman, D. M.; van Calster, G.; Friedrichs, S. Nanomaterials and Regulation of Cosmetics. *Nat. Nanotechnol.* **2010**, *5* (2), 92–92. https://doi.org/10.1038/nnano.2010.12.

(8) Contado, C. Nanomaterials in Consumer Products: A Challenging Analytical Problem. *Front. Chem.* **2015**, *3*, 48. https://doi.org/10.3389/fchem.2015.00048.

(9) Office of Cosmetics and Colors. Guidance for Industry: Safety of Nanomaterials in Cosmetic Products | FDA https://www.fda.gov/regulatory-information/search-fda-guidance-documents/guidance-industry-safety-nanomaterials-cosmetic-products#IIIB1 (accessed 2019 -12 -19).

(10) Rice, S. B.; Chan, C.; Brown, S. C.; Eschbach, P.; Han, L.; Ensor, D. S.; Stefaniak, A. B.; Bonevich, J.; Vladár, A. E.; Walker, A. R. H.; Zheng, J.; Starnes, C.;

Stromberg, A.; Ye, J.; Grulke, E. A. Particle Size Distributions by Transmission Electron Microscopy: An Interlaboratory Comparison Case Study. *Metrologia* **2013**, *50* (6), 663–678. https://doi.org/10.1088/0026-1394/50/6/663.

(11) Gwaze, P.; Annegarn, H. J.; Huth, J.; Helas, G. Comparison of Particle Sizes Determined with Impactor, AFM and SEM. *Atmospheric Res.* **2007**, *86* (2), 93–104. https://doi.org/10.1016/j.atmosres.2007.02.009.

(12) Barcikowski, S.; Hahn, A.; Kabashin, A. V.; Chichkov, B. N. Properties of Nanoparticles Generated during Femtosecond Laser Machining in Air and Water. *Appl. Phys. Mater. Sci. Process.* **2007**, *87* (1), 47–55. https://doi.org/10.1007/s00339-006-3852-1.

(13) Maas, S. L. N.; de Vrij, J.; van der Vlist, E. J.; Geragousian, B.; van Bloois, L.; Mastrobattista, E.; Schiffelers, R. M.; Wauben, M. H. M.; Broekman, M. L. D.; Nolte-'t Hoen, E. N. M. Possibilities and Limitations of Current Technologies for Quantification of Biological Extracellular Vesicles and Synthetic Mimics. *J. Control. Release Off. J. Control. Release Soc.* **2015**, *200*, 87–96. https://doi.org/10.1016/j.jconrel.2014.12.041.

(14) Vaclavek, T.; Prikryl, J.; Foret, F. Resistive Pulse Sensing as Particle Counting and Sizing Method in Microfluidic Systems: Designs and Applications Review. *J. Sep. Sci.* **2019**, *42* (1), 445–457. https://doi.org/10.1002/jssc.201800978.

(15) Carr, B.; Malloy, A. NanoParticle Tracking Analysis – The NANOSIGHT System. 8.

(16) Filipe, V.; Hawe, A.; Jiskoot, W. Critical Evaluation of Nanoparticle Tracking Analysis (NTA) by NanoSight for the Measurement of Nanoparticles and Protein Aggregates. *Pharm. Res.* **2010**, *27* (5), 796–810. https://doi.org/10.1007/s11095-010-0073-2.

(17) Carr, B.; Malloy, A. NanoParticle Tracking Analysis – The NANOSIGHT System.

(18) van der Pol, E.; Coumans, F. A. W.; Grootemaat, A. E.; Gardiner, C.; Sargent, I. L.; Harrison, P.; Sturk, A.; van Leeuwen, T. G.; Nieuwland, R. Particle Size Distribution of Exosomes and Microvesicles Determined by Transmission Electron Microscopy, Flow Cytometry, Nanoparticle Tracking Analysis, and Resistive Pulse Sensing. *J. Thromb. Haemost.* **2014**, *12* (7), 1182–1192. https://doi.org/10.1111/jth.12602.

(19) De Benedetto, G.; Cescutti, P.; Giannelli, C.; Rizzo, R.; Micoli, F. Multiple Techniques for Size Determination of Generalized Modules for Membrane Antigens from Salmonella Typhimurium and Salmonella Enteritidis. *ACS Omega* **2017**, *2* (11), 8282–8289. https://doi.org/10.1021/acsomega.7b01173.

(20) Makan, A. C.; Spallek, M. J.; du Toit, M.; Klein, T.; Pasch, H. Advanced Analysis of Polymer Emulsions: Particle Size and Particle Size Distribution by Field-Flow Fractionation and Dynamic Light Scattering. *J. Chromatogr. A* **2016**, *1442*, 94–106. https://doi.org/10.1016/j.chroma.2016.03.013.

(21) Battistini, B.; Petrucci, F.; Bocca, B. In-House Validation of AF4-MALS-UV for Polystyrene Nanoplastic Analysis. *Anal. Bioanal. Chem.* **2021**, *413* (11), 3027–3039. https://doi.org/10.1007/s00216-021-03238-2.

(22) Rübsam, H.; Becker, T.; Gastl, M. Analytical Characterization of the Hydrolysis of Barley Malt Macromolecules During Enzymatic Degradation Over Time Using AF4/MALS/RI. *J. Food Sci.* **2017**, *82* (6), 1326–1332. https://doi.org/10.1111/1750-3841.13716.

(23) Fuentes, C.; Castillo, J.; Vila, J.; Nilsson, L. Application of Asymmetric Flow Field-Flow Fractionation (AF4) and Multiangle Light Scattering (MALS) for the Evaluation of Changes in the Product Molar Mass during PVP-b-PAMPS Synthesis. *Anal. Bioanal. Chem.* **2018**, *410* (16), 3757–3767. https://doi.org/10.1007/s00216-018-1039-1.

(24) Asymmetric Flow Field-Flow Fractionation with Multiangle Light Scattering Detection for Characterization of Cellulose Nanocrystals | Biomacromolecules https://pubs.acs.org/doi/abs/10.1021/bm300595a (accessed 2021 -07 -31).

(25) Écija-Arenas, Á.; Román-Pizarro, V.; Fernández-Romero, J. M. Separation and Characterization of Liposomes Using Asymmetric Flow Field-Flow Fractionation with Online Multi-Angle Light Scattering Detection. *J. Chromatogr. A* **2021**, *1636*, 461798. https://doi.org/10.1016/j.chroma.2020.461798.

(26) Ansar, S. M.; Mudalige, T. Characterization of Doxorubicin Liposomal Formulations for Size-Based Distribution of Drug and Excipients Using Asymmetric-Flow Field-Flow Fractionation (AF4) and Liquid Chromatography-Mass Spectrometry (LC-MS). *Int. J. Pharm.* **2020**, *574*, 118906. https://doi.org/10.1016/j.ijpharm.2019.118906.

(27) Kuklenyik, Z.; Gardner, M.; Parks, B.; Schieltz, D.; Rees, J.; McWilliams, L.; Williamson, Y.; Pirkle, J.; Barr, J. Multivariate DoE Optimization of Asymmetric Flow Field Flow Fractionation Coupled to Quantitative LC-MS/MS for Analysis of Lipoprotein Subclasses. *Chromatography* **2015**, *2* (1), 96–117. https://doi.org/10.3390/chromatography2010096.

(28) Kuklenyik, Z.; Jones, J. I.; Gardner, M. S.; Schieltz, D. M.; Parks, B. A.; Toth, C. A.; Rees, J. C.; Andrews, M. L.; Carter, K.; Lehtikoski, A. K.; McWilliams, L. G.; Williamson, Y. M.; Bierbaum, K. P.; Pirkle, J. L.; Barr, J. R. Core Lipid, Surface Lipid and Apolipoprotein Composition Analysis of Lipoprotein Particles as a

Function of Particle Size in One Workflow Integrating Asymmetric Flow Field-Flow Fractionation and Liquid Chromatography-Tandem Mass Spectrometry. *PLOS ONE* **2018**, *13* (4), e0194797. https://doi.org/10.1371/journal.pone.0194797.

(29) Hetzer, B.; Burcza, A.; Gräf, V.; Walz, E.; Greiner, R. Online-Coupling of AF4 and Single Particle-ICP-MS as an Analytical Approach for the Selective Detection of Nanosilver Release from Model Food Packaging Films into Food Simulants. *Food Control* **2017**, *80*, 113–124. https://doi.org/10.1016/j.foodcont.2017.04.040.

(30) López-Sanz, S.; Fariñas, N. R.; Martín-Doimeadios, R. del C. R.; Ríos, Á. Analytical Strategy Based on Asymmetric Flow Field Flow Fractionation Hyphenated to ICP-MS and Complementary Techniques to Study Gold Nanoparticles Transformations in Cell Culture Medium. *Anal. Chim. Acta* **2019**, *1053*, 178–185. https://doi.org/10.1016/j.aca.2018.11.053.

(31) Ojeda, D.; Taboada-López, M. V.; Bolea, E.; Pérez-Arantegui, J.; Bermejo-Barrera, P.; Moreda-Piñeiro, A.; Laborda, F. Size Characterization and Quantification of Titanium Dioxide Nano- and Microparticles-Based Products by Asymmetrical Flow Field-Flow Fractionation Coupled to Dynamic Light Scattering and Inductively Coupled Plasma Mass Spectrometry. *Anal. Chim. Acta* **2020**, *1122*, 20–30. https://doi.org/10.1016/j.aca.2020.04.080.

(32) Schmidt, B.; Loeschner, K.; Hadrup, N.; Mortensen, A.; Sloth, J. J.; Koch, C. B.; Larsen, E. H. Quantitative Characterization of Gold Nanoparticles by Field-Flow Fractionation Coupled Online with Light Scattering Detection and Inductively Coupled Plasma Mass Spectrometry. *Anal. Chem.* **2011**, *83* (7), 2461–2468. https://doi.org/10.1021/ac102545e.

(33) Sötebier, C. A.; Bierkandt, F. S.; Rades, S.; Jakubowski, N.; Panne, U.; Weidner, S. M. Sample Loss in Asymmetric Flow Field-Flow Fractionation Coupled to Inductively Coupled Plasma-Mass Spectrometry of Silver Nanoparticles. *J. Anal. At. Spectrom.* **2015**, *30* (10), 2214–2222. https://doi.org/10.1039/C5JA00297D.

(34) Galazzi, R. M.; Chacón-Madrid, K.; Freitas, D. C.; Costa, L. F.; Arruda, M. A. Z. Inductively Coupled Plasma Mass Spectrometry-based Platforms for Studies Involving Nanoparticles Effects in Biological Samples. *Rapid Commun. Mass Spectrom.* **2020**. https://doi.org/10.1002/rcm.8726.

(35) Schwaferts, C.; Sogne, V.; Welz, R.; Meier, F.; Klein, T.; Niessner, R.; Elsner, M.; Ivleva, N. P. Nanoplastic Analysis by Online Coupling of Raman Microscopy and Field-Flow Fractionation Enabled by Optical Tweezers. *Anal. Chem.* **2020**, *92* (8), 5813–5820. https://doi.org/10.1021/acs.analchem.9b05336.

(36) Bello-Perez, L. A.; Agama-Acevedo, E.; Lopez-Silva, M.; Alvarez-Ramirez, J. Molecular Characterization of Corn Starches by HPSEC-MALS-RI: A Comparison

with AF4-MALS-RI System. *Food Hydrocoll.* **2019**, *96*, 373–376. https://doi.org/10.1016/j.foodhyd.2019.04.067.

(37) Duan, Y.; Coreas, R.; Liu, Y.; Bitounis, D.; Zhang, Z.; Parviz, D.; Strano, M.; Demokritou, P.; Zhong, W. Prediction of Protein Corona on Nanomaterials by Machine Learning Using Novel Descriptors. *NanoImpact* **2020**, 100207. https://doi.org/10.1016/j.impact.2020.100207.

Chapter 3: AF4-NTA for the Isolation and Characterization of Non-Spherical and Soft Nanomaterials in Complex Matrices

This chapter aims to explore materials that are non-ideal as further exploration of the broad applicability of AF4-NTA.

3.1 - Introduction

AF4 is quite versatile and has been employed in NP analysis of different morphologies, sizes, and compositions .[1–11] AF4 has been used in gentle separations of proteins, exosomes, microvesicles, and lipid nanostructures for biotechnology and research applications.[3,4,9,12–20] Our lab has used AF4 to separate NPs from proteins for corona analysis as well as developed a SELEX method using AF4 to enrich a high affinity aptamer for DNMT1.[21–24] Offline NTA analysis of extracellular vesicles has been well established and AF4-NTA seems very applicable in biological sample analysis of biocorona formation and exosome characterization.[25–30] It is reasonable to assume AF4-NTA would be as capable if not more suited for the analysis of biocorona thickness, and the isolation and characterization of exosomes and BioNPs.

Morphology plays an important role in NP design and function. It is common to alter the synthesis conditions to shape or modify the surface in ways that enhance its properties.[31–37] When a NP is sized by NTA, to simplify data analysis, the software assumes all particles are spherical,[38] and uses the Stokes Einstein equation (1) to determine the hydrodynamic diameter from the diffusion coefficient:

$$D = \frac{k_B T}{3\pi\eta d_h} \quad (2)$$

Where D is the self-diffusion coefficient (commonly known as just the diffusion coefficient), k_B is the Boltzmann constant, T is temperature, η is viscosity, and d_h is the hydrodynamic diameter. For a non-spherical shape, the relation between diffusion coefficient and hydrodynamic diameter changes to this equation:

$$D = \frac{k_B T}{3\pi\eta L} F_d \tag{2}$$

Where L is the length of the major axis and F_d is a geometrical coefficient. [39] Substituting Eqn (2) for D into Eqn (1) simplifies to:

$$L = d_h F_d \tag{3}$$

$$F_d = \frac{L}{d_h} \tag{4}$$

The geometric coefficient is a conversion factor between the major axis length and the hydrodynamic diameter measured by NTA, which assumes an ideal sphere. Using the value of L found from TEM measurement or from the supplier's certificate of authentication (COA) for a series of nanorod standards, it is possible to obtain the value of F_d from the d_h found by NTA.

Thus, it is attractive to employ AF4-NTA to separate non-spherical NPs and measure their dimensions. First, two different gold nanorods (AuNRs) of similar widths and differing lengths will be analyzed by online and offline NTA to see the ability to differentiate different populations and to determine the F_d value for two different AuNRs. Secondly, analysis of two-dimensional hexagonal boronitride (hBN) flakes were done

proving the capability of AF4-NTA in analyzing two-dimensional nanomaterials. In addition to non-spherical NPs, AF4-NTA was employed to evaluate the biocorona of hBN, and to measure standard exosomes and exosomes isolated from pooled single donor human serum using the AF4 size separation.

3.2 - Methodology

3.2.1 - Materials

NanoXact gold nanorods with dimensions of 45.5×17.3 nm (Cat # GRCN660-25M) and 69.3×12.0 nm (Cat# GRCN980-10M) were purchased from nanoComposix. The 2D nanomaterial of hexagonal boron nitride (hBN) with the average lateral dimension around 150 nm and layer thickness < 10 nm was obtained from the Harvard HSPH-HIEHS Nanosafety Center. The detailed characterization was reported in our previous work.[40] Fetal bovine serum (FBS) (Cat# 1043702), and Dulbecco′s Modified Eagle′s Medium, high glucose (DMEM) (Cat# 11965092) were purchased from Thermo Fisher. Single Donor Human Serum Off the Clot samples were purchased from Innovative Research (Cat# ISERS2ML). Supplemented medium was made by diluting to 10% FBS with DMEM. FL-70 (Cat# SF1051) and sodium azide (Cat# 190381000) were purchased from Fisher Scientific. 10× PBS (Cat# PBS01-03) was purchased premixed from Bioland and diluted to 1× and filtered daily. Exosome standards (Cat# HBM-COLO-100/2) were purchased from Galen Laboratory Supply and diluted to 100 µg/mL before being frozen for long term storage.

3.2.2 - AF4-NTA Coupling

The system was connected as defined by our previous work.[41] Briefly, a syringe pump is connected to the exit port of NTA with a multi-port flow splitter manifold attached to the input of the system. A total of 2 identical length lines were ran from the splitter to the fraction collector while the 3rd line was connected to the NTA channel. The remaining ports were closed off by plugs. A withdrawal flow rate of 15 μL/min was set in the Syringe Pump Pro software and the system was allowed to equilibrate until an accurate and smooth flow rate was achieved.

3.2.3 - AF4 Method

AF4 was performed with a 10 kDa regenerated cellulose with a 350 μm spacer with an analytical scale channel. All nanomaterials were separated in 0.02% NaN_3 with 0.1% FL-70 except for hBN, which was separated in 1× PBS with 0.1% FL-70 and 0.02% NaN_3. UV-Vis was taken at 265 nm with a Shimadzu SPD 10a detector. The crossflow program starts with focus, tip, and cross flows of 2.95, 0.30, and 2.75 ml/min, respectively, to focus the sample in a narrow band at the top of the channel. A focus time of 7 minutes was used to ensure the particles start in a tight band before separation. At the start of separation, the crossflow switches to 1.25 mL/min while the focus flow is turned off and the crossflow is linearly decayed to 0.10 mL/min over 50 minutes. The 0.10 mL/min is maintained for another 10 minutes until the end of the run. Figure 3.1 shows the complete cross flow method used for the isolations in this study.

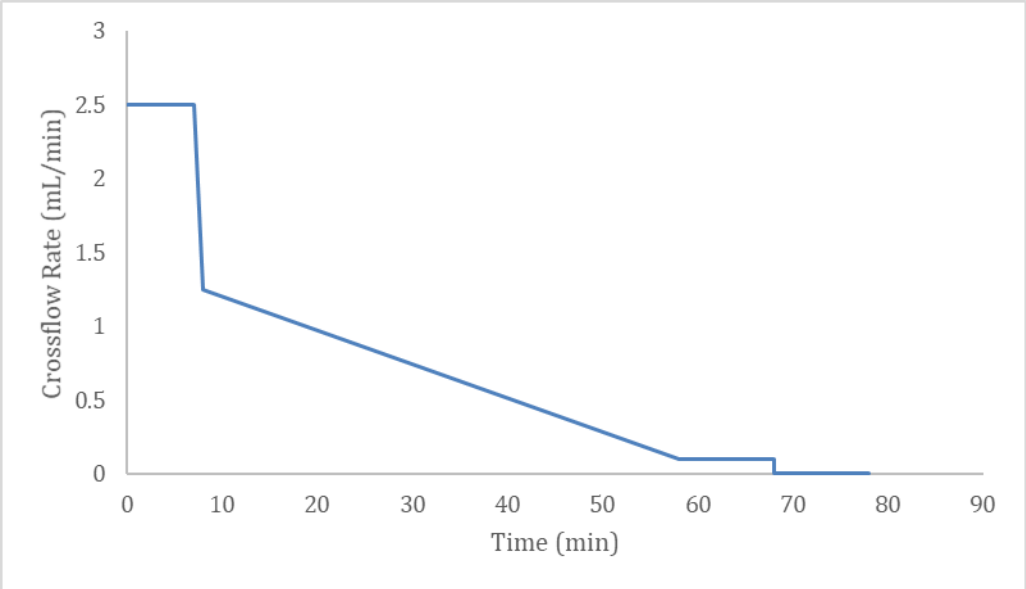

Figure 3.1 - Graphical display of the AF4 method.

3.2.4 - NTA Method

NTA scripting was setup according to our previous work.[41] The script produces a series 1 minute videos that correspond to 1 minute of elution into a fraction collector. Each fraction's distribution is stacked in a matrix in Origin Pro software, creating a 3D histogram with time on the x-axis, size on the y-axis, and particle concentration on the z-axis. By applying the integrate tool to the 3D plot, a peak volume is obtained, which contains the volumetric particle concentration. The peak volume unit is ($\frac{particles*min*nm}{mL}$) and reduces to ($particles * nm$) when multiplying the concentration by the detector flow rate ($\frac{mL}{min}$), which is the definition of a number distribution.

3.2.5 - Sample Preparation

Different preparations are needed depending on the type of analysis. Different AuNRs are used as a standard rod material of different lengths and were prepared the same.

Each sample was sonicated in a cone sonicator for 2 minutes with 50% power using a 2 sec on and 2 sec off cycling to avoid excessive overheating. After sonication, the sample was diluted in AF4 running buffer to 1 mg/mL and 25 µL injections of AuNRs separated using the AF4 method shown in Figure 1.

For protein corona analysis, the hBN sample was prepared by pelleting at speeds of 20,000 ×g for 10 minutes. Redispersion buffer was added to the pellet and vortexed for 30 seconds to disperse the pellet. The dispersed sample was then sonicated for 2 minutes at 50% power with a 2 s on 2 s off pulse cycle. The dispersion buffer was either DMEM or DMEM with 10% FBS. The sample was allowed to incubate for 5 minutes and then injected into the system. Each sample was prepared directly before injection to maintain similar incubation times after dispersion. The final mass concentration per sample was 25 µg/mL of hBN regardless of the dispersion buffer. The final injection of 200 µL of sample incorporated 5 µg of hBN per separation.

Exosome standards were diluted to 10× with 1× PBS with 0.1% FL-70 and ran in AF4 with the same running buffer. Three healthy patient human serum samples were purchased, pooled, aliquoted, and stored at -80°C until the day before analysis. Serum samples were thawed overnight at 4°C before injection. Serum samples were spun at 20,000 ×g before analysis to remove debris and larger macrovesicles. 25 µL of pooled healthy serum was injected while 2.5 and 10.0 µg of exosome standards were injected.

3.3 - Results and Discussion

3.3.1 - AuNRs

Figure 3.2 shows the results of the NTA and AF4-NTA data of the AuNRs. The mixture of AuNRs was ran in offline NTA a total of 3 times and only one of the trials showed two populations, as evident in (A) of Figure 3.2. The small difference in nanorod size causes peak overlap and causes broad single peaks in two of the trials. Table 3.1 shows the calculations of the geometrical coefficient, surface area, aspect ratio, and mass per particle of the AuNRs using online and offline NTA. The F_d value is different for each rod because each rod has a different width and length. The F_d shows a stronger relation to the mass to surface area ratio than the aspect ratio of the material. These F_d values can be used to convert the measured hydrodynamic diameter of the rod to the rod length but is unable to determine the width of the NP.

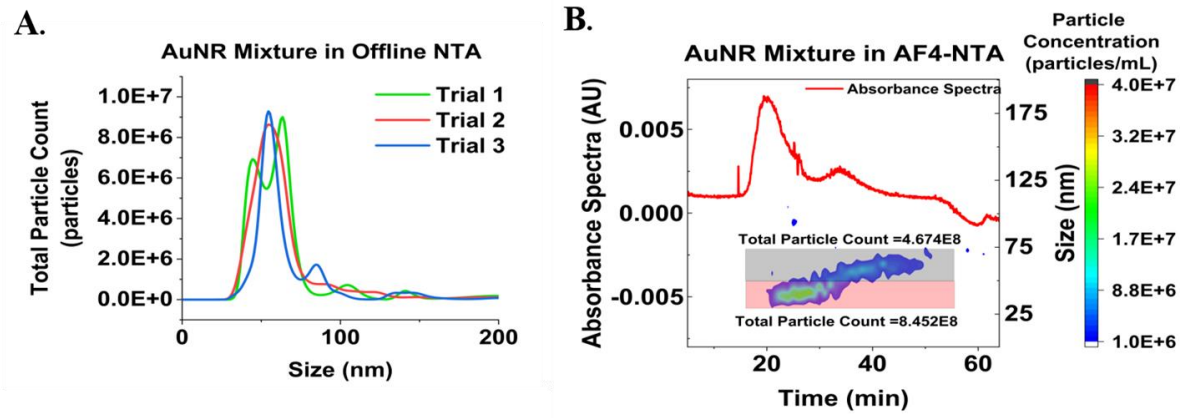

Figure 3.2 - Offline and online NTA results of the two AuNRs populations. Offline NTA cannot resolve two populations but in combination with AF4 it is quite visible.

Table 3.1 - AuNR COA, offline and online NTA data and analysis. The geometric coefficient is a calculation using the COA value for the major axis and the hydrodynamic diameter determined by NTA.

Particle Counts per 10 µL of Stock						
AuNR Size	**COA**	**Offline NTA**	**AF4-NTA**	**Error % Between COA and Offline**	**Error % Between COA and Online**	**Error % Between Online and Offline**
(nm)	**(Particles)**	**(Particles)**	**(Particles)**	**(%)**	**(%)**	**(%)**
45.5×17.3	**2.36E+09**	**3.66E+08**	**8.45E+08**	**84.49**	**64.19**	**130.87**
69.3×12.0	**1.40E+09**	**2.29E+08**	**4.78E+08**	**83.64**	**65.86**	**108.73**

Size Information						
AuNR Size	**COA DH Size Mode**	**Offline NTA Size Mode**	**AF4-NTA Size Mode**	**Width (TEM)**	**Length (TEM)**	**Aspect Ratio**
(nm)	**(nm)**	**(nm)**	**(nm)**	**(nm)**	**(nm)**	**(L/W)**
45.5×17.3	**13**	**43**	**42.5**	**17.4**	**45.5**	**2.61**
69.3×12.0	**19**	**55.7**	**57.5**	**12**	**69.3**	**5.78**

Geometric Coefficient Calculation						
AuNR Size	**Fd by Offline NTA**	**Fd by Online NTA**	**Mass of Sample**	**Mass per Particle**	**Average Surface Area of Particle**	**Mass per Surface Area**
(nm)	**(L/dh)**	**(L/dh)**	**(mg/mL)**	**(mg/particle)**	**(nm^3)**	**(mg/(particle*nm^3))**
45.5×17.3	**1.06**	**1.07**	**0.31**	**1.31E-10**	**10819.3**	**1.21E-14**
69.3×12.0	**1.24**	**1.21**	**0.18**	**1.29E-10**	**7837.6**	**1.64E-14**

There are noticeable discrepancies between the particle concentration and hydrodynamic size values obtained by NTA, AF4-NTA, and those provided by the manufacturer COA. The COA particle concentration is calculated based on the mass concentration measured by ICP-MS and the volume and density of the AuNRs; thus, it is

understandable that it could vary from that obtained by NTA through counting individual particles. On the other hand, the difference in particle size is quite large, with the COA values being 13 - 15 nm, which is much smaller than the 43 nm reported in NTA. This is because the COA value is determined by DLS, which uses a different approach to measure particle size than NTA.[42,43] While both instruments calculate particle size using the Stokes Einstein equation from diffusion coefficient (*D*), DLS acquires *D* via the time dependent scattering intensity fluctuation,[42,43] while NTA determines *D* by MSD.[30,44] Their different mechanisms in *D* determination induce relatively larger deviation in measuring the dimension of non-spherical particles like NRs compared to spherical ones.[45,46] It also has been shown by Žagar and Pahovnik et al. that DLS underestimates the size of particles in batch mode as well as flow mode, especially in larger-diameter particles.[47] Interestingly, DLS should be more capable than NTA because DLS measures the translational diffusion coefficient while NTA only obtains the self-diffusion coefficient from the MSD.[48] Similar in assumptions, DLS assumes all particles are spherical and assumes $D_T = D$, meaning the major axis is the same in all directions similar when F_d is equal to 1. According to Tirado and Garcia de la Torre et al., the DLS relation to rod dimensions and the Stokes-Einstein is:

$$D_t = \frac{k_B T}{3\pi\eta L}\left(\ln\frac{L}{d} + v\right) \quad (6)$$

Where *L* is the rod (major axis) length and *d* is the width of the rod. *v* is the end correction which has been experimentally determined for rods between certain aspect ratios by Tirado and Garcia de la Torre et al.[49] This relation assumes $D_t = D$ when calculating the

hydrodynamic radius in DLS. The MSD determined self-diffusion coefficient is the sum average of D_t and D_R by this equation:

$$D = \frac{(D_T + D_R)}{2} \tag{7}$$

NTA measures D while DLS measures D_T. If we assumed $D_t = D$, we could relate F_d to the DLS relation to a rod shape and be left with:

$$F_d = \ln \frac{L}{d} + v \tag{8}$$

It would be a fallacy to apply Eqn 8 to the F_d values determined by this experiment to calculate the nanorod width simply because $D_t \neq D$ when the shape is non-spherical, however it would be possible if D_T or D_R were known, and D could be converted into D_T with Eqn 7. It may be possible to use Eqn 7 to estimate an aspect ratio, but a more extensive study is needed with many different aspect ratios and sizes of nanorods to establish if any assumptions can be applied. No direct trend was observed in the data presented here.

NTA showed a lower particle concentration than the suppliers COA, but this could be due to stock aging and some loss of NPs to adsorption to the container wall. Offline NTA was unable to directly quantify a mixture of both species so the quantity was determined in offline NTA with single specie solutions. Online versus offline showed an increased particle count with AF4-NTA (130.87% and 108.73% increase in particles measured) compared to offline NTA, but this was done as a mixture and done with a non-ideal separation to show how the AF4-NTA combination can differentiate populations even if the poor resolution of AF4 causes peak overlap. One possibility that cannot be excluded is the smaller rod population could have dimers that overlap the larger rod peak. A better separation could help resolve the issue but the size difference between these two rods is

small and baseline separation would be difficult if not impossible. Another possible reason for the increase in counts is the addition of background particles from the AF4 channel or band broadening affects that may have caused discrepancies in the previous chapter. The previous work has also shown that a separation field before NTA allows the smaller sizes to be seen more easily since they are not shielded by the larger particles being measured when a mixture is measured simultaneously. This seems to cause consistently higher particle counts with online NTA when compared to offline NTA. Even though the total quantification is difficult to validate, the relative amounts still match with the injected volumes and expected ratios.

3.3.2 - hBN and protein corona formation on hBN

Analysis of 500 ng/mL hBN solution by standalone NTA exhibited a size distribution covering 50-100 nm (Figure 3A). In AF4-NTA, the separation showed a wide elution window from 15-45 minutes (Figure 3B). Summing the particle numbers detected over the entire separation course yields the true number distribution of the 5 µg hBN stock solution. Since 1 µL stock solution was used in the diluted stand-alone NTA sample and 10 µL was used for AF4-NTA, the particles were normalized to 1 µL of hBN stock solution by dividing the total particle count by 10. Interestingly, the AF4-NTA was able to measure more of the smaller particles within the size range of 30-50 nm compared to stand-alone NTA. This indicates a better ability to distinguish the true distribution because smaller particles may be masked by brighter particles in the viewing window when a mixture of populations are present.

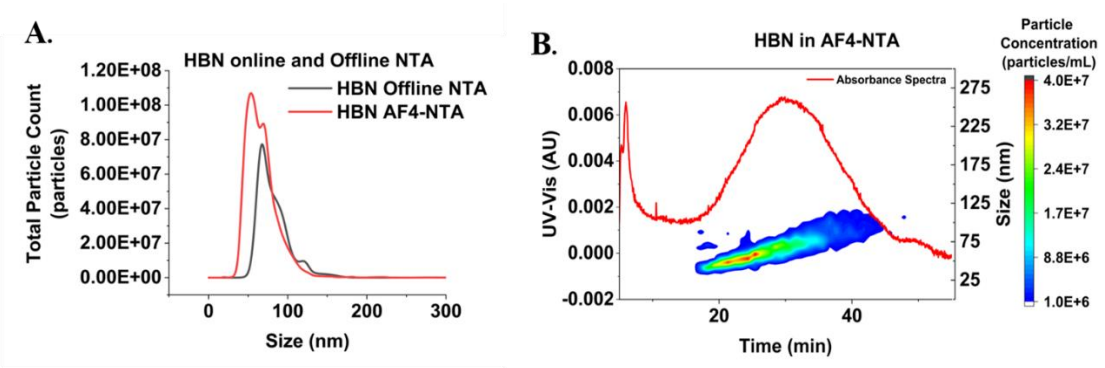

Figure 3.3 - Offline (A) and Online (B) NTA comparison of 5 µg stock hBN. The online NTA shown in A is a 2D sum of the plot in (B)

A protein corona was formed on the surface of hBN before AF4-NTA analysis to test and observe the corona formation. The stock material in Figure 3.4C showed a similar distribution to Figure 3.3B when the online and offline results were compared. The diluent medium was used as a control for background particles and the total particles are quantified in Figure 3.4A. The plots use a baseline of 1.00E+06 to make them visually appealing and easier to see, but for quantification there is no baseline selected. Lighter density NPs like proteins and vesicles do not scatter light as intensely as metal oxide NPs and require much higher camera levels to be detected by NTA, usually 10 or higher. hBN was very bright at camera level 7 and below and most of the background particles are not detected at these lower camera levels. Background particles that were detected were quantified and shown to be 6.41E+08 particles (Figure 3.4A). This run was performed after conditioning the membrane with multiple serum runs to block the membrane of any adsorption sites before performing quantitative analysis.

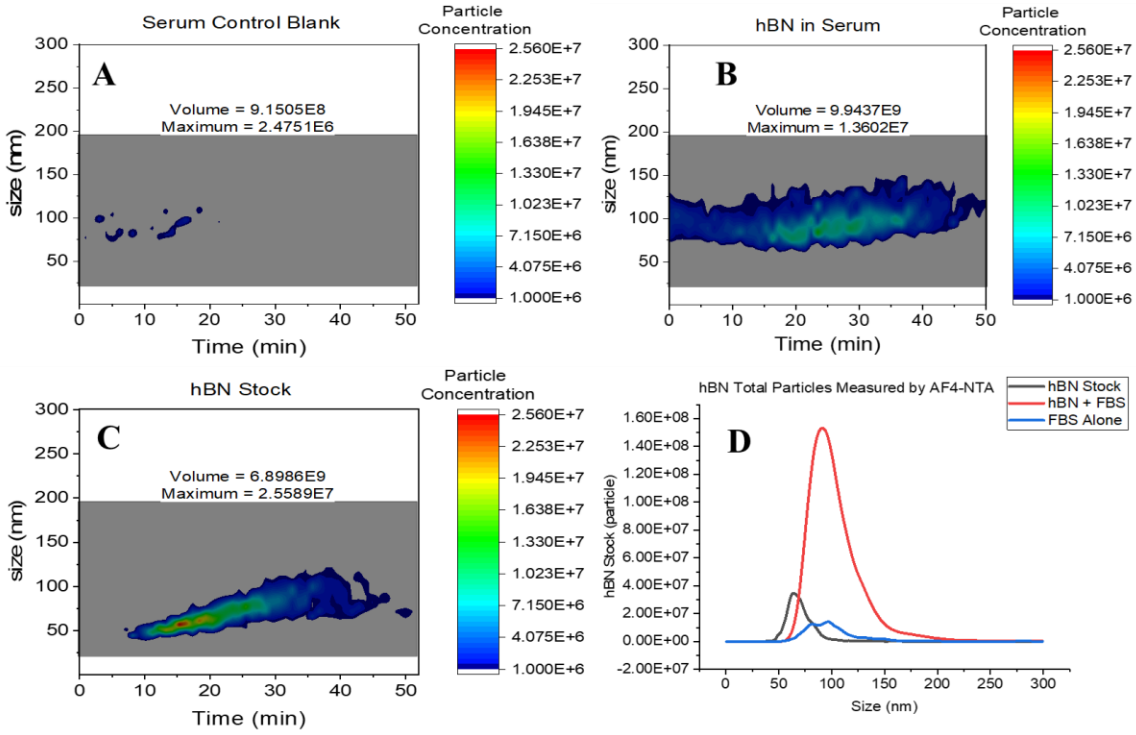

Figure 3.4 - hBN stock, background FBS, and hBN+FBS AF4-NTA results showing protein corona formation.

Figure 3.4B shows the results of the run after the hBN was dispersed in medium. The total particles were summed for the whole run and shown in a 2D plot in Figure 3.4D, and it shows a large increase in the number of particles measured as well as an increase in the size mode (apex) of the hBN peak. Table 3.2 shows the summary statistics of the 3 runs and it shows a fairly large increase in size of about 25 nm for hBN indicating a protein shell thickness of about 10-15 nm. There is also a large increase in the number of particles collected, surpassing the sum of both controls. The tailing ends of the hBN+FBS distribution are ~150 nm, which are much larger than the hBN without serum (~100 nm) and the background serum particles (~125 nm). There is also secondary tail on the hBN+FBS sample from 150-200 nm which could indicate protein unfolding and larger and

aggregation, but this could also be aggregation of hBN due to the unfolded proteins in the corona crosslinking multiple flakes. More analysis would be needed to understand the nature of the larger particles, whether the bulk is from protein aggregates or if the bulk is from aggregated hBN.

Table 3.2 - Summary statistics of the hBN, FBS and hBN + FBS of the AF4-NTA distributions.

	hBN Stock (Total Particles)	**FBS Alone (Total Particles)**	**hBN + FBS (Total Particles)**
Apex Value (particles)	**3.46E+07**	**1.42E+07**	**1.53E+08**
Total Particles (particles)	**8.68E+08**	**6.63E+08**	**7.04E+09**
Size Mode (nm)	**64**	**97**	**90**

The advantages of AF4-NTA allow quick size analysis and aggregate state determination of the NP and protein corona as the samples are prepared for various incubations in toxicology studies. Sample preparation for AF4-NTA mimicked toxicology study preparation protocols and required no additional requirements for injection and analysis. Samples are not only rapidly analyzed, but they are also fractionated and can be analyzed for corona contents, ROS generation, etc. AF4-NTA shows enhanced data capability and increased efficiency in toxicology assays involving NPs and biological interactions.

*3.3.3 - **Exosomes and Human Serum***

The final arm was to analyze softer, less dense particles and to separate human serum in the AF4-NTA system. Figure 3.5A and 3.5B shows 3D fractograms of 2.5 and 10 µg of exosome standards free of soluble protein. The distributions showed similarity to the COA distribution provided by the supplier that showed a wide distribution of particles with the apex being very close to 100 nm. The 2.5 µg sample does not have enough particles to show a clear distribution, however the quantification does show a comparable number of particles relating to the injected mass of exosomes. When both injections are normalized to 10 µg injection amounts, the particle counts are 3.17E+08 and 3.38E+08, showing only 6.21 % variance between the two values. The previous chapter as well as the work outlined here continue to display very linear responses based on injection amounts.

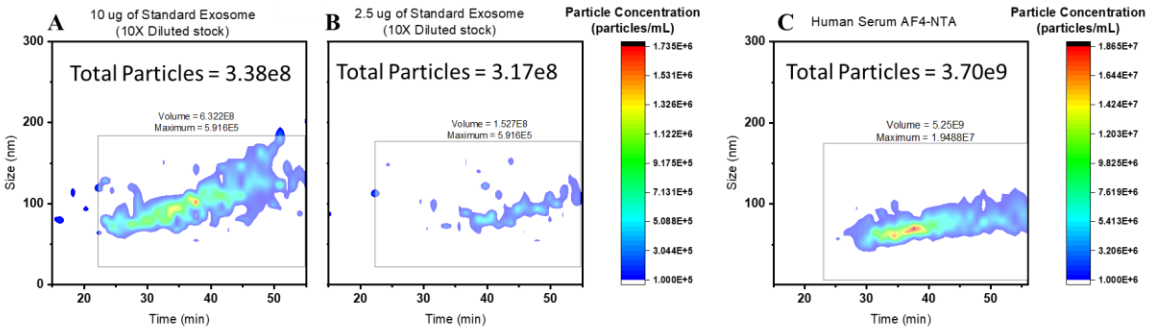

Figure 3.5 - Two injection masses of exosome standards and human serum in AF4-NTA. Exosome standards were purified from cell culture medium and could explain the larger size distribution compared to collected serum.

Exosome standards are enriched and free of background protein, but serum will contain background protein, protein aggregates, lipoproteins, and microvesicles as well. Figure 3.5C shows the fractogram of serum and shows a much larger number of particles,

but also shows a much smaller width in sizes than the exosome sample. One of the reasons for this may be the source of the vesicles, as they are sourced from cell cultures and purified while the human serum is collected from healthy patients' blood. Exosome standards are double purified and these purification steps, especially if ultracentrifuge was used, can cause aggregation and fusion of the purified exosomes. This further backs up the hypothesis that AF4-NTA BioNPs are truer to the native state when normally found in serum.

3.4 - Conclusions

The work here displays versatility and wide applicability of AF4-NTA to analyze many sample types and sample matrices. AF4-NTA can analyze non-spherical models, but access to microscopic or other techniques that can measure the major axis length or D_R is needed. AF4-NTA is also very good at handling softer materials and biological targets because it can gently wash the NPs while also preserving the NP structure and associated proteins. The speed of data collection and automated nature of the system allows this to be done in conjunction with other assays, especially considering the system can handle crude samples, is label-free, and fractionates the sample for further analysis.

3.5 - References

(1) de la Calle, I.; Soto-Gómez, D.; Pérez-Rodríguez, P.; López-Periago, J. E. Particle Size Characterization of Sepia Ink Eumelanin Biopolymers by SEM, DLS, and AF4-MALLS: A Comparative Study. *Food Anal. Methods* **2019**, *12* (5), 1140–1151. https://doi.org/10.1007/s12161-019-01448-0.

(2) Mathaes, R.; Winter, G.; Engert, J.; Besheer, A. Application of Different Analytical Methods for the Characterization of Non-Spherical Micro- and Nanoparticles. *Int. J. Pharm.* **2013**, *453* (2), 620–629. https://doi.org/10.1016/j.ijpharm.2013.05.046.

(3) Parot, J.; Caputo, F.; Mehn, D.; Hackley, V. A.; Calzolai, L. Physical Characterization of Liposomal Drug Formulations Using Multi-Detector Asymmetrical-Flow Field Flow Fractionation. *J. Controlled Release* **2020**, *320*, 495–510. https://doi.org/10.1016/j.jconrel.2020.01.049.

(4) Mildner, R.; Hak, S.; Parot, J.; Hyldbakk, A.; Borgos, S. E.; Some, D.; Johann, C.; Caputo, F. Improved Multidetector Asymmetrical-Flow Field-Flow Fractionation Method for Particle Sizing and Concentration Measurements of Lipid-Based Nanocarriers for RNA Delivery. *Eur. J. Pharm. Biopharm.* **2021**, *163*, 252–265. https://doi.org/10.1016/j.ejpb.2021.03.004.

(5) Sitar, S.; Kejžar, A.; Pahovnik, D.; Kogej, K.; Tušek-Žnidarič, M.; Lenassi, M.; Žagar, E. Size Characterization and Quantification of Exosomes by Asymmetrical-Flow Field-Flow Fractionation. *Anal. Chem.* **2015**, *87* (18), 9225–9233. https://doi.org/10.1021/acs.analchem.5b01636.

(6) Gollwitzer, C.; Bartczak, D.; Goenaga-Infante, H.; Kestens, V.; Krumrey, M.; Minelli, C.; Pálmai, M.; Ramaye, Y.; Roebben, G.; Sikora, A.; Varga, Z. A Comparison of Techniques for Size Measurement of Nanoparticles in Cell Culture Medium. *Anal. Methods* **2016**, *8* (26), 5272–5282. https://doi.org/10.1039/c6ay00419a.

(7) Giddings, J. C. Field Flow Fractionation: A Versatile Method for the Characterization of Macromolecular and Particulate Materials. *Anal. Chem.* **1981**, *53* (11), 1170–1178. https://doi.org/10.1021/ac00234a001.

(8) Contado, C. Field Flow Fractionation Techniques to Explore the "Nano-World." *Anal. Bioanal. Chem.* **2017**, *409* (10), 2501–2518. https://doi.org/10.1007/s00216-017-0180-6.

(9) Caputo, F.; Arnould, A.; Bacia, M.; Ling, W. L.; Rustique, E.; Texier, I.; Mello, A. P.; Couffin, A. C. Measuring Particle Size Distribution by Asymmetric Flow Field Flow Fractionation: A Powerful Method for the Preclinical Characterization of

Lipid-Based Nanoparticles. *Mol. Pharm.* **2019**, *16* (2), 756–767. https://doi.org/10.1021/acs.molpharmaceut.8b01033.

(10) Alasonati, E. A.; Benincasa, M. A.; Slaveykova, V. I. Asymmetrical Flow Field-Flow Fractionation Coupled to Multiangle Laser Light Scattering Detector: Optimization of Crossflow Rate, Carrier Characteristics, and Injected Mass in Alginate Separation. *J. Sep. Sci.* **2007**, *30* (14), 2332–2340. https://doi.org/10.1002/jssc.200700211.

(11) Pitkänen, L.; M. Striegel, A. AF4/MALS/QELS/DRI Characterization of Regular Star Polymers and Their "Span Analogs." *Analyst* **2014**, *139* (22), 5843–5851. https://doi.org/10.1039/C4AN01105H.

(12) Petersen, K. E.; Manangon, E.; Hood, J. L.; Wickline, S. A.; Fernandez, D. P.; Johnson, W. P.; Gale, B. K. A Review of Exosome Separation Techniques and Characterization of B16-F10 Mouse Melanoma Exosomes with AF4-UV-MALS-DLS-TEM. *Anal. Bioanal. Chem.* **2014**, *406* (30), 7855–7866. https://doi.org/10.1007/s00216-014-8040-0.

(13) Tamkovich, S. N.; Yunusova, N. V.; Stakheeva, M. N.; Somov, A. K.; Frolova, A. Y.; Kirushina, N. A.; Afanasyev, S. G.; Grigoryeva, A. E.; Laktionov, P. P.; Kondakova, I. V. [Isolation and Characterization of Exosomes from Blood Plasma of Breast Cancer and Colorectal Cancer Patients]. *Biomeditsinskaia Khimiia* **2017**, *63* (2), 165–169.

(14) Tauro, B. J.; Greening, D. W.; Mathias, R. A.; Ji, H.; Mathivanan, S.; Scott, A. M.; Simpson, R. J. Comparison of Ultracentrifugation, Density Gradient Separation, and Immunoaffinity Capture Methods for Isolating Human Colon Cancer Cell Line LIM1863-Derived Exosomes. *Methods* **2012**, *56* (2), 293–304. https://doi.org/10.1016/j.ymeth.2012.01.002.

(15) Wu, Y.; Deng, W.; Klinke, D. J.; Klinke II, D. J.; Théry, C.; Ostrowski, M. C.; Segura, E.; Andaloussi, S. E.; Mäger, I.; Breakefield, X. O.; Wood, M. J.; Robbins, P. D.; Morelli, A. E.; Harding, C.; Heuser, J.; Stahl, P.; Pan, B. T.; Teng, K.; Wu, C.; Adam, M.; Johnstone, R. M.; Valadi, H.; Ekström, K.; Bossios, A.; Sjöstrand, M.; Lee, J. J.; Lötvall, J. O.; Skog, J.; Würdinger, T.; Rijn, S. van; Meijer, D. H.; Gainche, L.; Sena-Esteves, M.; Curry, W. T.; Carter, B. S.; Krichevsky, A. M.; Breakefield, X. O.; Taylor, D. D.; Gercel-Taylor, C.; Al-Nedawi, K.; Meehan, B.; Micallef, J.; Lhotak, V.; May, L.; Guha, A.; Rak, J.; Peinado, H.; Alečković, M.; Lavotshkin, S.; Matei, I.; Costa-Silva, B.; Moreno-Bueno, G.; Hergueta-Redondo, M.; Williams, C.; García-Santos, G.; Ghajar, C.; Nitadori-Hoshino, A.; Hoffman, C.; Badal, K.; Garcia, B. a.; Callahan, M. K.; Yuan, J.; Martins, V. R.; Skog, J.; Kaplan, R. N.; Brady, M. S.; Wolchok, J. D.; Chapman, P. B.; Kang, Y.; Bromberg, J.; Lyden, D.; Peinado, H.; Lavotshkin, S.; Lyden, D.; Luketic, L.; Delanghe, J.; Sobol, P. T.; Yang, P.; Frotten, E.; Mossman, K. L.; Gauldie, J.; Bramson, J. L.;

Wan, Y.; Balaj, L.; Lessard, R.; Dai, L.; Cho, Y.-J.; Pomeroy, S. L.; Breakefield, X. O.; Skog, J.; Boelens, M. C.; Wu, T. J.; Nabet, B. Y.; Xu, B.; Qiu, Y.; Yoon, T.; Azzam, D. J.; Victor, C. T.-S.; Wiemann, B. Z.; Ishwaran, H.; Brugge, P. J. ter; Jonkers, J.; Slingerland, J.; Minn, A. J.; Bronisz, A.; Wang, Y.; Nowicki, M. O.; Peruzzi, P.; Ansari, K. I.; Ogawa, D.; Balaj, L.; Rienzo, G. D.; Mineo, M.; Nakano, I.; Ostrowski, M. C.; Hochberg, F.; Weissleder, R.; Lawler, S. E.; Chiocca, E. A.; Godlewski, J.; Clayton, A.; Mitchell, J. P.; Court, J.; Mason, M. D.; Tabi, Z.; Linnane, S.; Iero, M.; Valenti, R.; Huber, V.; Filipazzi, P.; Parmiani, G.; Fais, S.; Rivoltini, L.; Webber, J. P.; Spary, L. K.; Sanders, A. J.; Chowdhury, R.; Jiang, W. G.; Steadman, R.; Wymant, J.; Jones, A. T.; Kynaston, H.; Mason, M. D.; Tabi, Z.; Clayton, A.; Webber, J. P.; Steadman, R.; Mason, M. D.; Tabi, Z.; Clayton, A.; Kulkarni, Y. M.; II, D. J. K.; Wu, Y.; Byrne-Hoffman, C.; Ratajczak, J.; Wysoczynski, M.; Hayek, F.; Janowska-Wieczorek, A.; Ratajczak, M. Z.; Somasundaram, R.; Herlyn, M.; Hood, J. L.; San, R. S.; Wickline, S. A.; Andre, F.; Schartz, N. E. C.; Movassagh, M.; Flament, C.; Pautier, P.; Morice, P.; Pomel, C.; Lhomme, C.; Escudier, B.; Chevalier, T. L.; Tursz, T.; Amigorena, S.; Raposo, G.; Angevin, E.; Zitvogel, L.; Hood, J. L.; Pan, H.; Lanza, G. M.; Wickline, S. A.; Taylor, D. D.; Gerçel-Taylor, C.; Dai, S.; Wan, T.; Wang, B.; Zhou, X.; Xiu, F.; Chen, T.; Wu, Y.; Cao, X.; Wolfers, J.; Lozier, A.; Raposo, G.; Regnault, A.; Théry, C.; Masurier, C.; Flament, C.; Pouzieux, S.; Faure, F.; Tursz, T.; Angevin, E.; Amigorena, S.; Zitvogel, L.; Nilsson, J.; Skog, J.; Nordstrand, A.; Baranov, V.; Mincheva-Nilsson, L.; Breakefield, X. O.; Widmark, A.; Mitchell, P. J.; Welton, J.; Staffurth, J.; Court, J.; Mason, M. D.; Tabi, Z.; Clayton, A.; Villarroya-Beltri, C.; Baixauli, F.; Gutiérrez-Vázquez, C.; Sánchez-Madrid, F.; Mittelbrunn, M.; Filipazzi, P.; Bürdek, M.; Villa, A.; Rivoltini, L.; Huber, V.; Keller, S.; Ridinger, J.; Rupp, A.-K.; Janssen, J. W. G.; Altevogt, P.; Clayton, A.; Mason, M. D.; Gross, J. C.; Chaudhary, V.; Bartscherer, K.; Boutros, M.; Xu, D.; Tahara, H.; Sharma, P.; Schiapparelli, L.; Cline, H. T.; Okoye, I. S.; Coomes, S. M.; Pelly, V. S.; Czieso, S.; Papayannopoulos, V.; Tolmachova, T.; Seabra, M. C.; Wilson, M. S.; Fleming, A. B.; Saltzman, W. M.; Cocucci, E.; Racchetti, G.; Meldolesi, J.; Raposo, G.; Stoorvogel, W.; Mathivanan, S.; Ji, H.; Simpson, R. J.; Kulkarni, Y. M.; Chambers, E.; McGray, A. J. R.; Ware, J. S.; Bramson, J. L.; II, D. J. K.; Kulkarni, Y. M.; II, D. J. K.; Théry, C.; Amigorena, S.; Raposo, G.; Clayton, A.; Hu, W.; Zhang, C.; Fang, Y.; Lou, C.; II, D. J. K.; Brundage, K. M.; Pol, E. van der; Hoekstra, a. G.; Sturk, A.; Otto, C.; Leeuwen, T. G. van; Nieuwland, R.; Sokolova, V.; Ludwig, A.-K.; Hornung, S.; Rotan, O.; Horn, P. A.; Epple, M.; Giebel, B.; Sharma, S.; Rasool, H. I.; Palanisamy, V.; Mathisen, C.; Schmidt, M.; Wong, D. T.; Gimzewski, J. K.; György, B.; Szabó, T. G.; Pásztói, M.; Pál, Z.; Misják, P.; Aradi, B.; László, V.; Pállinger, E.; Pap, E.; Kittel, A.; Nagy, G.; Falus, A.; Buzás, E. I.; Tang, L.; Fan, T. M.; Borst, L. B.; Cheng, J.; Reddy, S. T.; Vlies, A. J. van der; Simeoni, E.; O'Neil, C. P.; Swartz, M. A.; Hubbell, J. A.; Irvine, D. J.; Swartz, M. A.; Szeto, G. L.; Pol, E. van der; Gemert, M. J. van; Sturk, A.; Nieuwland, R.; Leeuwen, T. G. van; Maas, S. L. N.; Vrij, J. de; Vlist, E. J. van der; Geragousian, B.; Bloois, L. van; Mastrobattista, E.; Schiffelers, R. M.; Wauben, M. H. M.; Broekman, M. L.

D.; Hoen, E. N. N.-'t M. N.-'t; Erlandsen, S. L.; Bemrick, W. J.; Schupp, D. E.; Shields, J. M.; Jarroll, E. L.; Sauch, J. F.; Pawley, J. B.; Speirs, V.; Eich-Bender, S.; Youngson, C. R.; Cutz, E.; Hoen, E. N. N.-'t M. N.-'t; Vlist, E. J. van der; Aalberts, M.; Mertens, H. C.; Bosch, B. J.; Bartelink, W.; Mastrobattista, E.; Gaal, E. V. B. van; Stoorvogel, W.; Arkesteijn, G. J.; Wauben, M. H. M.; Vlist, E. J. van der; Hoen, E. N. N.-'t M. N.-'t; Stoorvogel, W.; Arkesteijn, G. J.; Wauben, M. H. M.; Higginbotham, J. N.; Beckler, M. D.; Gephart, J. D.; Franklin, J. L.; Bogatcheva, G.; Kremers, G. J.; Piston, D. W.; Ayers, G. D.; McConnell, R. E.; Tyska, M. J.; Coffey, R. J.; Batagov, A. O.; Kurochkin, I. V.; Ekstrom, K.; Valadi, H.; Sjostrand, M.; Malmhall, C.; Bossios, A.; Eldh, M.; Lotvall, J.; Pegtel, D. M.; Cosmopoulos, K.; Thorley-Lawson, D. A.; Eijndhoven, M. A. van; Hopmans, E. S.; Lindenberg, J. L.; Gruijl, T. D. de; Würdinger, T.; Middeldorp, J. M.; Klinke, D. J. Exosomes: Improved Methods to Characterize Their Morphology, RNA Content, and Surface Protein Biomarkers. *The Analyst* **2015**, *140* (19), 6631–6642. https://doi.org/10.1039/c5an00688k.

(16) Zhang, H.; Freitas, D.; Kim, H. S.; Fabijanic, K.; Li, Z.; Chen, H.; Mark, M. T.; Molina, H.; Martin, A. B.; Bojmar, L.; Fang, J.; Rampersaud, S.; Hoshino, A.; Matei, I.; Kenific, C. M.; Nakajima, M.; Mutvei, A. P.; Sansone, P.; Buehring, W.; Wang, H.; Jimenez, J. P.; Cohen-Gould, L.; Paknejad, N.; Brendel, M.; Manova-Todorova, K.; Magalhães, A.; Ferreira, J. A.; Osório, H.; Silva, A. M.; Massey, A.; Cubillos-Ruiz, J. R.; Galletti, G.; Giannakakou, P.; Cuervo, A. M.; Blenis, J.; Schwartz, R.; Brady, M. S.; Peinado, H.; Bromberg, J.; Matsui, H.; Reis, C. A.; Lyden, D. Identification of Distinct Nanoparticles and Subsets of Extracellular Vesicles by Asymmetric Flow Field-Flow Fractionation. *Nat. Cell Biol.* **2018**, *20* (3), 332–343. https://doi.org/10.1038/s41556-018-0040-4.

(17) Kuklenyik, Z.; Gardner, M. S.; Parks, B. A.; Schieltz, D. M.; Rees, J. C.; Mcwilliams, L. G.; Williamson, Y. M.; Pirkle, J. L.; Barr, J. R. Multivariate DoE Optimization of Asymmetric Flow Field Flow Fractionation Coupled to Quantitative LC-MS/MS for Analysis of Lipoprotein Subclasses. *Chromatography* **2015**, *2*, 96–117. https://doi.org/10.3390/chromatography2010096.

(18) Sitar, S.; Kejžar, A.; Pahovnik, D.; Kogej, K.; Tušek-Žnidarič, M.; Lenassi, M.; Žagar, E. Size Characterization and Quantification of Exosomes by Asymmetrical-Flow Field-Flow Fractionation. *Anal. Chem.* **2015**, *87* (18), 9225–9233. https://doi.org/10.1021/acs.analchem.5b01636.

(19) Abdolahpur Monikh, F.; Grundschober, N.; Romeijn, S.; Arenas-Lago, D.; Vijver, M. G.; Jiskoot, W.; Peijnenburg, W. J. G. M. Development of Methods for Extraction and Analytical Characterization of Carbon-Based Nanomaterials (Nanoplastics and Carbon Nanotubes) in Biological and Environmental Matrices by Asymmetrical Flow Field-Flow Fractionation. *Environ. Pollut.* **2019**, *255*, 113304. https://doi.org/10.1016/j.envpol.2019.113304.

(20) Vezočnik, V.; Rebolj, K.; Sitar, S.; Ota, K.; Tušek-Žnidarič, M.; Štrus, J.; Sepčić, K.; Pahovnik, D.; Maček, P.; Žagar, E. Size Fractionation and Size Characterization of Nanoemulsions of Lipid Droplets and Large Unilamellar Lipid Vesicles by Asymmetric-Flow Field-Flow Fractionation/Multi-Angle Light Scattering and Dynamic Light Scattering. *J. Chromatogr. A* **2015**, *1418*, 185–191. https://doi.org/10.1016/j.chroma.2015.09.048.

(21) Ashby, J.; Schachermeyer, S.; Pan, S.; Zhong, W. Dissociation-Based Screening of Nanoparticle–Protein Interaction via Flow Field-Flow Fractionation. *Anal. Chem.* **2013**, *85* (15), 7494–7501. https://doi.org/10.1021/ac401485j.

(22) Schachermeyer, S.; Ashby, J.; Zhong, W. Aptamer–Protein Binding Detected by Asymmetric Flow Field Flow Fractionation. *J. Chromatogr. A* **2013**, *1295*, 107–113. https://doi.org/10.1016/J.CHROMA.2013.04.063.

(23) Wang, L.; Lee, J. Y.; Gao, L.; Yin, J.; Duan, Y.; Jimenez, L. A.; Adkins, G. B.; Ren, W.; Li, L.; Fang, J.; Wang, Y.; Song, J.; Zhong, W. A DNA Aptamer for Binding and Inhibition of DNA Methyltransferase 1. *Nucleic Acids Res.* **2019**, *47* (22), 11527–11537. https://doi.org/10.1093/nar/gkz1083.

(24) Ashby, J.; Schachermeyer, S.; Duan, Y.; Jimenez, L. A.; Zhong, W. Probing and Quantifying DNA–Protein Interactions with Asymmetrical Flow Field-Flow Fractionation. *J. Chromatogr. A* **2014**, *1358*, 217–224. https://doi.org/10.1016/j.chroma.2014.07.002.

(25) Maas, S. L. N.; de Vrij, J.; van der Vlist, E. J.; Geragousian, B.; van Bloois, L.; Mastrobattista, E.; Schiffelers, R. M.; Wauben, M. H. M.; Broekman, M. L. D.; Nolte-'t Hoen, E. N. M. Possibilities and Limitations of Current Technologies for Quantification of Biological Extracellular Vesicles and Synthetic Mimics. *J. Control. Release Off. J. Control. Release Soc.* **2015**, *200*, 87–96. https://doi.org/10.1016/j.jconrel.2014.12.041.

(26) Gruia, F.; Parupudi, A.; Polozova, A. Practical Considerations for Detection and Characterization of Sub-Micron Particles in Protein Solutions by Nanoparticle Tracking Analysis. *PDA J. Pharm. Sci. Technol.* **2015**, *69* (3), 427–439. https://doi.org/10.5731/pdajpst.2015.01051.

(27) Filipe, V.; Hawe, A.; Jiskoot, W. Critical Evaluation of Nanoparticle Tracking Analysis (NTA) by NanoSight for the Measurement of Nanoparticles and Protein Aggregates. *Pharm. Res.* **2010**, *27* (5), 796–810. https://doi.org/10.1007/s11095-010-0073-2.

(28) Sokolova, V.; Ludwig, A.-K.; Hornung, S.; Rotan, O.; Horn, P. A.; Epple, M.; Giebel, B. Characterisation of Exosomes Derived from Human Cells by Nanoparticle Tracking Analysis and Scanning Electron Microscopy. *Colloids Surf.*

B Biointerfaces **2011**, *87* (1), 146–150. https://doi.org/10.1016/j.colsurfb.2011.05.013.

(29) Krueger, A. B.; Carnell, P.; Carpenter, J. F. Characterization of Factors Affecting Nanoparticle Tracking Analysis Results with Synthetic and Protein Nanoparticles. *J. Pharm. Sci.* **2016**, *105* (4), 1434–1443. https://doi.org/10.1016/j.xphs.2016.02.005.

(30) Nanoparticle tracking analysis for the multiparameter characterization and counting of nanoparticle suspensions - PubMed https://pubmed.ncbi.nlm.nih.gov/22791460/ (accessed 2021 -07 -14).

(31) Sharma, V.; Park, K.; Srinivasarao, M. Shape Separation of Gold Nanorods Using Centrifugation. *Proc. Natl. Acad. Sci.* **2009**, *106* (13), 4981–4985. https://doi.org/10.1073/pnas.0800599106.

(32) Xiong, B.; Cheng, J.; Qiao, Y.; Zhou, R.; He, Y.; Yeung, E. S. Separation of Nanorods by Density Gradient Centrifugation. *J. Chromatogr. A* **2011**, *1218* (25), 3823–3829. https://doi.org/10.1016/J.CHROMA.2011.04.038.

(33) Yu, X.; Yun, S.; Yeon, J. S.; Bhattacharya, P.; Wang, L.; Lee, S. W.; Hu, X.; Park, H. S. Emergent Pseudocapacitance of 2D Nanomaterials. *Adv. Energy Mater.* **2018**, *8* (13), 1702930. https://doi.org/10.1002/aenm.201702930.

(34) Zhu, Y.; Peng, L.; Fang, Z.; Yan, C.; Zhang, X.; Yu, G. Structural Engineering of 2D Nanomaterials for Energy Storage and Catalysis. *Adv. Mater.* **2018**, *30* (15), 1706347. https://doi.org/10.1002/adma.201706347.

(35) Tuning Size and Sensing Properties in Colloidal Gold Nanostars | Langmuir https://pubs.acs.org/doi/full/10.1021/la102559e (accessed 2021 -07 -29).

(36) Esenturk, E. N.; Walker, A. R. H. Surface-Enhanced Raman Scattering Spectroscopy via Gold Nanostars. *J. Raman Spectrosc.* **2009**, *40* (1), 86–91. https://doi.org/10.1002/jrs.2084.

(37) Barbosa, S.; Agrawal, A.; Rodríguez-Lorenzo, L.; Pastoriza-Santos, I.; Alvarez-Puebla, R. A.; Kornowski, A.; Weller, H.; Liz-Marzán, L. M. Tuning Size and Sensing Properties in Colloidal Gold Nanostars. *Langmuir* **2010**, *26* (18), 14943–14950. https://doi.org/10.1021/la102559e.

(38) Malloy, A.; Carr, B. NanoParticle Tracking Analysis - The Halo^{TM} System. *Part. Part. Syst. Charact.* **2006**, *23* (2), 197–204. https://doi.org/10.1002/ppsc.200601031.

(39) Hoover, B. M.; Murphy, R. M. Evaluation of Nanoparticle Tracking Analysis for the Detection of Rod-Shaped Particles and Protein Aggregates. *J. Pharm. Sci.* **2020**, *109* (1), 452–463. https://doi.org/10.1016/j.xphs.2019.10.006.

(40) Duan, Y.; Coreas, R.; Liu, Y.; Bitounis, D.; Zhang, Z.; Parviz, D.; Strano, M.; Demokritou, P.; Zhong, W. Prediction of Protein Corona on Nanomaterials by Machine Learning Using Novel Descriptors. *NanoImpact* **2020**, 100207. https://doi.org/10.1016/j.impact.2020.100207.

(41) Adkins, G. B.; Sun, E.; Coreas, R.; Zhong, W. Asymmetrical Flow Field Flow Fractionation Coupled to Nanoparticle Tracking Analysis for Rapid Online Characterization of Nanomaterials. *Anal. Chem.* **2020**, acs.analchem.0c00406. https://doi.org/10.1021/acs.analchem.0c00406.

(42) Arenas-Guerrero, P.; Delgado, Á. V.; Donovan, K. J.; Scott, K.; Bellini, T.; Mantegazza, F.; Jiménez, M. L. Determination of the Size Distribution of Non-Spherical Nanoparticles by Electric Birefringence-Based Methods. *Sci. Rep.* **2018**, *8* (1), 9502. https://doi.org/10.1038/s41598-018-27840-0.

(43) Multipolarization Dynamic Light Scattering of Nonspherical Nanoparticles in Solution | The Journal of Physical Chemistry C https://pubs.acs.org/doi/10.1021/acs.jpcc.6b10226 (accessed 2021 -07 -14).

(44) Filipe, V.; Hawe, A.; Jiskoot, W. Critical Evaluation of Nanoparticle Tracking Analysis (NTA) by NanoSight for the Measurement of Nanoparticles and Protein Aggregates. *Pharm. Res.* **2010**, *27* (5), 796–810. https://doi.org/10.1007/s11095-010-0073-2.

(45) Shang, J.; Gao, X. Nanoparticle Counting: Towards Accurate Determination of the Molar Concentration. *Chem. Soc. Rev.* **2014**, *43* (21), 7267–7278. https://doi.org/10.1039/C4CS00128A.

(46) Maguire, C. M.; Rösslein, M.; Wick, P.; Prina-Mello, A. Characterisation of Particles in Solution – a Perspective on Light Scattering and Comparative Technologies. *Sci. Technol. Adv. Mater.* **2018**, *19* (1), 732–745. https://doi.org/10.1080/14686996.2018.1517587.

(47) Sitar, S.; Vezočnik, V.; Maček, P.; Kogej, K.; Pahovnik, D.; Žagar, E. Pitfalls in Size Characterization of Soft Particles by Dynamic Light Scattering Online Coupled to Asymmetrical Flow Field-Flow Fractionation. *Anal. Chem.* **2017**, *89* (21). https://doi.org/10.1021/acs.analchem.7b03251.

(48) Glidden, M.; Muschol, M. Characterizing Gold Nanorods in Solution Using Depolarized Dynamic Light Scattering. *J. Phys. Chem. C* **2012**, *116* (14), 8128–8137. https://doi.org/10.1021/jp211533d.

(49) Tirado, M. M.; Martínez, C. L.; de la Torre, J. G. Comparison of Theories for the Translational and Rotational Diffusion Coefficients of Rod-like Macromolecules. Application to Short DNA Fragments. *J. Chem. Phys.* **1984**, *81* (4), 2047–2052. https://doi.org/10.1063/1.447827.

Chapter 4: Downstream Analysis of Extracellular Vesicles

4.1 - Introduction

Cancer biomarkers can be detected on extracellular vesicles secreted from the parent cancer cells.[1–20] Cancer cells also have been shown to secrete an increased number of vesicles or have altered distributions compared to the healthy cell during progression of the disease.[21–25] Analyzing cancerous tissues in cell cultures are very tedious and require large amounts of sample due to poor isolation methods.[26–30,30–34] Large-scale protocols for ultracentrifugation combined with vesicle characterization and downstream protein analysis can take approximately 3 days using high yield density gradient ultracentrifugation and the assays needed to properly characterize the recovery of BioNPs.[35–37] During that time, sample degradation, aggregation, and processing yield losses can occur, dramatically altering the data generated by the end of the process.

Circulating vesicles are much easier to access than internal tissue and can be exploited for rapid disease information. A liquid biopsy is a technique that collects BioNPs from biofluids to analyze diseased tissue by collecting the exosomes or microvesicles found in biofluids and performing protein, metabolite, or nucleotide analysis to determine the disease state or the best treatment option without needing to perform invasive and costly surgeries.[3,38–43] Additionally, liquid biopsies can be performed rapidly with a blood test and can reduce the time it takes to initiate proper treatment after the initial diagnosis.[44–47] Exosomes contain surface proteins, cytosolic proteins, metabolites, as well as small RNA like mRNA and miRNA. One of the most promising liquid biopsy targets are the renal organs and urine.[13,18,47–50] Urine has direct contact with the kidneys, bladder, and prostrate

and it has been prefiltered from all other tissues by the kidneys making it much easier to identify expression levels specific to renal organs only.[13]

AF4-NTA is ideal for rapid characterization of BioNPs providing size-separated, fractionated samples that can be analyzed downstream for protein or other cargo contents with very little preprocessing or sample modifications. Combining this technique with traditional and modified western blot (WB) or enzyme-linked immunosorbent assay (ELISA) assays on the fractionated samples can provide relative protein quantities which can be related to the online size distribution and quantity. Additionally, surface area can be determined, and a ratio of protein/surface area could be used to identify expression levels of surface receptors.

Our modified western blot technique utilizes nitrocellulose membranes and a vacuum dot-blot apparatus to adsorb the fractionated vesicles to a nitrocellulose (NC) membrane.[51–53] Instead of electrolytic diffusion from a slab gel to NC membrane, aqueous samples are incubated on the membrane in the dot blot apparatus and slowly pulled through the porous membrane with a gentle vacuum. The hydrophobic and electrostatic interactions of proteins and lipids with the membrane causes binding and disruption of the vesicle and adsorption of the vesicle's membrane proteins.[54–56] This technique can quickly adsorb and concentrate proteins found in the fractions and can counter low concentration volumes by concentrating the analyte into a small region on the membrane.

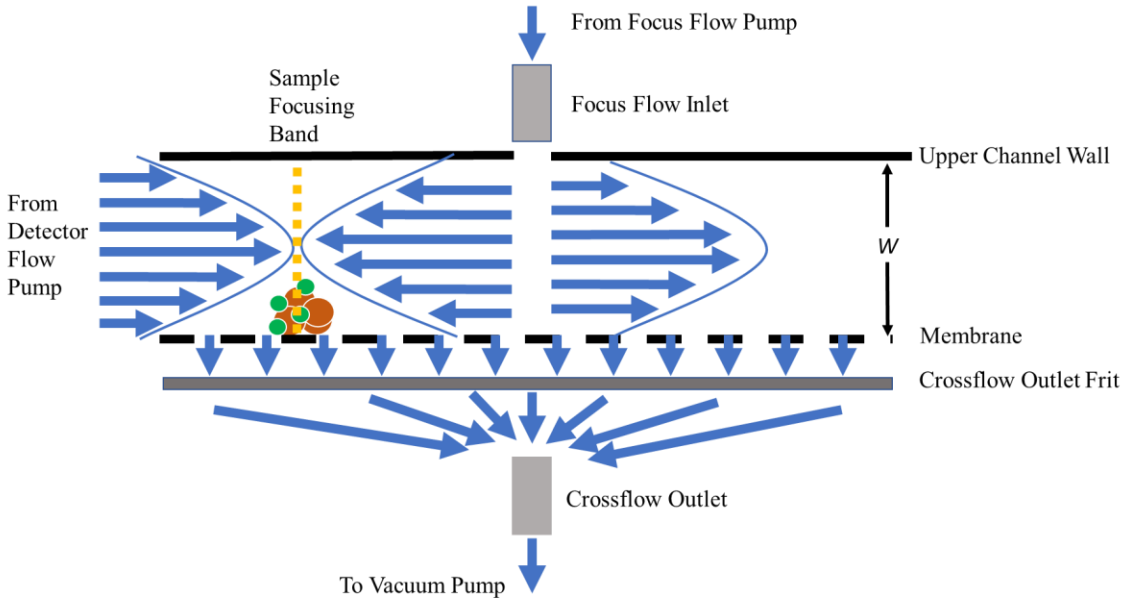

Figure 4.1 - AF4 channel undergoing focusing. The sample plug is confined by the opposing forces to a high concentration region. The pressure fluctuations in the 3 opposing flows along with electrostatic repulsion and self-diffusion provide increased mobility to the probes and NPs in the confined space, with smaller probes seeing better diffusivity ion the region.

Another technique this chapter explores is the utilization of the focusing step to develop an *in-situ* labeling technique. Figure 4.1 shows a schematic of the AF4 channel during focusing with a sample focused before separation. The focusing region contains the sample within the opposing flows and concentrates it to a small volume.[57] High efficiency binding can occur in this region due to the confined space and constant agitation the sample plug feels from the opposing forces, electrostatic repulsion, and self-diffusion. Adding biological probes to the medium directly before injection leads to pre-fractionation labeling with fluorescent dyes. The size separation and gentle washing allows separation of the unbound and bound dyes while also washing any nonspecifically adsorbed probes. This

simplifies the downstream analysis by the removal of the individual antibody probing, blocking, and washing steps. With pre-labeled proteins, the steps reduce to adsorbing proteins to the NC membrane and then directly imaging the NC membrane. Issues with high LOD or LOQ can be overcome with more advanced probes that offer better signaling strategies like nucleic acid amplification or specific signal generation like horseradish peroxidase (HRP), which can provide better signal to noise ratios than fluorescent dyes.

This chapter focuses on developing techniques to rapidly characterize vesicles and quantify proteins found on the vesicle's surface in a matter of hours instead of days. The AF4 system will be utilized as a pseudo purification unit by separating serum and cell culture medium directly without the need of the standard purification steps. Assays will be modified to work with the AF4 separation system to allow probing of the sample and separate the bound and unbound probes from the exosomes found in the BioNPs eluted from serum and medium.

4.2 - Methods

4.2.1 - Materials

Dulbecco′s Modified Eagle′s Medium, high glucose (DMEM) (Cat# 11965092), SuperSignal West Pico Chemiluminescent Substrate (Cat# PI34077), EZ-Link™ NHS-LC-LC-Biotin Reagent Kit (Cat# 21343), and Pierce™ Biotin Quantitation Kit (Cat# 28005) were purchased from Thermo Fisher. Single Donor Human Serum Off the Clot samples were purchased from Innovative Research (Cat# ISERS2ML). FL-70 (Cat# SF1051), bovine serum albumin (BSA) (Cat# 50550390), and sodium azide (Cat# 190381000) were purchased from Fisher Scientific. Goat Anti-Mouse IgG (whole

molecule) (Cat# M8642-1MG) was purchased from Sigma Aldrich. IRDye® 800CW Goat anti-Mouse IgG and IRDye® 680RD Goat anti-Rabbit IgG were purchased from LI-COR. Mouse anti-cd63 IgG [MEM-259] (Cat# NB10077913) was purchased from Novus Biologicals. Mouse anti-CD81 IgG [M38] (Cat# ab79559-100ug), rabbit anti-CD63 IgG (Cat# ab216130-100ul), and mouse anti-Apolipoprotein B IgG [7B8] (Cat # ab39560) were purchased from Abcam. Mouse anti-CD9 IgG [MM2/57] (Cat# CBL162), human high-density lipoprotein (Cat# LP3-5MG), Streptavidin – Peroxidase Conjugate from Streptomyces a./horseradish (Cat# 85876), Amicon® Ultra-0.5 mL Centrifugal Filters (Cat # UFC500324), and human low-density lipoprotein (Cat# LP2-2MG) were purchased from Millipore. 10× PBS (Cat# PBS01-03) was purchased premixed from Bioland and was diluted to 1× and filtered daily. Exosome standards (Cat# HBM-COLO-100/2) were purchased from Galen Laboratory Supply and diluted to 100 µg/mL before being frozen for long term storage.

4.2.2 - Biological sample preparation

Three healthy human serum samples were pooled and aliquoted after directly after receiving. Samples were stored frozen at -80 °C for long term storage or -20 °C freezer for short term storage. Supplemented medium was created by diluting human serum to 10% using DMEM. To make a mock medium, BSA was added at 16 mg/mL to add protein mass, but not particles or antigens for the probes. 1 µg of primary and 0.5 µg of secondaries were added to 250 µL of medium directly before injection into AF4. Samples were diluted using 1× PBS when needed for assay preparation.

4.2.3 - Asymmetrical Flow Field Flow Fractionation

Optimized AF4 separations were performed using the exponential method shown in Figure 4.2. A 30 kDa regenerated cellulose membrane with a 350 μm spacer with a running buffer 1× PBS was used for all separations. Samples were fractionated in 2 mL collection tubes and analyzed immediately after or stored at 4°C until analysis. NTA analysis was done offline on collected fractions.

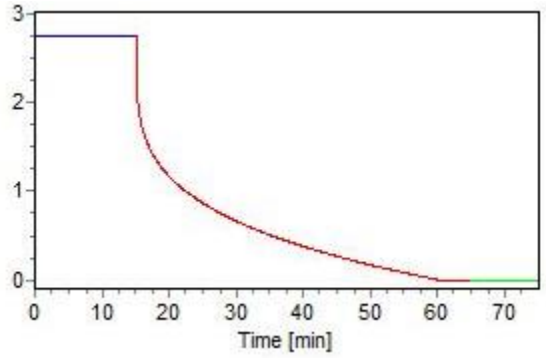

Figure 4.2 - AF4 exponential$^{0.25}$ method with a 15-minute focus is shown over 45 minutes.

4.2.4 - Nanoparticle Tracking Analysis

NTA was performed offline on collected fractions. The NTA data for each fraction was converted from particles/mL to just particles by multiplying the fraction volume by the concentration. NTA was done in using the attached syringe pump with a flow setting of 50 (arbitrary value which corresponds to about 10.6 μL/min) with a camera level of 12 or 13, just depending on how bright the particles were in the viewing window, with the later fractions needing level 12 to avoid flaring of the scatter point.

4.2.5 - Ultracentrifuge

Ultracentrifuge was carried out on a Beckman Coulter Optima-Max TL using a TLA-110 Fixed Angle Rotor and 4.7 mL OptiSeal propylene glycol centrifuge tubes. Various solution densities were generated by making 10-50% iodixanol solutions diluted with 1× PBS from a stock 60% iodixanol solution. The tube was layered in 3 layers, cushion, stripping, and sample. The cushion layer was composed of 40% or 50% iodixanol, the stripping layer was 10% or 20% iodixanol, and the sample layer was PBS containing 100 µL of conditioned serum. The ultracentrifuge tube was assembled by adding 1.5 mL of cushion solution first, followed by 1.5 mL of stripping solution, then finally 1.5 mL of 15× diluted human serum. Serum was preconditioned by differential ultracentrifugation, starting with 500 ×g to remove cells, then 2000 ×g to remove debris, and finally at 18,500 ×g to remove larger microvesicles and larger aggregates. The tubes were spun at 110,000 ×g for 18 hours. The boundary between the cushion and stripping layer was collected then diluted to a total volume of 4.5 mL and a second pelleting was done at 110,000 ×g for 70 minutes. The supernatant was discarded, and the resulting pellet was resuspended in 100 µL of fresh PBS. Characterization of the recovered exosomes was done immediately after resuspension using NTA and BCA Analysis.

4.2.6 - Precipitation Reagent

Exosome were isolated using the Invitrogen Total Exosome Isolation Reagent from Serum (PR). 10 µL of reagent was mixed with 50 µL of human serum using gentle pipetting until the solution turned slightly opaque. The resulting mix was incubated at 4°C for 1 hour and then spun in a benchtop centrifuge at 10,000 ×g for 10 minutes. The

supernatant was discarded, and the resulting pellet was resuspended in 50 μL of 1× PBS. To increase purity, the reagent protocol was performed a second time on the previously purified sample. This resulted in two pelleting and resuspension steps in total and is referred to as the double precipitation sample while the single pelleting protocol is called the single precipitation sample. The sample is considered a single precipitation sample unless explicitly stated otherwise.

4.2.7 - Bicinchoninic acid assay

Bicinchoninic acid assay (BCA) was performed to quantify total protein of a solution using the BCA Protein Assay Kit of the Micro BCA Protein Assay Kit from Thermo Fisher Scientific. Samples were done in triplicate on a 96 well plate using the micro format protocol listed in the manual using a BSA standard curve. Briefly, 200 μL of activated reagent and 25 μL of sample is added to the well. After incubation at 37C for 45 minutes, the plate is imaged using a Biotek Synergy 2 well plate reader at 562 nm.

4.2.8 - Dot-Blot Assay

The dot blot apparatus was set up per instruction manual. Briefly, a hydrated NC membrane was sandwiched between the two outer trays and a filter sheet. The apparatus was washed 3 times with 1× PBS using a gentle vacuum. The plate was used right after hydration and washing. The samples were pipette directly from the fractionated tubes and allowed to incubate for 30 minutes before being allowed to filter through the membrane under gentle vacuum over 5-10 minutes. After samples were bound to the membrane, the apparatus was disassembled, and the membrane transferred to the imaging plate of the LI-

COR Odyssey FC Imager. Two dyes were detected at 680 and 800 nm. The plating was done in triplicate and error is reported as the standard deviation of the triplicate well assay.

4.2.9 - Biotinylating Primary IgG

Mouse antihuman-CD63 was biotinylated with the EZ-link biotin reagent using a 20-molar excess on a 2 mg/mL solution of IgG in PBS. After 30 minutes, the IgG was filtered of biotin reagent using a 30 kDa Amicon ultra- 0.5 centrifuge filter and resuspended in 1× PBS. The IgG was tested for biotin using the Pierce™ Biotin Quantitation Kit. The resulting 1 mg/mL IgG solution was aliquoted and stored at -80°C.

4.2.10 - Conjugated IgG LOD and LOQ

1 µg of exosome standards were adsorbed to the NC membrane in the dot blot apparatus. The membrane was removed and blocked by 3% BSA. The membrane was removed from the dot-blot apparatus and incubated in 500 ng/mL bio-anti-CD63 solution under gentle agitation to selectively label the exosomes. After 1 hr at room temp, the membrane was placed into a solution containing 10 ng/mL streptavidin-HRP. The membrane was incubated for 1 hour at room temp with gentle shaking. The membrane was washed 3× times with decreasing concentrations of PBS (3×, 1× and 0.1×). After the final wash, the membrane was dried of excess solution and placed in a minimal amount of chemiluminescent substrate (0.1 mL per cm^2). After 5 minutes, the sheet was imaged for 30 seconds in the LICOR instrument, and the protein spots were quantified and correspond to the wells of the dot-blot apparatus.

4.3 - Results and Discussion

4.3.1 - AF4 Serum Separation

Figure 4.3 shows the total particle and size mode for each minute fraction collected for the separation of exosome standards using the exponential cross flow program. NTA starts to detect particles at 12 minutes and reaches the apex at 16 minutes. We can also see a linear increase of size as the elution continues once enough particles were eluted to provide a good determination of the distribution. Without enough particles detected, as seen from 5 minutes to 12 minutes region, the size mode is random as only a few background particles are measured. Only fractions above 10 minutes are detectable by NTA. Exosome standards showed a steady increase over the separation reaching up to 200 nm in size, but our previous work indicates this larger size could be artifacts of the exosome standard purification process compared to the expected size of vesicles in serum.

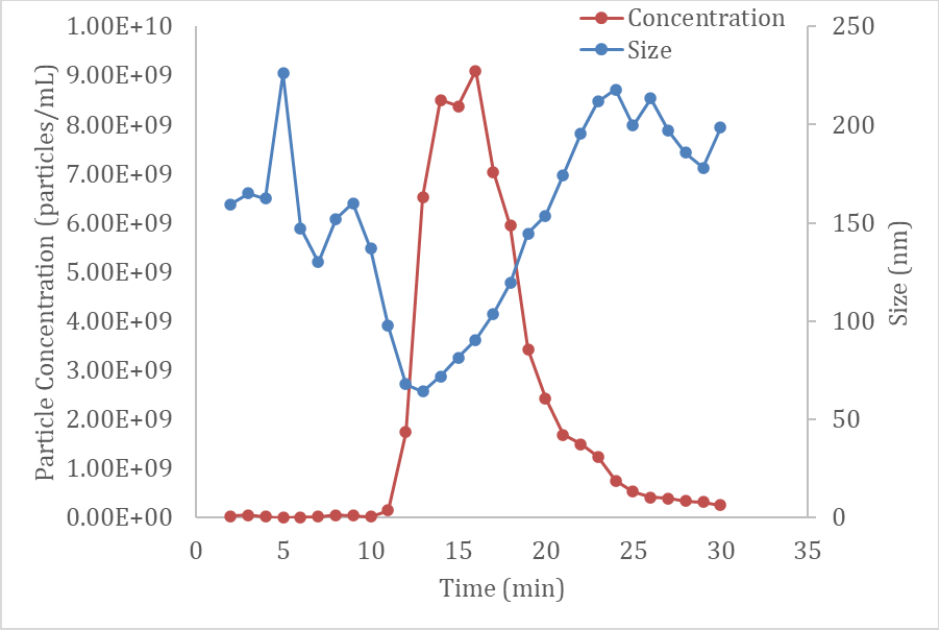

Figure 4.3 - Exosome standards ran in AF4 and quantified by offline NTA.

4.3.2 - Yield Recovery Comparison

AF4 recovery and purity were compared to the other common techniques for isolating exosomes from serum or cell culture medium. Table 4.1 shows the tabulated results from all the experiments performed. When evaluating AF4 it is important to note AF4 only needs to be successful at enriching exosomes to a high enough purity and concentration that protein and NTA analysis is possible. AF4 is not designed to be the best purifying instrument and thus is not expected to be, however it's used as a pseudo on-line purifying method and should be comparable. Each method requires different volumes of serum for purification (100 µL UC; 25 µL AF4, 50 µL PR) so each result was normalized to 100 µL for comparison. Each fraction recovered was converted to total particles from particles/mL to normalize the recovered particles from the different volumes recovered from the different methods used. AF4 was quantified from 12 minutes to 26 minutes based on Figure 3 showing the elution window of exosomes. Particles and protein were recovered earlier than 12 minutes, but this region will contain large amounts of soluble protein and is poorly enriched. The particle recovery of AF4 was superior to UC regardless of which cushioning strategy was attempted, but still was not as efficient as PR. Protein recovery showed similar trends with AF4 obtaining over 10× more protein than UC but was still less than PR by almost the same magnitude. The single precipitated PR showed large amounts of protein collected, but less than half of that amount was retained after the second precipitation indicating that a large portion were coeluted soluble proteins and protein aggregates.

Table 4.1 - Recovery results from the different isolation methods normalized to 100 µL of serum.

Isolation Method	Particles Recovered (total particles)	Protein Recovery (ug)	Protein per Particle (ug/particle)	Size Mode (nm)
50:20	**7.95E+08**	**16.10**	**2.03E-08**	**107.4**
50:10	**6.27E+08**	**8.13**	**1.30E-08**	**121.1**
40:20	**5.67E+08**	**8.95**	**1.58E-08**	**96.9**
40:10	**5.89E+08**	**8.57**	**1.45E-08**	**120.2**
Single Precipitation	**6.40E+10**	**1619**	**2.53E-08**	**85.4**
Double Precipitation	**7.42E+10**	**659**	**8.88E-09**	**89.2**
AF4 (after 12 minutes)	**9.17E+09**	**183**	**1.99E-08**	**93.9**

The recovery of UC was poor, but the volume of serum was low in comparison to the volumes normally done. UC was 1 order of magnitude less than AF4 for recovery of particles and 2 orders of magnitude under the PR method. The protein/particle of recovered vesicles the lowest besides the double precipitated PR sample. Figure 4.4 shows a diagram showing different UC pelleting strategies using no cushion, a single cushion layer, and a stripping + cushion layer. The pelleting strategy used was to increase purity and recovery. The cushion provides a liquid wall for the BioNP to compress against instead of a solid tube wall. Vesicles are low in density (1.09 to 1.15 g/mL) and would be buoyed by the

cushion layer and be retained at the boundary of the cushion and stripping layer. The stripping layer serves as a density filter because any compound with a lighter density than the stripping layer will be retained in the boundary between the sample plug and the stripping layer. The resulting pellet is an enriched BioNP sample that is within a density range. Four separate mixtures of iodixanol % layers were tested to minimize coprecipitation of aggregates, proteins, and debris and reduce sample loss due to pelleting. The four mixtures tested were 50:10, 50:20, 40:10, 40:20 cushion: stripping iodixanol percentage layers. The other advantage to this type of method is that process of pelleting against a firm wall can lead to increased sample loss from irreversible adsorption to the tube wall. Using a wall of slightly higher density allows more flexibility in the retention region and has a much higher surface area where the pellet forms because the sample is not forced into the smallest region of the coned tube. This gives more room for the exosome pellet to expand out from the repulsive forces created by the negative charge of the vesicles and could reduce aggregation and fusion. These benefits provide a better system of recovery over the common pelleting methods commonly used and would give the best-case recovery of an ultracentrifuge pelleting method. The downfall is the background iodixanol solution, which is removed by a secondary ultracentrifuge step that uses the standard pelleting method against a coned tube wall.

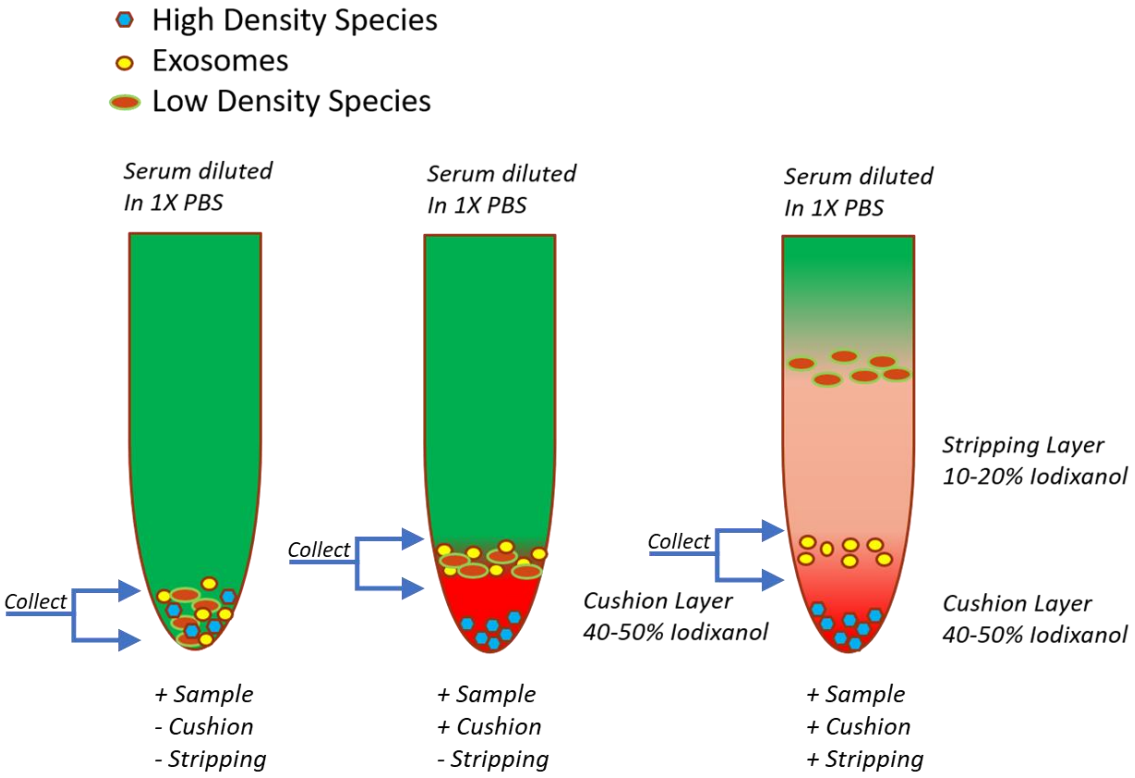

Figure 4.4 - Different UC pelleting strategies using varying density layers to enrich vesicles within a density range.

The PR isolation method was used as a high recovery method that clears >95% of the exosomes in sample based on commercial product information and previous group results. The PR method showed high recovery of both protein and particles. The protein/particle indicate the first pelleting was crude while the second pelleting cleared a large amount of background protein but did not have any loss in particles. The reagent utilizes osmotic dehydration of the exosomes, which temporarily dehydrates the vesicles using osmolyte additives in the surrounding medium, which is then removed upon resuspension of the pellet. One drawback to PR is that it has shown decreased antibody affinity to exosome biomarkers which could be due to surface protein aggregation or

protein unfolding due osmotic balance shifts in the medium. However, this method has shown great yields, simple process, and consistent product performance from serum and cell culture medium and the high recovery overcomes the reduced antibody affinity.

4.3.3 - Hydrodynamic Diameter of Recovered Particles

One noticeable difference is the size average between the UC and other methods. PR samples showed very consistent size regardless of the number of times precipitated. The dehydration would cause shrinkage but regained when normal osmotic balance is restored, and rehydration occurs. Normal exosome sizes are generally considered around 100 nm, but many factors can influence this from so some variation can be expected when evaluating donor serum. The size average of UC was much larger than PR and AF4 showing 107.4, 121.1, 96.9 and 120.2 nm when the other methods were 90 nm in size. This matches previous reports of fusion and aggregation in UC and is expected to be from the isolation itself. AF4 measured slightly higher at 93.9 nm than PR at 85.4 and 89.2 nm for single and double. AF4 has no selectivity towards bilayer membranes like the PR method does and will collect any particle within the size separation window (50-150 nm) and it is possible AF4 collected some additional protein aggregates within the fractions, and this may shift the average slightly. However, the distributions of UC samples showed large particles that were not seen in AF4 or UC and further indicate fusion and aggregation occurred.

4.3.4 - Purity Estimation

A way to compare purity performance is the protein/particle ratio. Protein aggregates and small lipoproteins have higher amounts of protein per particle than a hollow

BioNP with a bilayer membrane. The protein per particle ratio is not a standard value but a relative measure of how much protein content is loaded in each particle. Bilayer membrane particles have hollow cores with mRNA, peptide, and metabolites occupying the cargo space with spaced out receptor proteins on the surface. There would be differences in particle subtypes where particles may be composed primarily of protein, or a hybrid structure like a lipoprotein that has a fat bound to the hydrophobic units of the structure forming proteins. Generally, the lowest amount of protein/particle would be a bilayer membrane vesicle such as exosome or microvesicle. A good display of this is the single and double precipitated PR samples. A slight increase in the particle count was observed after the second precipitation, but considering the sample has additional processing steps of centrifugation and resuspension, it is expected that variation in NTA is seen. The increase to 7.42E+10 from 6.40E+10 was small compared to the decrease in protein from 1619 to 659 µg for the single and double PR respectively, and this caused a large swing the protein/particle ratio from 2.53E-08 to 8.88E-09 respectively.

The double PR method had protein/particle on the scale of 10^{-9} µg/particle and no other method was able to reach that low of a ratio. All other methods were very close to each other in value. This value also helps show that the 50:20 cushion method that resulted in 2× the protein amount only showed a slight increase in particles, which indicates this may have been mostly coeluted proteins instead of a better cushioning method. AF4 compares well to single PR, which is the standard protocol for the reagent. The double PR is only done when trying to ensure purity is as high as possible. The cost of the reagent is very high compared to the consumables of the other methods so doubling this cost it makes

this method even less economical. AF4 fairs slightly higher than UC on the purity scale with a 1.99E-08 ratio, but the value is close to UC's average of 1.59E-08. AF4 can provide similar performance in purification from a complex matrix but can provide size separation and the capability of online detection.

One of the advantages of the protein/particle ratio is it can help determine possible populations in the fractionated sample. Serum is a complex mixture of multiple populations, and the protein/particle can help identify the location enriched exosomes are being eluted. Figure 4.5 shows the protein/particle ratio for each fraction as the separation occurred. Early in the separation, the eluted protein amount is very high as this is a combination of soluble proteins, small vesicles, aggregates, and lipoproteins. This ratio drops steeply until 13 minutes, when it stabilizes. This coincides with the exosome elution window, but this is more a product of when the soluble proteins and protein aggregates have finished eluting from the channel. The fractogram can help identify when in the method the background proteins stop eluting, thus ensuring the collected fractions are not heavily contaminated. A peak can be seen at 22 minutes which shows a protein/particle ratio that doubles which indicates a protein aggregate or other population of protein rich BioNP may be present with the vesicles eluted.

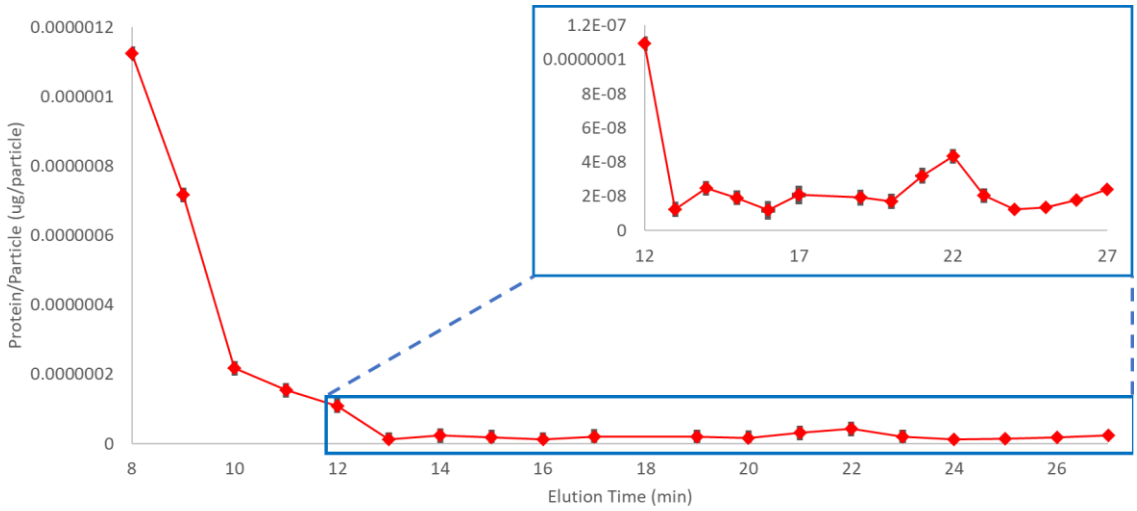

Figure 4.5 - Protein/particle ratio for each minute fraction the AF4 eluent of human serum. The earlier fractions (8-12 minutes) still contain large amounts of soluble proteins and protein aggregates. Error bars are taken as the variation of the BCA quantity divided by the number of particles, providing the variance in µg/particle.

4.3.5 - In-Situ Labeling

AF4 channel design and size separation allow BioNPs to be washed of unbound probes while being separated. This can be exploited to develop in-channel labeling techniques to save time and resources for the downstream analysis. Small probes can be washed through the channel membrane while larger probes can be size separated from the larger BioNPs. To test this, commercial labeling systems utilizing a rabbit model primary against CD63 with an anti-mouse secondary labeled with a 700 nm NIR dye and a mouse model primary against apolipoprotein-B with a goat anti-rabbit with 800 nm dye were used as the two detection systems in a duplex format allowing two proteins per fraction to be quantified. These commercial systems have been well characterized and should perform well in standard WBs and our modified dot-blot.

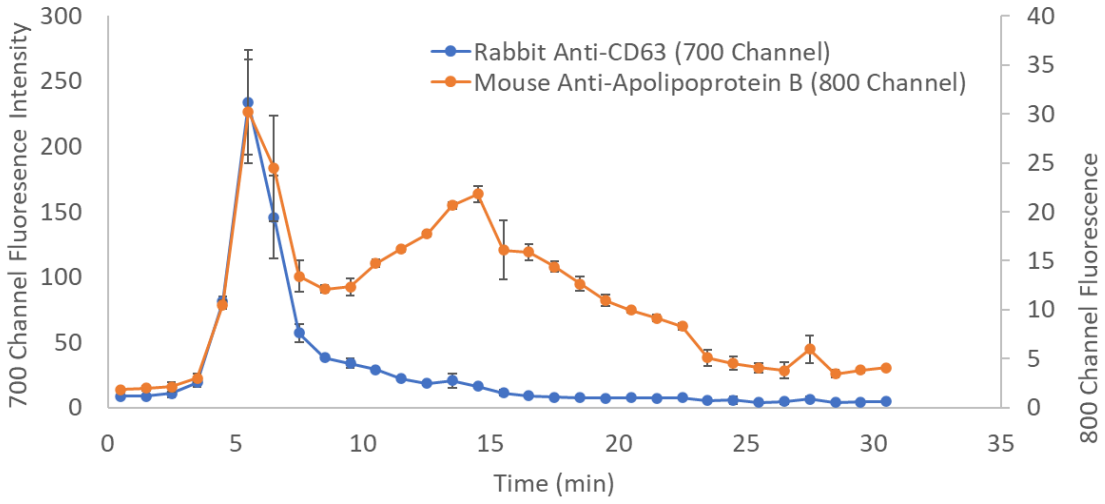

Figure 4.6 - Probe signal intensity fractogram of apolipoprotein-B and BSA. The primary and secondary IgG were added directly before injection. CD63 was not found on the lipoprotein surface and does not label the LDL particles.

Specificity was tested using a mock medium with only BSA and lipoproteins with the spiked in probes. The CD63 probe should not bind to the lipoproteins because CD63 is not present on lipoproteins. The mock medium and probes were injected and separated with AF4 and quantified with the dot-blot assay. To allow probe binding time, focusing time was increased to 15 minutes from 7 minutes. Figure 4.6 Shows the fractogram showing the signal intensity for each fraction. The rabbit primary targets CD63, which is absent on lipoproteins and no labeling of the lipoproteins was observed. In contrast, the specific labeling of apolipoprotein-B is carried with the BioNPs throughout the run. This shows promise that AF4 is not forcing non-specific adsorption and the washing effect is strong enough to remove unbound probes from the surface of the BioNPs. We also show specific labeling of surface antigens can be done in channel during the focusing step without the need of any additional steps or processing.

The mock medium was neat with only BSA to add bulk soluble protein, but serum contains proteases and increased inhibition from protein-protein interactions so labeling may not be efficient or effective with a complex matrix. Figure 4.7 shows human serum labeled with rabbit anti-CD63 and mouse anti-CD81. A few different peaks are identified in the fractogram and both CD63 and CD81 showed the same peak pattern, however the relative peak intensities do show differences between CD63 and CD81, especially in the 3rd peak seen at 18 minutes. This variable intensity for the same populations could mean subpopulations of exosomes may be present that have different expression levels of CD63 and CD81. This has been hypothesized in others work as well. The overall intensity is arbitrary as the detection limits of the different channels and dyes are different along with the different binding affinities of the different antibody systems, but the different ratios of peak area do indicate differences of protein amount. The elution window of all 3 peaks falls within the expected elution window of exosomes, but the polyclonal detection system used in these assays are not ideal for the separation. A primary is usually monoclonal and produced to have a specific interaction with one antigen, but the secondary is produced in an animal using full length IgG of the target primary. This generates polyclonal antibody systems where multiple secondaries bind to a single primary. These larger probe complexes add more signal per antigen, but also add bulkiness to the probe, which causes longer elution times. Figure 4.7 shows the unbound probes, and the bound exosomes overlap, and the quantification of the protein/particle ratio would be skewed. This is somewhat magnified with the rabbit, which showed better polyclonal binding because the

size of the probe complex is larger than the mouse model, and thus causes more overlap with the peaks. The polyclonal binding combined with natural antibody aggregation creates probe complexes too large for separation from exosomes.

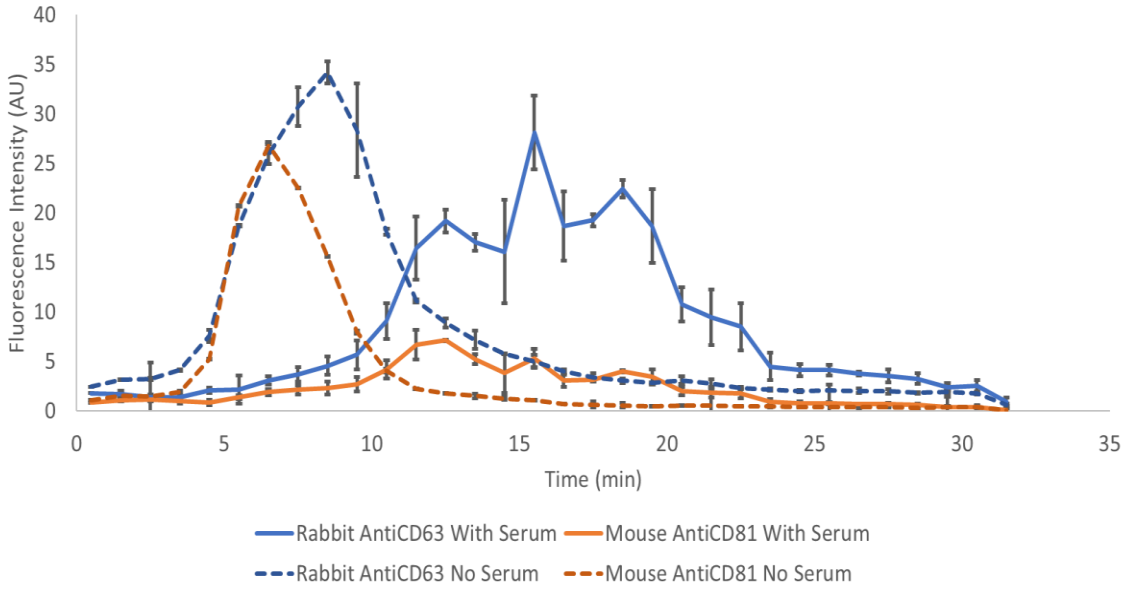

Figure 4.7 - Fractograms of serum labeled with anti-CD63 and anti-CD81 antibodies. The without serum was performed with mock medium and shows where the unbound probes elute.

4.4 - Future Outlooks

AF4-NTA was designed solely for this type of vesicle analysis because of the sample reduction and efficient biological probing. This project was delayed while validation of AF4-NTA was being done, with the goal of returning to design a better probe system once AF4-NTA recovery of exosomes was established, and the fraction particle concentration ranges were determined. New probes in our lab as well as custom conjugations to primaries could allow us better control over the probe size and signal intensities, allowing us to tune the probe performance to AF4-NTA but the COVID-19

pandemic caused lab shutdowns and supply chain issues that ended a lot of research during this time. Because of this, the future outlooks section of this chapter is slightly longer due to the future ideas for the final probe.

4.4.1 - Single Antibody System

The best route to improve the detection scheme is to reduce probe hydrodynamic size, thus increasing the separation between the unbound probes and the eluted exosomes. The fractions collected by the AF4-NTA system would be a narrow concentration range due to the narrow concentration range NTA operates at. The fractions will also be dilute. A successful detection scheme should be adaptable to a simple well plate or dot blot apparatus and work with smaller volumes so it can be done in replicates with a single run. The easiest adjustment to the current setup is to label primary antibodies with the probes directly with biotin using EDC-NHS chemistry and attaching different signaling molecules to the primary. The NTA working range was determined to be 10^7 to 10^9 particles/mL and this range can be applied to the LOD and LOQ of different probes when converting protein mass to particle counts. Horseradish peroxidase (HRP) works well as a single signaling molecule as the enzyme continuously catalyzes light emitting reactions, which can enhance the detection a low concentration of probes.

Figure 4.8 shows the standard curve using standard exosomes and HRP labeled anti-cd63. The curve was converted into particle counts using particle counts measured by NTA of the stock material and the dilution factor used to make the standard curve. Both the exosome standard's protein mass and particle counts were evaluated for the LOD and LOQ (Table Inset of Figure 4.8). The protein mass needed for detection was 10.8 ng while

33.0 ng was needed for quantification. In terms of particle counts, LOD was measured as 9.79E+06 particles and the LOQ was recorded as 2.97E+07. While this probe shows promise because these limits work within the AF4-NTA limits, it would not be quantifiable in all fractions where a lower number of exosomes are recovered.

The other consideration is the LOQ was calculated in total particles adsorbed to the membrane (assuming 100% binding efficiency) and not from concentration. The LOQ converted to particle/mL is 5.94E+07 particles/mL if the fraction was 500 µL and 1.18E+08 particles/mL if the fractions were 250 uL. The fraction volume varies between 0.5-1.0 mL in typical AF4 separations performed in this dissertation. It can be estimated that the total particle LOQ ideal for AF4-NTA would be 5.0E+06 total particles. That would result in a 500 µL fraction having an LOQ of 1.0E+07 particles/mL. This LOQ would align the LOQ of the NTA detector with the LOQ of the dot blot apparatus.

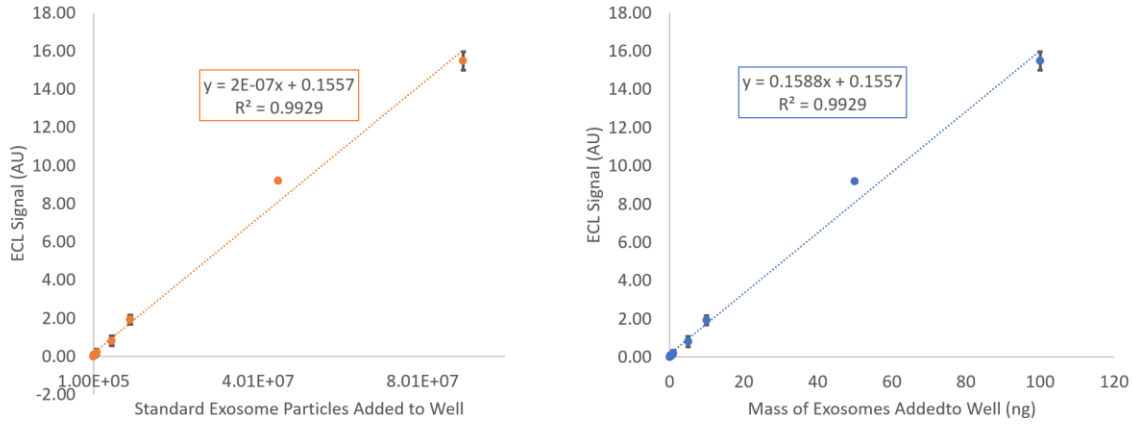

Biotinylated Primaries Post Channel Detection		
Exo Mass (ng)	LOD	10.9
	LOQ	33.0
Exo Particle Count (particles)	LOD	9.79E+06
	LOQ	2.97E+07
Protein/Particle Ratio	(ug/particle)	1.11E-10

Figure 4.8 - LOD and LOQ quantification curves for protein amount and particle counts.

4.4.2 - Aptamer Probes

The most promising probes for AF4-NTA are aptamers.[58–60] Our lab's previous work displayed a SELEX method for aptamer development[61] and evaluated aptamer-protein interactions[57] and the small size of the oligonucleotide allows better diffusion in the focusing region, and thus would increase probe interactions with the binding antigen over bulkier IgG probes. The small size also decreases the retention time and allows a bigger baseline separation between the unbound probes and the eluted exosomes. Aptamers are easily synthesized with custom designs that allow attachment of several dyes and cost much cheaper than antibodies. This allows more versatility in signal selection and better suited for in-channel labeling applications.

Another benefit of an aptamer design is the ability to use amplification techniques.[62–68] An aptamer can be designed to open when it binds to CD63 to expose an initiating sequence that binds to a hairpin sequence (H1) that opens and binds a second hairpin sequence (H2). The opened H2 sequence can then bind and open the H1 sequence, and the cycle repeats until the chain reaction is stopped. Our recent work in Biosensors and Bioelectronics grows nanostructures on the surface antigens of exosomes using similar designs.[69] Our lab has experience in other polymerase chain reaction analysis for exosome miRNA[70,71] as well as isothermal amplification techniques that could be modified to work with the initiator sequence of the aptamer.[72] The advantage to these types of strategies is the degree of amplification is controlled by reaction time or thermocycles allowing some control over the LOQ of the design. Aptamer based probes can be tuned to have a linear range within the working range of AF4-NTA.

4.5 - Conclusion

Isolating vesicles and exosomes from serum or cell culture medium with AF4 does compare with other isolation techniques and can successfully enrich the fractions with BioNPs and separate the soluble proteins and metabolites. The gentle nature separates exosomes in a native state and does not seem to cause fusion or aggregation like UC is prone to. The ability to isolate exosomes from serum adds function to AF4 than the other techniques considering the detector capability. The detection scheme should work within the analytical limits of AF4-NTA and be adaptable to recovery volume and yields. Highly sensitive detection schemes are needed due to the narrow limits of NTA. AF4's ability to wash BioNPs of unbound probes makes the downstream processing much simpler and can reduce the overall processing time from days to hours by eliminating the binding, blocking, washing, and imaging steps needed in a traditional protocol for a dot blot assay. AF4 shows great promise in developing a labeling, characterization, and detection strategy for surface proteins of BioNPs. Using this in combination of AF4-NTA allows the protein data to be directly related to the particle counts in the solution. This creates a "snapshot" that gives particle counts, particle size, and protein signal intensity for 2 surface biomarkers. These signal/particle ratios indicate how much protein may be found on the surface. The speed at which this assay can be performed make it excellent for any application where exosome secretion rates, exosome expression levels, or changes in exosome populations are needed to be analyzed on a frequent basis.

4.6 - References

(1) Zhu, Y.; Pick, H.; Gasilova, N.; Li, X.; Lin, T.-E.; Laeubli, H. P.; Zippelius, A.; Ho, P.-C.; Girault, H. H. MALDI Detection of Exosomes: A Potential Tool for Cancer Studies. *Chem* **2019**, *5* (5), 1318–1336. https://doi.org/10.1016/j.chempr.2019.04.007.

(2) Braicu, C.; Tomuleasa, C.; Monroig, P.; Cucuianu, A.; Berindan-Neagoe, I.; Calin, G. A. Exosomes as Divine Messengers: Are They the Hermes of Modern Molecular Oncology? *Cell Death Differ.* **2015**, *22* (1), 34–45. https://doi.org/10.1038/cdd.2014.130.

(3) Whiteside, T. L. The Potential of Tumor-Derived Exosomes for Noninvasive Cancer Monitoring: An Update. *Expert Rev. Mol. Diagn.* **2018**, *18* (12), 1029–1040. https://doi.org/10.1080/14737159.2018.1544494.

(4) Duijvesz, D.; Burnum-Johnson, K. E.; Gritsenko, M. A.; Hoogland, A. M.; Berg, M. S. V. den; Willemsen, R.; Luider, T.; Paša-Tolić, L.; Jenster, G. Proteomic Profiling of Exosomes Leads to the Identification of Novel Biomarkers for Prostate Cancer. *PLOS ONE* **2013**, *8* (12), e82589. https://doi.org/10.1371/journal.pone.0082589.

(5) Brinton, L. T.; Sloane, H. S.; Kester, M.; Kelly, K. A. Formation and Role of Exosomes in Cancer. *Cell. Mol. Life Sci.* **2015**, *72* (4), 659–671. https://doi.org/10.1007/s00018-014-1764-3.

(6) Barile, L.; Vassalli, G. Exosomes: Therapy Delivery Tools and Biomarkers of Diseases. *Pharmacol. Ther.* **2017**, *174*, 63–78. https://doi.org/10.1016/j.pharmthera.2017.02.020.

(7) Christianson, H. C.; Svensson, K. J.; Kuppevelt, T. H. van; Li, J.-P.; Belting, M. Cancer Cell Exosomes Depend on Cell-Surface Heparan Sulfate Proteoglycans for Their Internalization and Functional Activity. *Proc. Natl. Acad. Sci.* **2013**, *110* (43), 17380–17385. https://doi.org/10.1073/pnas.1304266110.

(8) Blomme, A.; Fahmy, K.; Peulen, O.; Costanza, B.; Fontaine, M.; Struman, I.; Baiwir, D.; de Pauw, E.; Thiry, M.; Bellahcène, A.; Castronovo, V.; Turtoi, A. Myoferlin Is a Novel Exosomal Protein and Functional Regulator of Cancer-Derived Exosomes. *Oncotarget* **2016**, *7* (50), 83669–83683. https://doi.org/10.18632/oncotarget.13276.

(9) Zhang, Y.; Liu, Y.; Liu, H.; Tang, W. H. Exosomes: Biogenesis, Biologic Function and Clinical Potential. *Cell Biosci.* **2019**, *9*, 19. https://doi.org/10.1186/s13578-019-0282-2.

(10) Asada, H.; Tomiyasu, H.; Uchikai, T.; Ishihara, G.; Goto-Koshino, Y.; Ohno, K.; Tsujimoto, H. Comprehensive Analysis of MiRNA and Protein Profiles within Exosomes Derived from Canine Lymphoid Tumour Cell Lines. *PLOS ONE* **2019**, *14* (4), e0208567. https://doi.org/10.1371/journal.pone.0208567.

(11) Jakobsen, N. A.; Hamdy, F. C.; Bryant, R. J. Novel Biomarkers for the Detection of Prostate Cancer. *J. Clin. Urol.* **2016**, *9* (2 Suppl), 3–10. https://doi.org/10.1177/2051415816656121.

(12) György, B.; Szabó, T. G.; Pásztói, M.; Pál, Z.; Misják, P.; Aradi, B.; László, V.; Pállinger, É.; Pap, E.; Kittel, Á.; Nagy, G.; Falus, A.; Buzás, E. I. Membrane Vesicles, Current State-of-the-Art: Emerging Role of Extracellular Vesicles. *Cell. Mol. Life Sci.* **2011**, *68* (16), 2667–2688. https://doi.org/10.1007/s00018-011-0689-3.

(13) Erozenci, L. A.; Böttger, F.; Bijnsdorp, I. V.; Jimenez, C. R. Urinary Exosomal Proteins as (Pan-)Cancer Biomarkers: Insights from the Proteome. *FEBS Lett.* **2019**, *593* (13), 1580–1597. https://doi.org/10.1002/1873-3468.13487.

(14) Lorenc, T.; Klimczyk, K.; Michalczewska, I.; Słomka, M.; Kubiak-Tomaszewska, G.; Olejarz, W. Exosomes in Prostate Cancer Diagnosis, Prognosis and Therapy. *Int. J. Mol. Sci.* **2020**, *21* (6), 2118. https://doi.org/10.3390/ijms21062118.

(15) D'Souza-Schorey, C.; Clancy, J. W. Tumor-Derived Microvesicles: Shedding Light on Novel Microenvironment Modulators and Prospective Cancer Biomarkers. *Genes Dev.* **2012**, *26* (12), 1287–1299. https://doi.org/10.1101/gad.192351.112.

(16) Skotland, T.; Sandvig, K.; Llorente, A. Lipids in Exosomes: Current Knowledge and the Way Forward. *Prog. Lipid Res.* **2017**, *66*, 30–41. https://doi.org/10.1016/J.PLIPRES.2017.03.001.

(17) Lässer, C.; Eldh, M.; Lötvall, J. Isolation and Characterization of RNA-Containing Exosomes. *JoVE J. Vis. Exp.* **2012**, No. 59, e3037. https://doi.org/10.3791/3037.

(18) Nilsson, J.; Skog, J.; Nordstrand, A.; Baranov, V.; Mincheva-Nilsson, L.; Breakefield, X. O.; Widmark, A. Prostate Cancer-Derived Urine Exosomes: A Novel Approach to Biomarkers for Prostate Cancer. *Br. J. Cancer* **2009**, *100* (10), 1603–1607. https://doi.org/10.1038/sj.bjc.6605058.

(19) Tamkovich, S. N.; Yunusova, N. V.; Stakheeva, M. N.; Somov, A. K.; Frolova, A. Y.; Kirushina, N. A.; Afanasyev, S. G.; Grigoryeva, A. E.; Laktionov, P. P.; Kondakova, I. V. [Isolation and Characterization of Exosomes from Blood Plasma of Breast Cancer and Colorectal Cancer Patients]. *Biomeditsinskaia Khimiia* **2017**, *63* (2), 165–169.

(20) Huang, T.; Deng, C.-X. Current Progresses of Exosomes as Cancer Diagnostic and Prognostic Biomarkers. *Int. J. Biol. Sci.* **2019**, *15* (1), 1–11. https://doi.org/10.7150/ijbs.27796.

(21) Paulaitis, M.; Agarwal, K.; Nana-Sinkam, P. Dynamic Scaling of Exosome Sizes. *Langmuir ACS J. Surf. Colloids* **2018**, *34* (32), 9387–9393. https://doi.org/10.1021/acs.langmuir.7b04080.

(22) Whiteside, T. L. Tumor-Derived Exosomes and Their Role in Cancer Progression. *Adv. Clin. Chem.* **2016**, *74*, 103–141. https://doi.org/10.1016/bs.acc.2015.12.005.

(23) Aubertin, K.; Silva, A. K. A.; Luciani, N.; Espinosa, A.; Djemat, A.; Charue, D.; Gallet, F.; Blanc-Brude, O.; Wilhelm, C. Massive Release of Extracellular Vesicles from Cancer Cells after Photodynamic Treatment or Chemotherapy. *Sci. Rep.* **2016**, *6* (1), 35376. https://doi.org/10.1038/srep35376.

(24) Johnsen, K. B.; Gudbergsson, J. M.; Andresen, T. L.; Simonsen, J. B. What Is the Blood Concentration of Extracellular Vesicles? Implications for the Use of Extracellular Vesicles as Blood-Borne Biomarkers of Cancer. *Biochim. Biophys. Acta BBA - Rev. Cancer* **2019**, *1871* (1), 109–116. https://doi.org/10.1016/j.bbcan.2018.11.006.

(25) Bebelman, M. P.; Smit, M. J.; Pegtel, D. M.; Baglio, S. R. Biogenesis and Function of Extracellular Vesicles in Cancer. *Pharmacol. Ther.* **2018**, *188*, 1–11. https://doi.org/10.1016/j.pharmthera.2018.02.013.

(26) Lobb, R. J.; Becker, M.; Wen, S. W.; Wong, C. S. F.; Wiegmans, A. P.; Leimgruber, A.; Möller, A. Optimized Exosome Isolation Protocol for Cell Culture Supernatant and Human Plasma. *Journal of Extracellular Vesicles*. July 17, 2015.

(27) Li, P.; Kaslan, M.; Lee, S. H.; Yao, J.; Gao, Z. Progress in Exosome Isolation Techniques. *Theranostics* **2017**, *7* (3), 789–804. https://doi.org/10.7150/thno.18133.

(28) Weng, Y.; Sui, Z.; Shan, Y.; Hu, Y.; Chen, Y.; Zhang, L.; Zhang, Y. Effective Isolation of Exosomes with Polyethylene Glycol from Cell Culture Supernatant for In-Depth Proteome Profiling. *The Analyst* **2016**, *141* (15), 4640–4646. https://doi.org/10.1039/c6an00892e.

(29) Van Deun, J.; Mestdagh, P.; Sormunen, R.; Cocquyt, V.; Vermaelen, K.; Vandesompele, J.; Bracke, M.; De Wever, O.; Hendrix, A. The Impact of Disparate Isolation Methods for Extracellular Vesicles on Downstream RNA Profiling. *J. Extracell. Vesicles* **2014**, *3*. https://doi.org/10.3402/jev.v3.24858.

(30) Zlotogorski-Hurvitz, A.; Dayan, D.; Chaushu, G.; Korvala, J.; Salo, T.; Sormunen, R.; Vered, M. Human Saliva-Derived Exosomes: Comparing Methods of Isolation. *J. Histochem. Cytochem.* **2015**, *63* (3), 181–189. https://doi.org/10.1369/0022155414564219.

(31) Patel, G. K.; Khan, M. A.; Zubair, H.; Srivastava, S. K.; Khushman, M.; Singh, S.; Singh, A. P. Comparative Analysis of Exosome Isolation Methods Using Culture Supernatant for Optimum Yield, Purity and Downstream Applications. *Sci. Rep.* **2019**, *9* (1). https://doi.org/10.1038/s41598-019-41800-2.

(32) Gupta, S.; Rawat, S.; Arora, V.; Kottarath, S. K.; Dinda, A. K.; Vaishnav, P. K.; Nayak, B.; Mohanty, S. An Improvised One-Step Sucrose Cushion Ultracentrifugation Method for Exosome Isolation from Culture Supernatants of Mesenchymal Stem Cells. *Stem Cell Res. Ther.* **2018**, *9* (1), 180. https://doi.org/10.1186/s13287-018-0923-0.

(33) Cvjetkovic, A.; Lötvall, J.; Lässer, C. The Influence of Rotor Type and Centrifugation Time on the Yield and Purity of Extracellular Vesicles. *J. Extracell. Vesicles* **2014**, *3* (1), 23111. https://doi.org/10.3402/jev.v3.23111.

(34) Helwa, I.; Cai, J.; Drewry, M. D.; Zimmerman, A.; Dinkins, M. B.; Khaled, M. L.; Seremwe, M.; Dismuke, W. M.; Bieberich, E.; Stamer, W. D.; Hamrick, M. W.; Liu, Y. A Comparative Study of Serum Exosome Isolation Using Differential Ultracentrifugation and Three Commercial Reagents. *PLOS ONE* **2017**, *12* (1), e0170628. https://doi.org/10.1371/journal.pone.0170628.

(35) Tauro, B. J.; Greening, D. W.; Mathias, R. A.; Ji, H.; Mathivanan, S.; Scott, A. M.; Simpson, R. J. Comparison of Ultracentrifugation, Density Gradient Separation, and Immunoaffinity Capture Methods for Isolating Human Colon Cancer Cell Line LIM1863-Derived Exosomes. *Methods* **2012**, *56* (2), 293–304. https://doi.org/10.1016/j.ymeth.2012.01.002.

(36) Li, K.; Wong, D. K.; Hong, K. Y.; Raffai, R. L. Cushioned–Density Gradient Ultracentrifugation (C–DGUC): A Refined and High Performance Method for the Isolation, Characterization & Use of Exosomes. *Methods Mol. Biol. Clifton NJ* **2018**, *1740*, 69–83. https://doi.org/10.1007/978-1-4939-7652-2_7.

(37) Pavani, K. C.; Hendrix, A.; Van Den Broeck, W.; Couck, L.; Szymanska, K.; Lin, X.; De Koster, J.; Van Soom, A.; Leemans, B. Isolation and Characterization of Functionally Active Extracellular Vesicles from Culture Medium Conditioned by Bovine Embryos In Vitro. *Int. J. Mol. Sci.* **2019**, *20* (1), 38. https://doi.org/10.3390/ijms20010038.

(38) Stübiger, G.; Nairn, M. D.; Abban, T. K.; Openshaw, M. E.; Mancera, L.; Herzig, B.; Wuczkowski, M.; Senfter, D.; Mader, R. M. MALDI-MS Protein Profiling of

Chemoresistance in Extracellular Vesicles of Cancer Cells. *Anal. Chem.* **2018**, acs.analchem.8b03756. https://doi.org/10.1021/acs.analchem.8b03756.

(39) Wang, Y.-M.; Liu, J.-W.; Adkins, G. B.; Shen, W.; Trinh, M. P.; Duan, L.-Y.; Jiang, J.-H.; Zhong, W. Enhancement of the Intrinsic Peroxidase-Like Activity of Graphitic Carbon Nitride Nanosheets by SsDNAs and Its Application for Detection of Exosomes. *Anal. Chem.* **2017**, *89* (22). https://doi.org/10.1021/acs.analchem.7b03335.

(40) Alix-Panabières, C.; Pantel, K. Circulating Tumor Cells: Liquid Biopsy of Cancer. *Clin. Chem.* **2013**, *59* (1), 110–118. https://doi.org/10.1373/clinchem.2012.194258.

(41) Pantel, K.; Alix-Panabières, C. Liquid Biopsy: Potential and Challenges. *Mol. Oncol.* **2016**, *10* (3), 371–373. https://doi.org/10.1016/j.molonc.2016.01.009.

(42) Ilié, M.; Hofman, P. Pros: Can Tissue Biopsy Be Replaced by Liquid Biopsy? *Transl. Lung Cancer Res.* **2016**, *5* (4), 420–423. https://doi.org/10.21037/tlcr.2016.08.06.

(43) Crowley, E.; Di Nicolantonio, F.; Loupakis, F.; Bardelli, A. Liquid Biopsy: Monitoring Cancer-Genetics in the Blood. *Nat. Rev. Clin. Oncol.* **2013**, *10* (8), 472–484. https://doi.org/10.1038/nrclinonc.2013.110.

(44) Chen, S.; Shiesh, S.-C.; Lee, G.-B.; Chen, C. Two-Step Magnetic Bead-Based (2MBB) Techniques for Immunocapture of Extracellular Vesicles and Quantification of MicroRNAs for Cardiovascular Diseases: A Pilot Study. *PLOS ONE* **2020**, *15* (2), e0229610. https://doi.org/10.1371/journal.pone.0229610.

(45) Zarovni, N.; Corrado, A.; Guazzi, P.; Zocco, D.; Lari, E.; Radano, G.; Muhhina, J.; Fondelli, C.; Gavrilova, J.; Chiesi, A. Integrated Isolation and Quantitative Analysis of Exosome Shuttled Proteins and Nucleic Acids Using Immunocapture Approaches. *Methods* **2015**, *87*, 46–58. https://doi.org/10.1016/j.ymeth.2015.05.028.

(46) Fang, S.; Tian, H.; Li, X.; Jin, D.; Li, X.; Kong, J.; Yang, C.; Yang, X.; Lu, Y.; Luo, Y.; Lin, B.; Niu, W.; Liu, T. Clinical Application of a Microfluidic Chip for Immunocapture and Quantification of Circulating Exosomes to Assist Breast Cancer Diagnosis and Molecular Classification. *PLOS ONE* **2017**, *12* (4), e0175050. https://doi.org/10.1371/journal.pone.0175050.

(47) Campos-Silva, C.; Suárez, H.; Jara-Acevedo, R.; Linares-Espinós, E.; Martinez-Piñeiro, L.; Yáñez-Mó, M.; Valés-Gómez, M. High Sensitivity Detection of Extracellular Vesicles Immune-Captured from Urine by Conventional Flow

Cytometry. *Sci. Rep.* **2019**, *9* (1), 2042. https://doi.org/10.1038/s41598-019-38516-8.

(48) Ladd Effio, C.; Oelmeier, S. A.; Hubbuch, J. High-Throughput Characterization of Virus-like Particles by Interlaced Size-Exclusion Chromatography. *Vaccine* **2016**, *34* (10), 1259–1267. https://doi.org/10.1016/j.vaccine.2016.01.035.

(49) Dhondt, B.; Geeurickx, E.; Tulkens, J.; Van Deun, J.; Vergauwen, G.; Lippens, L.; Miinalainen, I.; Rappu, P.; Heino, J.; Ost, P.; Lumen, N.; De Wever, O.; Hendrix, A. Unravelling the Proteomic Landscape of Extracellular Vesicles in Prostate Cancer by Density-Based Fractionation of Urine. *J. Extracell. Vesicles* **2020**, *9* (1), 1736935. https://doi.org/10.1080/20013078.2020.1736935.

(50) Akers, J. C.; Gonda, D.; Kim, R.; Carter, B. S.; Chen, C. C. Biogenesis of Extracellular Vesicles (EV): Exosomes, Microvesicles, Retrovirus-like Vesicles, and Apoptotic Bodies. *J. Neurooncol.* **2013**, *113* (1), 1–11. https://doi.org/10.1007/s11060-013-1084-8.

(51) Development of a Dot Blot Assay for the Rapid Detection of Central Nervous System Tissue on Meat and Contact Surfaces | Journal of Agricultural and Food Chemistry https://pubs.acs.org/doi/abs/10.1021/jf0718493 (accessed 2021 -07 -31).

(52) Wang, Y.; Li, D.; Ren, W.; Liu, Z.; Dong, S.; Wang, E. Ultrasensitive Colorimetric Detection of Protein by Aptamer–Au Nanoparticles Conjugates Based on a Dot-Blot Assay. *Chem. Commun.* **2008**, *0* (22), 2520–2522. https://doi.org/10.1039/B801055B.

(53) Ortega Ibarra, J. M.; Cifuentes-Castro, V. H.; Medina- Ceja, L.; Morales-Villagrán, A. Nano Dot Blot: An Alternative Technique for Protein Identification and Quantification in a High Throughput Format. *J. Neurosci. Methods* **2021**, *358*, 109194. https://doi.org/10.1016/j.jneumeth.2021.109194.

(54) Aoki, Y.; Kunimoto, M.; Shibata, Y.; Suzuki, K. T. Detection of Metallothionein on Nitrocellulose Membrane Using Western Blotting Technique and Its Application to Identification of Cadmium-Binding Proteins. *Anal. Biochem.* **1986**, *157* (1), 117–122. https://doi.org/10.1016/0003-2697(86)90204-6.

(55) Low, S. C.; Shaimi, R.; Thandaithabany, Y.; Lim, J. K.; Ahmad, A. L.; Ismail, A. Electrophoretic Interactions between Nitrocellulose Membranes and Proteins: Biointerface Analysis and Protein Adhesion Properties. *Colloids Surf. B Biointerfaces* **2013**, *110*, 248–253. https://doi.org/10.1016/j.colsurfb.2013.05.001.

(56) Přistoupil, T. I.; Kramlová, M.; Štěrbíková, J. On the Mechanism of Adsorption of Proteins to Nitrocellulose in Membrane Chromatography. *J. Chromatogr. A* **1969**, *42*, 367–375. https://doi.org/10.1016/S0021-9673(01)80636-1.

(57) Schachermeyer, S.; Ashby, J.; Zhong, W. Aptamer–Protein Binding Detected by Asymmetric Flow Field Flow Fractionation. *J. Chromatogr. A* **2013**, *1295*, 107–113. https://doi.org/10.1016/J.CHROMA.2013.04.063.

(58) Seok Kim, Y.; Ahmad Raston, N. H.; Bock Gu, M. Aptamer-Based Nanobiosensors. *Biosens. Bioelectron.* **2015**, *76*, 2–19. https://doi.org/10.1016/j.bios.2015.06.040.

(59) Tan, W.; Wang, H.; Chen, Y.; Zhang, X.; Zhu, H.; Yang, C.; Yang, R.; Liu, C. Molecular Aptamers for Drug Delivery. *Trends Biotechnol.* **2011**, *29* (12), 634–640. https://doi.org/10.1016/j.tibtech.2011.06.009.

(60) Tan, W.; Donovan, M. J.; Jiang, J. Aptamers from Cell-Based Selection for Bioanalytical Applications. *Chem. Rev.* **2013**, *113* (4), 2842–2862. https://doi.org/10.1021/cr300468w.

(61) Wang, L.; Lee, J. Y.; Gao, L.; Yin, J.; Duan, Y.; Jimenez, L. A.; Adkins, G. B.; Ren, W.; Li, L.; Fang, J.; Wang, Y.; Song, J.; Zhong, W. A DNA Aptamer for Binding and Inhibition of DNA Methyltransferase 1. *Nucleic Acids Res.* **2019**, *47* (22). https://doi.org/10.1093/nar/gkz1083.

(62) Orlando, C.; Pinzani, P.; Pazzagli, M. Developments in Quantitative PCR. **1998**, *36* (5), 255–269. https://doi.org/10.1515/CCLM.1998.045.

(63) Smith, C. J.; Osborn, A. M. Advantages and Limitations of Quantitative PCR (Q-PCR)-Based Approaches in Microbial Ecology. *FEMS Microbiol. Ecol.* **2009**, *67* (1), 6–20. https://doi.org/10.1111/j.1574-6941.2008.00629.x.

(64) PCR past, present and future https://www.ncbi.nlm.nih.gov/pmc/articles/PMC7439763/ (accessed 2021 -07 -31).

(65) Gu, L.; Yan, W.; Liu, L.; Wang, S.; Zhang, X.; Lyu, M. Research Progress on Rolling Circle Amplification (RCA)-Based Biomedical Sensing. *Pharmaceuticals* **2018**, *11* (2), 35. https://doi.org/10.3390/ph11020035.

(66) Liu, X.; Xue, Q.; Ding, Y.; Zhu, J.; Wang, L.; Jiang, W. A Cascade Signal Amplification Strategy for Sensitive and Label-Free DNA Detection Based on Exo III-Catalyzed Recycling Coupled with Rolling Circle Amplification. *Analyst* **2014**, *139* (11), 2884–2889. https://doi.org/10.1039/C4AN00389F.

(67) Yang, L.; Fung, C. W.; Cho, E. J.; Ellington, A. D. Real-Time Rolling Circle Amplification for Protein Detection. *Anal. Chem.* **2007**, *79* (9), 3320–3329. https://doi.org/10.1021/ac062186b.

(68) Nilsson, M.; Gullberg, M.; Dahl, F.; Szuhai, K.; Raap, A. K. Real-time Monitoring of Rolling-circle Amplification Using a Modified Molecular Beacon Design. *Nucleic Acids Res.* **2002**, *30* (14), e66–e66. https://doi.org/10.1093/nar/gnf065.

(69) Guo, K.; Li, Z.; Win, A.; Coreas, R.; Adkins, G. B.; Cui, X.; Yan, D.; Cao, M.; Wang, S. E.; Zhong, W. Calibration-Free Analysis of Surface Proteins on Single Extracellular Vesicles Enabled by DNA Nanostructure. *Biosens. Bioelectron.* **2021**, *192*, 113502. https://doi.org/10.1016/j.bios.2021.113502.

(70) Flack, K.; Jimenez, L. A.; Zhong, W. Analysis of the Distribution Profiles of Circulating MicroRNAs by Asymmetrical Flow Field Flow Fractionation. In *MicroRNA Profiling: Methods and Protocols*; Rani, S., Ed.; Methods in Molecular Biology; Springer: New York, NY, 2017; pp 161–168. https://doi.org/10.1007/978-1-4939-6524-3_15.

(71) Jimenez, L. A.; Zhong, W. Extraction of Small RNAsSmall RNAs by Titanium Dioxide NanofibersNanofibers. In *RNA Abundance Analysis : Methods and Protocols*; Jin, H., Kaloshian, I., Eds.; Methods in Molecular Biology; Springer US: New York, NY, 2021; pp 117–124. https://doi.org/10.1007/978-1-0716-0743-5_8.

(72) Trinh, M. P.; Carballo, J. G.; Adkins, G. B.; Guo, K.; Zhong, W. Physical and Chemical Template-Blocking Strategies in the Exponential Amplification Reaction of Circulating MicroRNAs. *Anal. Bioanal. Chem.* **2020**, *412* (11). https://doi.org/10.1007/s00216-020-02496-w.

Chapter 5: Conclusions and Future Outlook

5.1 - Dissertation Summary

The research presented here shows high versatility for NP analysis using AF4 to separate and fractionate with online NTA to determine the number and size distribution. Coupling the two together enhanced the capabilities by speeding up analysis time, decreasing sample input, and by identifying coeluted populations that may have been missed by bulk analysis with MALS or DLS. The coupling also enhanced NTA data as each population was enriched and the proper camera levels could be used for each population throughout the run.

AF4 was excellent for isolation and fractionation of BioNPs from complex matrices into enriched fractions due to the ability of AF4 to size fractionate under most aqueous conditions. The low concentration of proteins found in the fractions make downstream analysis difficult, but more advanced probing techniques as well as different probe types can be used to overcome the low SNR and increase assay repeatability. AF4 was able evaluate protein coronas through online NTA size data, retention time, and dispersity of the distribution. The gentle nature preserves the protein corona of ENPs and surface associated proteins of BioNPs making the system ideal for biological analysis of collected NPs.

5.2 - Future Advancements and Applications

5.2.1 - AF4-NTA Design

The AF4-NTA coupling is designed so that AF4-NTA operates under most run conditions AF4 may operate under for NP analysis. This provides ideal versatility for

deployment in a wide array of assays and studies, but the design has drawbacks, such as band broadening and time shifts to correlate the FC with the NTA data. The biggest advancement would be a fully redesigned NTA channel that can control a range of flow rates but maintains steady and consistent flow through the NTA. This would eliminate the splitter manifold set up and create a singular inline flow cell. The ideal unit would be a single NTA channel that maintains the flow rate for two lines with one having the viewing window and the other maintaining the sample plug going to the FC. The design would need to be somewhat complex as it would need to have a controlled needle valve with an attached flow sensor to monitor and adjust the flow rate as the AF4 pressure changes throughout the run. This type of design is used in Wyatt AF4 systems that utilize mass flow sensors combined with a needle valve to control the crossflow rate. The Wyatt system runs higher pressures because of this design choice but can control all focusing, cross flow and detector flows with a single liquid pump and lowers the cost of the instrument dramatically. The newer NTA channel would need to be resistant to the 30-bar limit of the Wyatt AF4 system if it is to be applicable for all AF4 systems.

5.2.2 - BioNP AF4-NTA Analysis

The AF4-NTA counting repeatability and consistent sizing performance makes it an excellent choice for BioNPs and downstream analysis. The system uses 15 µL of volume per fraction to collect NTA data, which is drastically less than the 1 mL offline NTA protocols require. The difficulty in performing downstream biochemical assays is the concentration of the collected fractions. The nitrocellulose membrane used in the dot-blot apparatus functioned as a concentration mechanism when the dilute BioNP proteins

are bound into a small area of the membrane. More efficient methods of concentrating the fractionated samples or increasing the binding affinity of the BioNPs to the nitrocellulose would help improve the SNR and further enhance the feasibility of BioNP analysis using a single injection, but multiple injections and the average of the distributions can be used to pool enough sample for robust analysis or increased sample volumes. The speed at which the sample can be labeled and analyzed is vastly superior to standard methodologies, especially when combining online NTA data with the protein analysis of the fractions. Additionally, a wide variety of amplification strategies and probe designs can be used in AF4-NTA and can be explored to find an optimal scheme for the post fractionation detection of BioNPs. With modified standard assays tuned to AF4-NTA limits, very rapid characterization and biochemical quantification can be realized.

The advancements outlined above would lead to AF4-NTA 2.0. The advantage of AF4-NTA is very promising and AF4-NTA 2.0 would be a system with very few drawbacks. It would have broad application for most NP research and be compatible with downstream biological detection using in-channel labeling. The label free NTA data is excellent at characterizing the fractions and the AF4 separation is excellent at enriching fractions for NTA and downstream analysis.

5.3 - Commercial Applications

AF4-NTA's best commercial application would be in the pharmaceutical industry analyzing nanomedicine and drug delivery vehicles.[1,2] FDA regulated products have stringent characterization requirements with specific knowledge about drug loading capacity, formulation stability, and drug leeching propensity. NTA's power is in individual

counting and sizing, and this can be exploited with online detection of the drug in tandem with the online NTA data. Quantification of the drug with UV-Vis or fluorescence divided by the particle counts directly gives you the drug loading capacity in a mass/particle unit. The pharmaceutical industry prefers label free methods as the probes can alter the aggregated state, size, reactivity, etc. NTA data is label free and produces true particle counts and is a compatible detector for nanosized drug products. In tandem with AF4, the free drug can be separated from the loaded NPs, providing information about the loading efficiency, loading capacity, and the aggregated state of the NPs in a single run with only two online detectors.

There is also potential in commercial NP manufacturing, especially commercial exosomes produced from cell cultures. The cultures done for exosome production at manufacturing scale are grown on the surface of hollow-fibers and fed fresh medium through a porous fiber.[3] Exosomes are secreted into the extracellular space around the fiber, which is collected as crude exosome secretions. The medium is then purified and characterized to judge confluency, yield, and cell maturity. Secretion rates, BioNP yield, and total protein concentration could be measured in a single run and continuously throughout the lifecycle of the cultures. BioNP production is very reliant on cell culture health and performance and is not always the same rate or yield.[4,5] Additionally, cultures need to grow before production rates are sufficient and this can be easily monitored by the secretion rates of the exosomes.

5.4 - References

(1) Klein, M.; Menta, M.; Dacoba, T. G.; Crecente-Campo, J.; Alonso, M. J.; Dupin, D.; Loinaz, I.; Grassl, B.; Séby, F. Advanced Nanomedicine Characterization by DLS and AF4-UV-MALS: Application to a HIV Nanovaccine. *J. Pharm. Biomed. Anal.* **2020**, *179*, 113017. https://doi.org/10.1016/j.jpba.2019.113017.

(2) Ansar, S. M.; Mudalige, T. Characterization of Doxorubicin Liposomal Formulations for Size-Based Distribution of Drug and Excipients Using Asymmetric-Flow Field-Flow Fractionation (AF4) and Liquid Chromatography-Mass Spectrometry (LC-MS). *Int. J. Pharm.* **2020**, *574*, 118906. https://doi.org/10.1016/j.ijpharm.2019.118906.

(3) Storm et al. - 2016 - Hollow Fiber Bioreactors for In Vivo-like Mammalia.Pdf.

(4) Chiu, Y.-J.; Cai, W.; Shih, Y.-R. V.; Lian, I.; Lo, Y.-H. A Single-Cell Assay for Time Lapse Studies of Exosome Secretion and Cell Behaviors. *Small* **2016**, *12* (27), 3658–3666. https://doi.org/10.1002/smll.201600725.

(5) Exosomes Development & Manufacturing | For Therapy | Lonza https://pharma.lonza.com/technologies-products/exosomes (accessed 2021 -08 -02).